# PENGUIN

## TURBINE TRAINER HELICOPTER

Alfred Gessow Rotorcraft Center
Department of Aerospace Engineering
University of Maryland, College Park

Graduate Level Design Category

University of Maryland

Alfred Gessow Rotorcraft Center

Department of Aerospace Engineering

University of Maryland

College Park, Maryland 20742

# PENGUIN

## TURBINE TRAINER HELICOPTER

In response to the 2006 American Helicopter Society

Student Design Competition - Graduate Category

June 2, 2006

Peter Copp - Team Leader, Graduate Student

Dr. Inderjit Chopra - Faculty Advisor

Arun Jose, Graduate Student

Moble Benedict, Graduate Student

Shyam Menon, Graduate Student

Vishnu Keshavan, Graduate Student

Brandon Fitchett, Graduate Student

Bryant Craig, Graduate Student

Nitin Kumar Gupta, Graduate Student

# Acknowledgements

The Penguin design team would like to acknowledge the following people and thank them for their advice and assistance:

Dr. Vengalattore T. Nagaraj — Research Scientist, Dept. of Aerospace Engineering, University of Maryland, College Park. Co-advisor for the design course, for his valuable guidance throughout the design process.

Dr. Marat Tishchenko — Former Chief Designer, Mil Design Bureau, for his numerous comments and useful suggestions.

Dr. Inderjit Chopra - Professor, Department of Aerospace Engineering, University of Maryland, College Park.

Mr. David J.H. Eames, Chief, Product and Technology Strategy, Allison Advanced Development Company.

Dr.Christopher Cadou - Assistant Professor, Department of Aerospace Engineering, University of Maryland, College Park.

Dr. Roberto Celi - Professor, Department of Aerospace Engineering, University of Maryland, College Park.

Dr. Jinsong Bao, Dr. Paul Samuel, Dr. Anubhav Datta - Research Scientists, Department of Aerospace Engineering, University of Maryland, College Park.

Carlos Malpica, A. Abhishek, Nicholas Rosenfeld - Graduate Students, Department of Aerospace Engineering, University of Maryland, College Park.

Special thanks to Shreyas Ananthan and Sudarshan Kaushik - Graduate Students, Department of Aerospace Engineering, University of Maryland, College Park, for their help with formatting this report in LaTeX

# Contents

# List of Figures

# List of Tables

# List of Symbols and Abbreviations

| Symbol | Description | Symbol | Description |
|---|---|---|---|
| AHS | American Helicopter Society | $\mu$ | Advance Ratio |
| CG | Center of Gravity | $\sigma$ | Solidity |
| CR | Compression Ratio | $C_T$ | Thrust Coefficient |
| FCS | Flight Control System | c.g. | Center of Gravity |
| FBW | Fly-By-Wire | $\theta$ | Blade Pitch |
| HOGE | Hover Out of Ground Effect | FADEC | Full Authority Digital Electronic Control |
| HUMS | Health and Usage Monitoring System | R/c | Blade Aspect Ratio |
| ISA | International Standard Atmosphere | GPS | Global Positioning System |
| MSL | Mean Sea Level | AoA | Angle of Attack |
| NOTAR | No Tail Rotor | Nb | Number of Blades |
| NTSB | National Transportation Safety Board | ROC | Rate of Climb |
| RFP | Request for Proposals | $\Omega$ | Angular Velocity |
| SHP | Shaft Horsepower | DL | Disk Loading |
| SFC | Specific Fuel Consumption | DOC | Direct Operating Cost |
| TIT | Turbine Inlet Temperature | IOC | Indirect Operating Cost |
| UMARC | University of Maryland Advanced Rotor Code | ADF | Automatic Direction Finder |
| VHQ | Variable Handling Qualities | DME | Distance Measuring Equipment |
| VFR | Visual Flight Rules | VOR | VHF Omnidirectional Range |
| IFR | Instrument Flight Rules | HSI | Horizontal Situation Indicator |
| FAR | Federal Aviation Regulation | MFD | Multi-Functional Display |
| MTBF | Mean Time Before Failure | MTTR | Mean Time to Repair |
| TO | Take Off | MCP | Maximum Continuous Power |
| APU | Auxiliary Power Unit | RPM | Rotations Per Minute |
| AGMA | American Gear Manufacturers Association | | |

## RFP Requirements and Compliance

| RFP Requirement | Action Taken | Reference |
|---|---|---|
| Inexpensive to acquire | Acquisition cost primary concern in almost all design decisions, $266k purchase price; Competitive with current trainers. | Ch. 12, Pg. 73; Throughout proposal |
| Include conceptual design for low cost turbine engine | 145 hp Pyros compact oil free turbine engine with low SFC and high power to weight ratio | Ch. 6, Pg. 29 |
| Airframe and engine maintain normal standards of safety and reliability | Design follows FAR 27; Transmission HUMS included. Engine has FADEC. Sufficient attention paid to safety and acquisition cost. | Throughout proposal |
| Focus on innovative manuafacturing cost reduction concepts | Lean Manufacturing, Powder metallurgy for turbine blades | Throughout proposal, Sec. 6.5.5, Pg. 47 |
| Rugged | Landing Gear; airframe | Ch. 9, Pg. 60 |
| Durable | 4000 hrs transmission; composite tailored low vibration rotor; foil bearings in engine | Ch. 3, Pg. 16, Ch. 7, Pg. 53 |
| Good Autorotative Capability | Use of tip weight to increase Autorotative Index | Ch. 3, Pg.16 |
| Capable of lifting two 90 kg people, 20 kg miscellaneous equipment and enough fuel to hover out of ground effect for 2 hr. at 6000 ft. on an ISA $+20^{\circ}$C day | Conservative power and fuel requirement estimate ensures full compliance with this requirement | Ch. 2, Pg. 11 |
| Forward speed performance superior to current piston trainers | Compares favorably with Robinson R22 and Schweizer 300CBi | Ch. 11, Pg. 68 |
| *ab initio* and advanced training in same aircraft | Innovative design for Variable Handling Qualities (VHQ); Optional IFR display or glass cockpit | Ch. 5, Pg. 24, Sec. 10.1, Pg. 63 |

# Executive Summary

*"To all the Penguins who always knew*
*they were meant for more than this world:*
*Light the Pyros within and soar to the*
*heights far above the hills of doubt"*

The Penguin is a 2 seat single turbine engine trainer helicopter designed in response to the 2006 American Helicopter Society's Request for Proposal (RFP), sponsored by Bell Helicopter. There is a gulf between the operating characteristics of current light piston training helicopters and the commercial fleet of turbine helicopters. Training schools purchase less expensive piston helicopters to lower the life cycle costs and make it more affordable for customers. Turbine helicopters in this class are more expensive than piston helicopters due to the cost of the engine. For a turbine trainer to be successful, the design must focus on a low acquisition cost. No existing turbine engine meets the requirements of the RFP at a low cost while operating efficiently. The first-of-its-kind oil-free Pyros turbine engine more than adequately meets this need. Even with the advanced Pyros turbine engine, the Penguin's purchase price ($266k) compares favorably with current piston trainers. The low purchase cost derives in part from innovative manufacturing cost reduction concepts. Other innovations include Variable Handling Qualities (VHQ), designed specifically to make the Penguin a more versatile training platform than any of its competitors. The Penguin also offers superior performance in comparison to its competitors both in forward flight speed, hover altitude, endurance and range.

## Design Requirements

The RFP requires a 2-place turbine engine training helicopter that is competitive with current training piston helicopters. Acquisition cost was the key factor and operating efficiency was a secondary concern. The conceptual design of a low cost turboshaft engine was included. The helicopter was required to have the ruggedness, durability and autorotative performance that the training environment entails. The helicopter should be capable of lifting two 90 kg people, 20 kg of miscellaneous equipment and enough fuel to hover out of ground effect for two hours at 6000 ft. on an ISA $+20^{\circ}$C day. The RFP also suggested forward flight performance superior to current piston trainers.

## Configuration Selection

A training helicopter must have a similar configuration as the majority of today's helicopters. A tandem, coaxial, synchropter or compound configuration would therefore not work well as a trainer. A single main rotor with a

conventional tail rotor was chosen. Fan-in-fin or NOTAR systems do not offer enough benefit for the large cost increase. A review of Robinson R22 (which has a conventional tail rotor) accidents reveals no in-flight accidents due to tail rotor strikes. Available accident data does not suggest that people approach the R22 from the rear and accidentally walk into the tail rotor.

## Design Methodology

The Penguin was designed to fulfill ENAE634 Helicopter Design, a one semester Spring 2006 course. No commercial engineering computer programs were used except GASTURB for the engine cycle analysis. Preliminary sizing and analysis were based on Tishchenko's methodology. The drawings were made using CATIA and Pro-Engineer. Rotor dynamics analysis was performed using the University of Maryland Advanced Rotor Code (UMARC).

## Design Features

The following features make the Penguin stand out as a training helicopter:

**Low Acquisition Cost** — Preliminary cost analysis estimates a $266k purchase price. This cost compares favorably with the cost of the piston powered Robinson R22 ($215k) and Schweizer 300CBi ($295k) helicopters. Cost-saving manufacturing methods used by both the Penguin helicopter and the Pyros engine reduce the overall acquisition cost.

**Pyros Oil-Free Engine** — This low-cost oil-free engine, designed specifically for the Penguin, reduces the expected price differential between a piston engine helicopter and a turbine engine helicopter. The gas generator section consists of a back to back radial compressor and turbine on the same shaft running at 100,000 RPM. Power is extracted by a free turbine on a separate shaft running at 75,000 RPM. The high RPM allowed for a compact engine. The turbine blades are made out of a low cost Ni-based superalloy. A high compression ratio and high turbine inlet temperature (without blade cooling) gives the Pyros a low SFC and high power to weight ratio. The SFC is 50% lower and the power to weight ratio 25% higher than APU derived turboshaft engines with comparable power output. The engine uses foil bearings to handle the high shaft speeds. These also eliminate lubrication requirements, significantly reducing the engine's maintenance costs as well as eliminating the cost and weight of the oil system. The engine was designed for ease of accessibility, assembly and disassembly to facilitate inexpensive maintenance. The gas generator can be be separated from the power turbine section by disassembling at just one location. A FADEC improves performance and safety.

**VHQ (Variable Handling Qualities)** — Using a simple and innovative mechanical system to alter the pilot inputs to the swashplate, the pilot can safely and easily change the handling qualities of the helicopter. This is accomplished without using a complex and expensive fly-by-wire system. The pilot can learn to fly several categories of helicopters on the same platform. This greatly enhances the Penguin's value as a trainer by providing both *ab initio* and advanced training.

**Cockpit Options** — Optional IFR instrumentation allows the trainee to become familiarized with this equipment before flying an IFR certified helicopter. An optional glass cockpit follows the industry trend towards standard glass cockpits. A trainee's performance can be reviewed from recorded flight data.

**Good Autorotative Characteristics** — Blade tip weights significantly increase rotor inertia thereby providing good autorotational characteristics.

**Simple, 4000 Hour Total Reduction Transmission** — All reduction from the free turbine shaft at 75,000 RPM to the main rotor shaft at 550 RPM is achieved through this compact and lightweight transmission. The optimized design is simple and well proven. A low part number count and modular design reduces manufacturing costs. The 4000 hour MTBF reduces life cycle costs.

**Low Vibration** — By choosing three blades over two blades (at little to no acquisition cost penalty), the Penguin has low vibration levels. Composite blades reduce the vibration levels through tailored elastic coupling.

**Hingeless Rotor Hub** — Maintenance and part count are reduced compared to an articulated rotor. The hingeless design provides an effective hinge offset so that unlike the R22, mast bumping is not an issue and control authority is increased. The elastomeric lag damper inside the hub plates results in a more compact hub.

**Superior Safety and Crashworthiness** — An alarm system will warn the pilot that he is in the dead man's curve or is approaching the tail rotor authority limit. An inexpensive crash seat (adds $250/seat) using crushable aluminum foam adds to the crashworthiness. The airframe, landing gear, fuselage and floor were designed to absorb the energy of a crash.

**Superior Performance** — In comparison to the Robinson R22, the Penguin has 22% more range, 75% greater endurance, twice the rate of climb, twice the HOGE ceiling and 14 knots extra maximum cruise speed.

**Health and Usage Monitoring System (HUMS)** — The transmission and engine are monitored via basic HUMS, thereby lowering maintenance costs.

**Roomy Cabin** — The cabin has a width of 60 inches giving more room for occupants than its competitors. Ergonomic designs maintain comfort for even the longest duration flights.

**Manufacturing Cost Reductions** — Lean manufacturing methods employed throughout the Penguin and Pyros design significantly reduce manufacturing costs. The cockpit design employs simple curvatures. Powder production and processing have been employed in turbine blade manufacturing.

## Conclusion

The Penguin is a two place turbine-engine training platform that offers the best value for the lowest cost. The Penguin offers its users a safe, crashworthy vehicle with a cockpit and VHQ system specifically designed for training. The Penguin has superior performance characteristics as compared to its competitors. The Pyros turboshaft engine meets the challenge set out by the RFP's low-cost engine requirement with a state-of-the-art oil-free system. The Pyros has a low SFC and high power to weight ratio. A long life transmission and basic HUMS system reduces maintenance costs. These advantages along with manufacturing innovations spread throughout the proposal make the Penguin the ideal 2-place turboshaft training helicopter.

# Performance Summary and Physical Data

| VEHICLE DIMENSIONS | | MAIN ROTOR SPECIFICATIONS | |
|---|---|---|---|
| Overall Length | 28.5 ft (8.69 m) | Diameter | 23.3 ft(7.12 m) |
| Height - Hub | 7.9 ft (2.41 m) | Number of Blades | 3 |
| Fuselage Width | 5 ft (1.52 m) | Chord (root) | 0.49 ft (0.15 m) |
| Horizontal Stabilizer | 2.2 ft (0.67 m) | Chord (tip) | 0.49 ft (0.15 m) |
| Fuel Capacity | 23.8 gal (90 l) | Solidity | 0.04 |
| **WEIGHTS** | | Disk Loading | 3.14 lb/$ft^2$ (15.35 kg/m$^2$) |
| Design Gross Weight | 1345 lb (610 kg) | Blade Twist | $-11^\circ$ linear |
| Empty Weight | 743 lb (337 kg) | Tip Speed | 672 ft/s (205 m/s) |
| Useful Load | 602 lb (273 kg) | Shaft RPM | 550 |
| Max. Usable Fuel | 161 lb (73 kg) | Shaft Tilt | $3^\circ$ forward |
| Pilot + Pass. + Equip. | 441 lb (200 kg) | Tip Anhedral | $10^\circ$ |
| ***PYROS* ENGINE RATINGS** | | Root Cutout | 13% |
| TO Power (5 min) | 180 hp (134 kW) | Airfoil Section | SC-1095 |
| Max. Cont. Power | 165 hp (123 kW) | **TAIL ROTOR SPECIFICATIONS** | |
| Specific Fuel Consumption | 0.61 lb/hp/hr (0.37 kg/kW/hr) | Diameter | 3.59 ft (1.09 m) |
| | | Number of Blades | 2 |
| **PERFORMANCE** | | Chord | 0.27 ft (0.082 m) |
| Design Cruise Speed | 103 kts (190 km/hr) | Solidity | 0.095 |
| Speed for Best Range | 78 kts (144 km/hr) | Blade Twist | $-8^\circ$ linear |
| Speed for Best Endurance | 48 kts (89 km/hr) | Tip Speed | 672 ft/s (205 m/s) |
| Maximum Cruise Speed | 110 kts (204 km/hr) | Shaft RPM | 3592 |
| Maximum Range | 243 nm (450 km) | Airfoil Sections | NACA0012 |
| Maximum Endurance | 3.85 hrs | **TRANSMISSION** | |
| Vertical ROC | 900 ft/min (274 m/s) | TO Rating | 150 hp (112 kW) |
| Maximum ROC | 1894 ft/min (577 m/s) | Max. Cont. Rating | 145 hp (108 kW) |

# Foldout 1: Four-View Drawing of the Penguin

UNIVERSITY OF MARYLAND

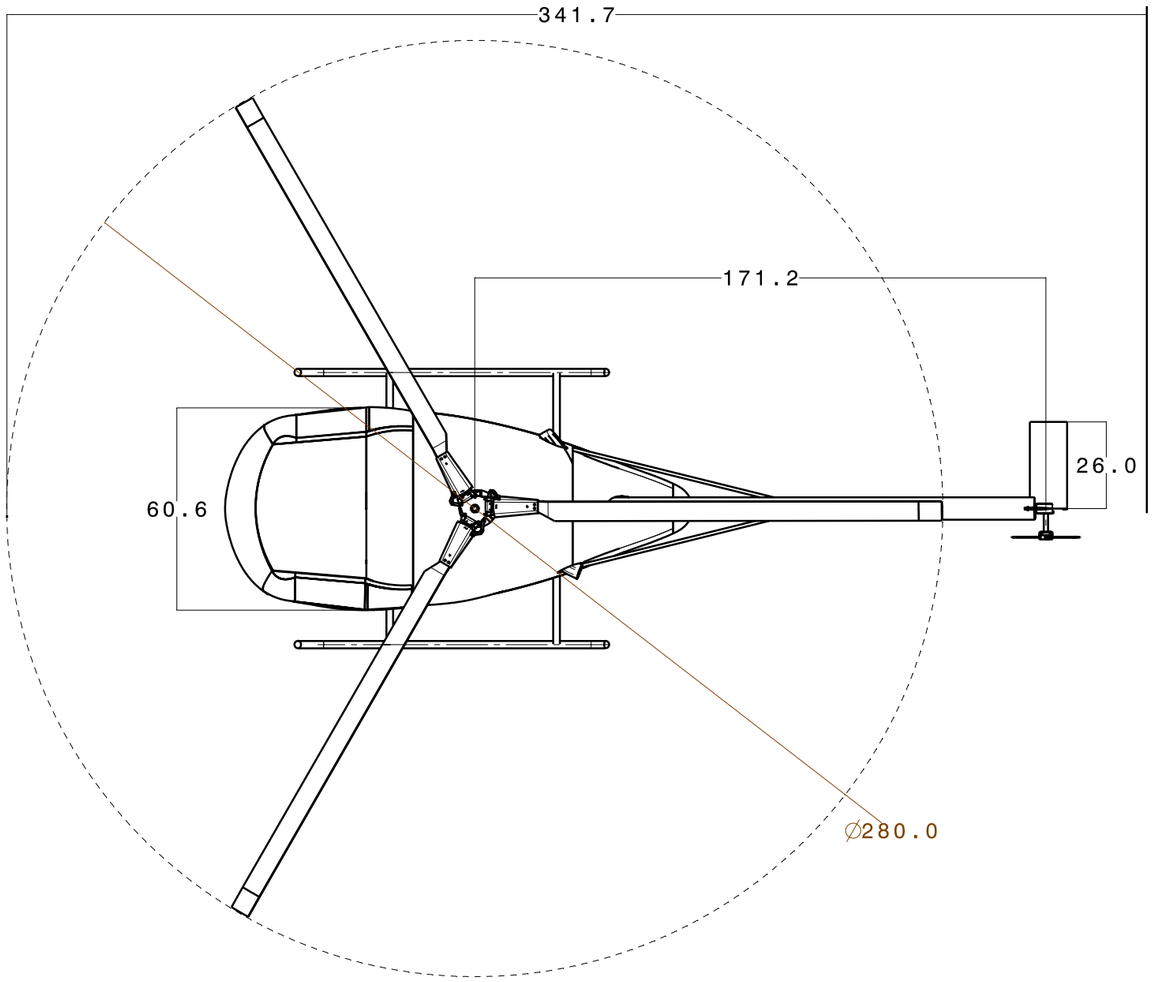


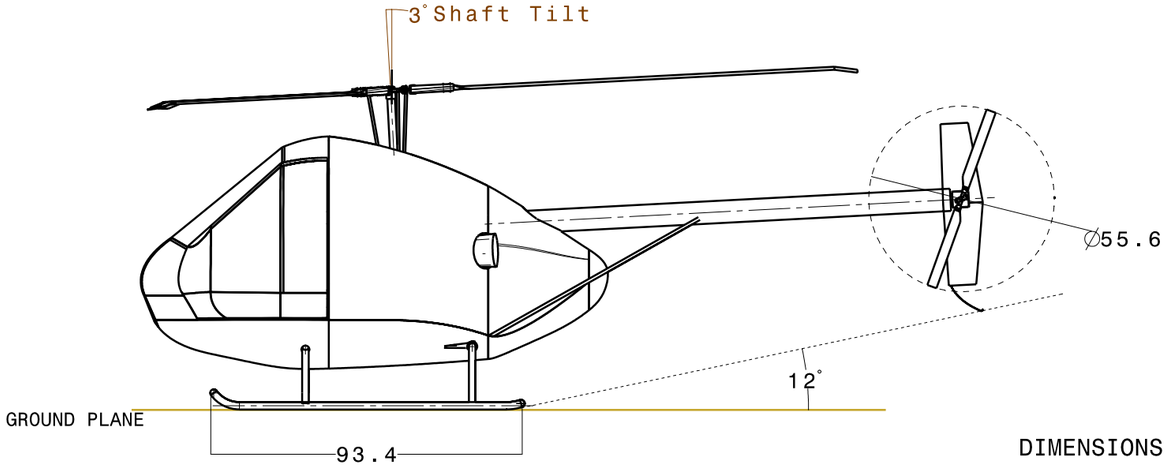


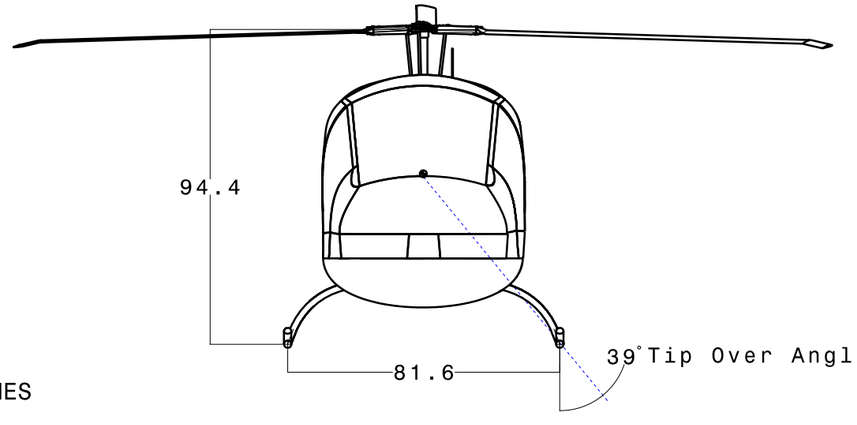


DIMENSIONS IN INCHES

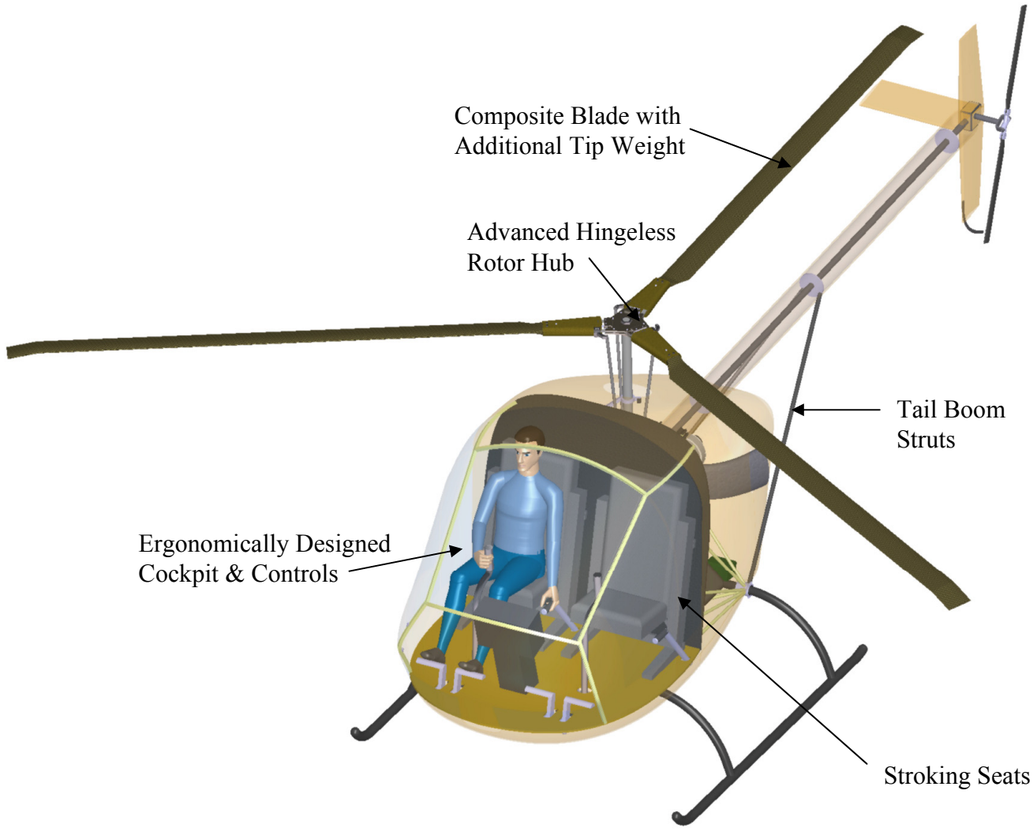


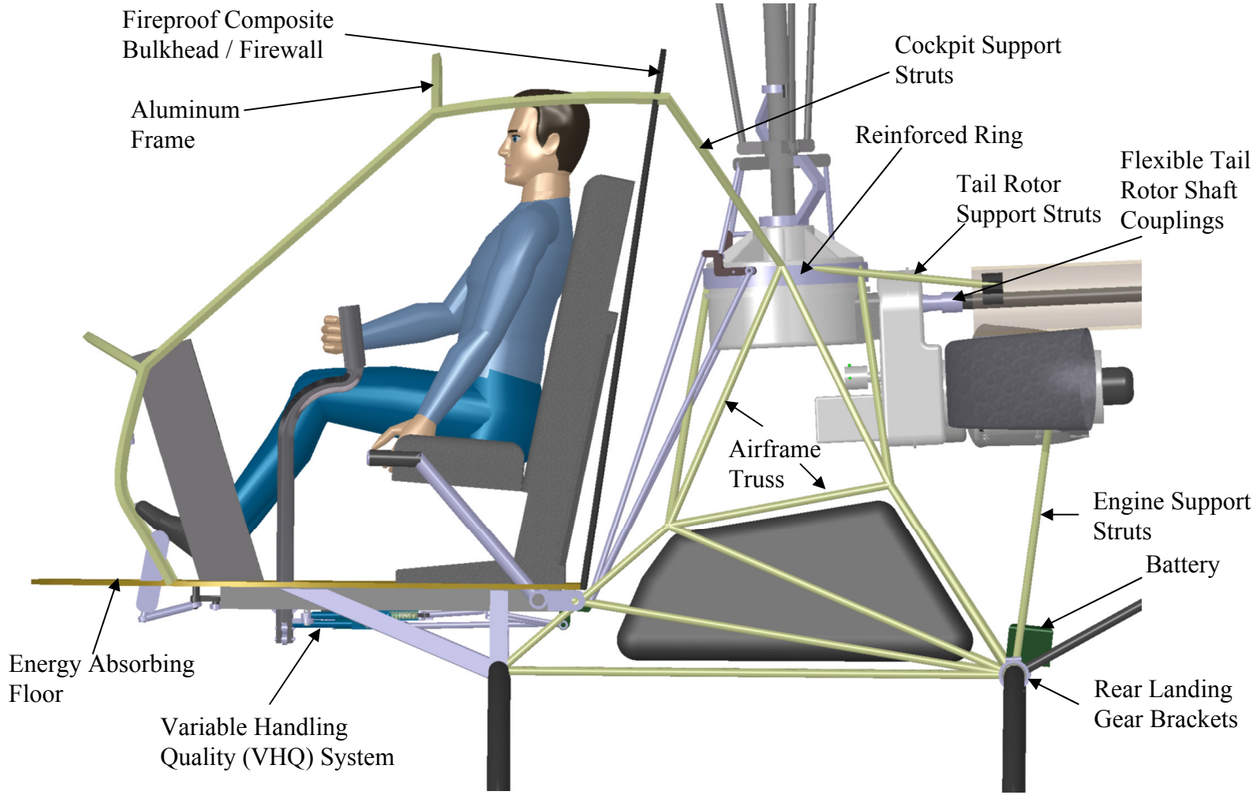


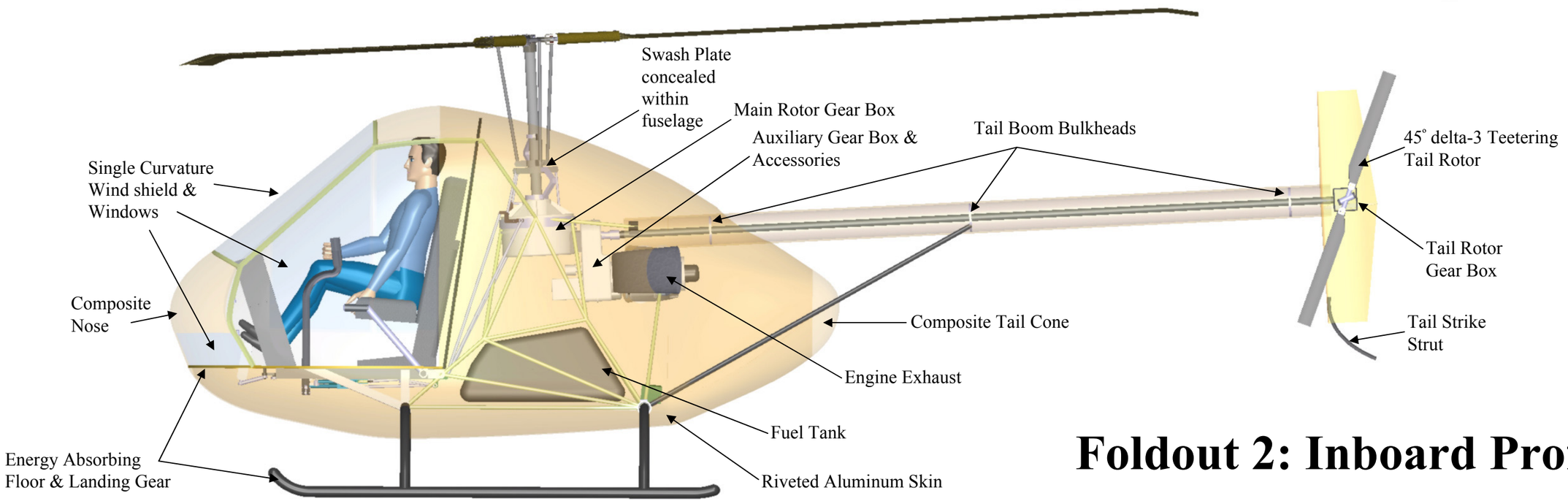


# Foldout 2: Inboard Profile

# PYROS

**Advanced Engine Technology**

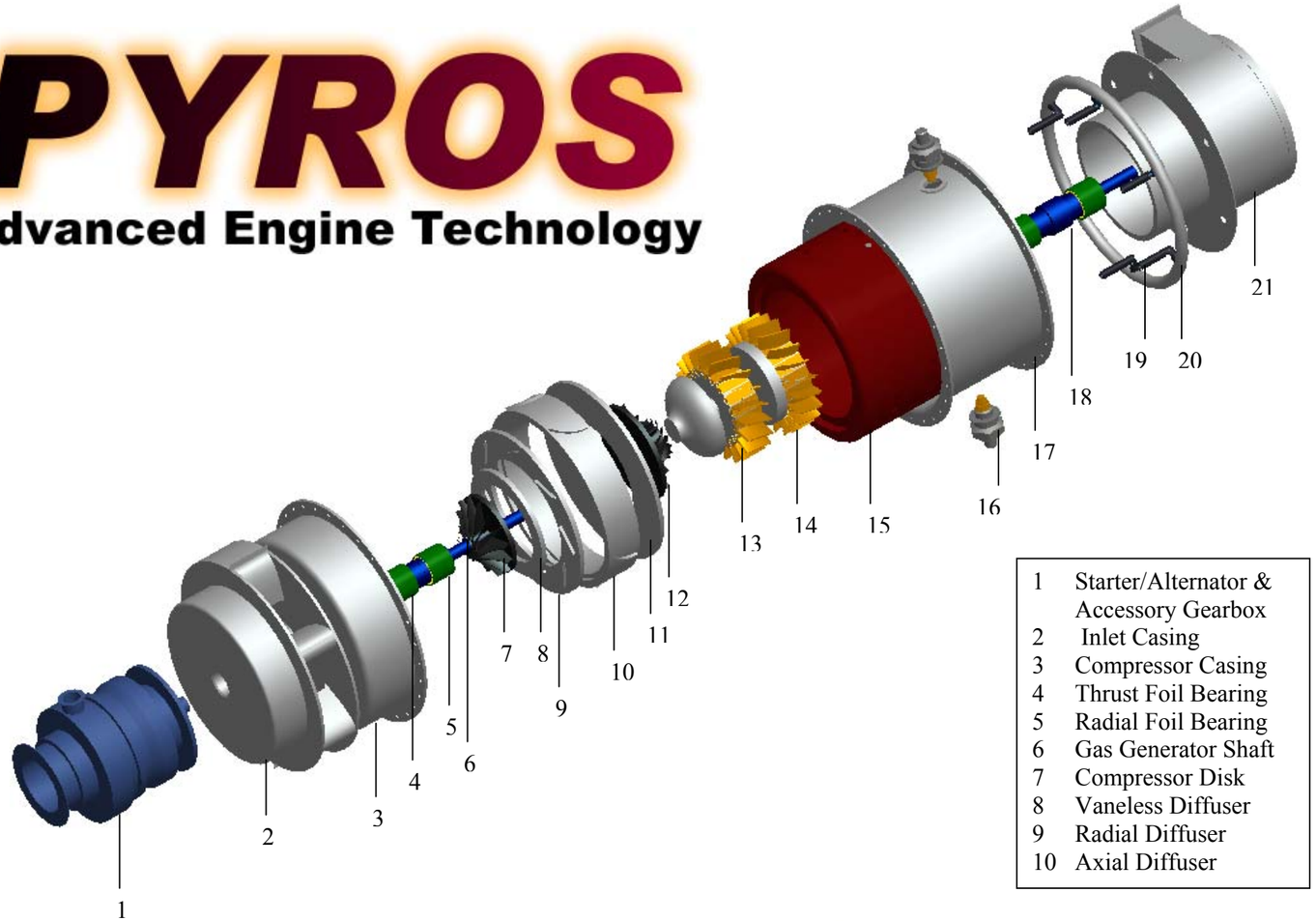


| | | | |
|---|---|---|---|
| 1 | Starter/Alternator & Accessory Gearbox | 11 | Nozzle Guide Vanes |
| 2 | Inlet Casing | 12 | HP Turbine Disk |
| 3 | Compressor Casing | 13 | Stator Disk |
| 4 | Thrust Foil Bearing | 14 | Axial LP Turbine |
| 5 | Radial Foil Bearing | 15 | Combustor Liner |
| 6 | Gas Generator Shaft | 16 | Igniter |
| 7 | Compressor Disk | 17 | Combustor Casing |
| 8 | Vaneless Diffuser | 18 | Power Turbine Shaft |
| 9 | Radial Diffuser | 19 | Fuel Injector |
| 10 | Axial Diffuser | 20 | Fuel Pipe |
| | | 21 | Exhaust Duct |

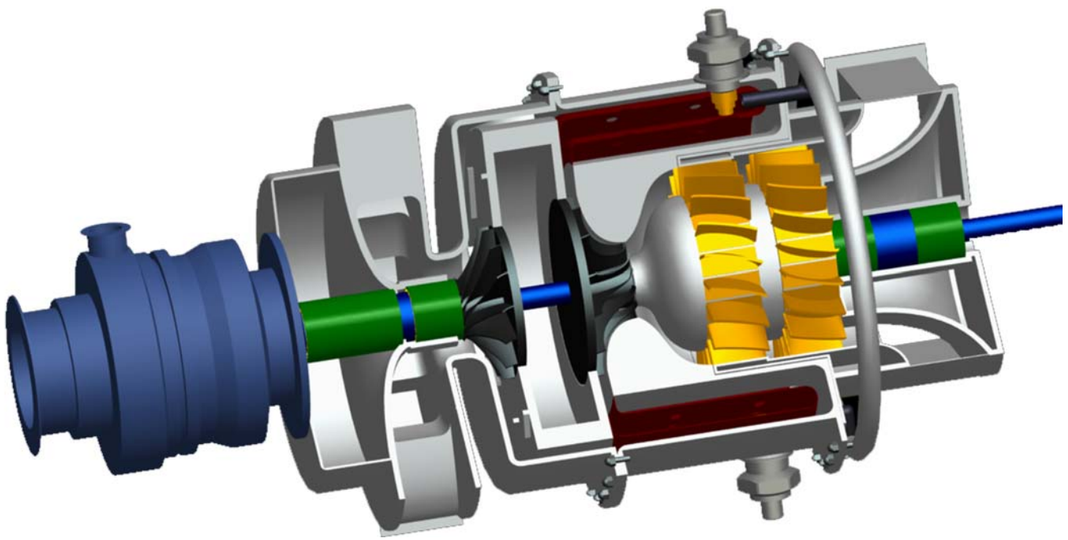

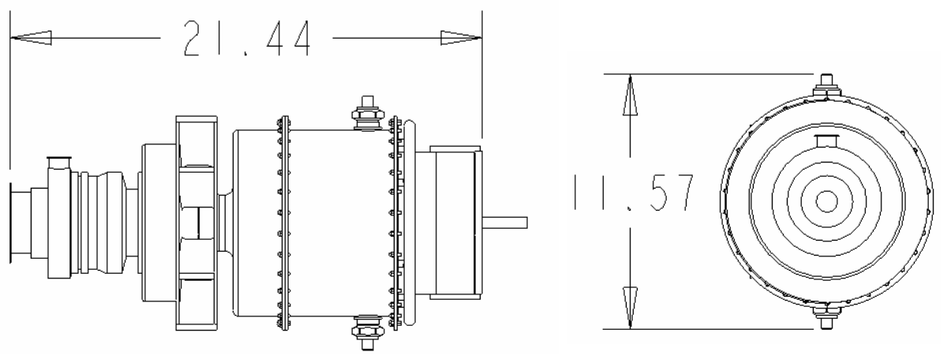


## Foldout 3: Engine Drawing

# 1 Introduction

This proposal describes the design of the Penguin, a 2-seat turbine-engine training helicopter and its low-cost turboshaft powerplant, the Pyros. The proposal was developed in response to the RFP of the 2006 AHS Student Design Competition. There exists an operational gulf between piston training helicopters and the commercial fleet of turbine helicopters. A turbine helicopter may have different handling qualities than a piston engine helicopter. The turbine engine may lag in throttle response compared to a piston engine. The engine gauges will be different. The pilot needs to be aware of these differences. Because of these differences, potential pilots are forced to undergo expensive transition training in a turbine helicopter after completing piston training.

Training schools purchase piston helicopters because of their low acquisition cost and low operating cost. Any new turbine trainer must therefore be inexpensive to acquire. This will be difficult because for this size helicopter, a turbine engine costs more than a piston engine. Therefore, the Pyros turboshaft engine was designed and optimized for this class of helicopter.

Another way to bring down costs is through lowering the performance metrics. This was not the choice made with the Penguin. Instead, the Penguin has been designed to exceed the standard set by the market controlling Robinson R22. Inexpensive innovative design features such as variable handling qualities and a basic HUMS have been included. Various innovations that reduce the manufacturing costs of each component are discussed throughout the proposal.

## 1.1 Design Drivers

- Acquisition cost
- The RFP requires hover out of ground effect for 2 hours at 6000 ft. with a payload of two 90 kg people and 20 kg of miscellaneous equipment on an ISA $+20^{\circ}$C.
- Forward flight performance: The RFP requires that the Penguin should have forward flight performance superior to that of current piston trainers. This is more important than hovering performance for a training helicopter. In our discussion with training school pilots, we found out that they spend most of their flying time in forward flight and not in hover. Often for training, the helicopter must fly to a special location away from the airport. Thus, a faster helicopter will spend less training time getting to that location and more time actually training at that location. The forward flight requirement influenced the blade twist. Table 1.1 shows how the Penguin forward flight speed and other parameters including its HOGE limit compare favorably with its competitors. The Penguin holds up very well in HOGE and economic cruise speed despite having less horsepower than all other helicopters except the R22.
- Autorotation - Over 40% of R22 accidents occurred after an autorotation [1]. The RFP requires good autoro-

| Model | Installed SHP | Max T/O Weight (lb) | Payload (lb) | HOGE (ft) (ISA+0°) | Cruise Speed (kts) |
|---|---|---|---|---|---|
| **Bell 206B3 JetRanger** | 420 | 32000 | 1522 | 8800 | 114 |
| **Enstrom 480** | 269 | 2850 | 1175 | 12200 | 96 |
| **Enstrom F280FX** | 225 | 2600 | 1015 | 8700 | 93 |
| **Robinson R22 Beta II** | 131 | 1370 | 525 | 5200 | 83 |
| **Rotorway EXEC 162F** | 150 | 1500 | 525 | 5000 | 83 |
| **Schweizer 300CBi** | 180 | 1750 | 662 | 4800 | 80 |
| **Schweizer 330SP** | 420 | 2260 | 1120 | 11200 | 102 |
| **Penguin** | 145 | 1345 | 440 | 10000 | 103 |

**Table 1.1:** Comparison of Potential Training Helicopters

tative capability. This led to the Penguin's high inertia rotor.

- As required in the RFP, the helicopter must accommodate both *ab initio* and advanced training.
- Ruggedness and Durability - A training helicopter should be designed for the training environment.

## 1.2 Configuration Selection

A training helicopter must be similar to the helicopters the trainee is likely to fly after the completion of his training. The fleet of commercial helicopters consists of many rotor configurations, but single main rotors are most common among them. A trainer helicopter with an alternate rotor configuration such as tandem or coaxial will not teach the pilot how to use a conventional anti-torque system. Thus the configuration of choice is a single main rotor/tail rotor system. This could be with a conventional tail rotor, NOTAR or fenestron. The conventional tail rotor has been chosen. The NOTAR tail rotor system was excluded because it is prohibitively expensive. A fenestron is more expensive than a conventional tail rotor but it is perceived to be safer. A survey of all R22 accidents reported to the NTSB showed that tail rotor strikes did not cause any accidents [1]. So, a conventional tail rotor was chosen over a fenestron.

## 1.3 Engine Design Philosophy

The RFP assumes that no current turbine engine meets the low acquisition cost requirement. So, a conceptual design for a low cost turbine engine must be included. The Pyros turbine engine meets this requirement. The Penguin requires 125 hp at 6000 ft ISA +20°C. Through cycle analysis it was found that the best SFC occurs when the engine operates at its design horsepower with the components operating at their limits. So, the engine was designed to produce at most 125hp at 6000 ft ISA +20°C. A higher horsepower is not required as engine cost increases with increasing horsepower. The RFP production rate of 300 aircraft per year assures a large enough market so that the Pyros does not need to be built for a larger horsepower in order to potentially increase its

market size and drive down its cost with economies of scale. Foil bearings offer considerable cost savings by eliminating the need for a lubrication system.

# 2 Preliminary Sizing and Weight Estimate

## 2.1 Design Requirements

The RFP states that the helicopter should be "capable of lifting two 90 kg people, 20 kg of miscellaneous equipment and enough fuel to hover out of ground effect (HOGE) for 2 hr, into a HOGE at 6000 ft on an ISA $+20^{\circ}$ C day". This, along with the decision to go for a single main rotor with conventional tail rotor configuration, is taken as the primary input for preliminary sizing and weight analysis.

## 2.2 Methodology

For preliminary design analysis, the methodology developed by Tischenko [2] at Mil Design Bureau and later modified at the University of Maryland is used. An in-house code has been developed based on the Tischenko model and tailored for light weight helicopters. The inputs to the analysis include RFP specifications (payload, HOGE requirements), assumed parameters ($C_T/\sigma$, tip speed, flat plate area, SFC, etc.) and empirical data (loss factors, component weight coefficients, etc.). The assumed parameters are refined at successive stages of the design process as the different subsystems (engine, transmission, etc.) evolve.

The Tischenko method first calculates the size and power requirements of the main rotor based on an initial gross weight estimate. From the main rotor size and power, the tail rotor and gearbox size, torque and power requirements are computed. Appropriate loss parameters are used to account for aerodynamic, transmission, engine installation and other losses. Once the size and power requirements are known, the weights of different components (main rotor, fuselage, engine, drive system, etc.) are estimated based on empirical formulas obtained from historical data and tailored for the design problem. The fuel weight is then computed by imposing the HOGE performance requirement specified in the RFP. The updated gross weight estimate is then used to repeat the sizing calculations and the process is continued until convergence, following which, the performance characteristics and cost are estimated. The analysis is performed concurrently for different number of blades and aspect ratios and the final configurations obtained are evaluated based on different metrics (e.g., gross weight, acquisition cost, cruise speed, etc.).

Figure 2.1 shows the weight efficiency (i.e., $1 - M_{\text{empty}}/M_{GW}$) versus disk loading for different number of blades and aspect ratios. The weight efficiency decreases with increasing blade number and increases with increasing aspect ratio. The power required for hover (and hence also the fuel weight) increases with increasing

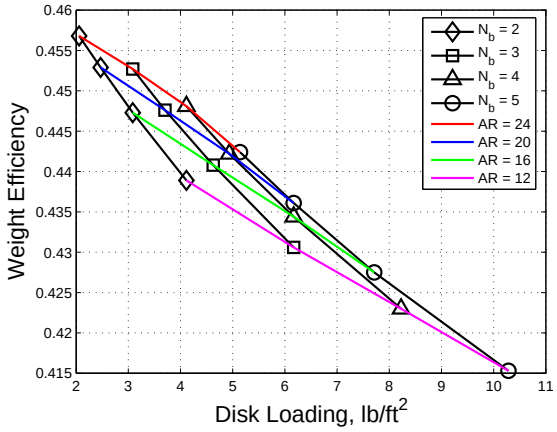


**Figure 2.1:** Weight Efficiency vs. Disk Loading

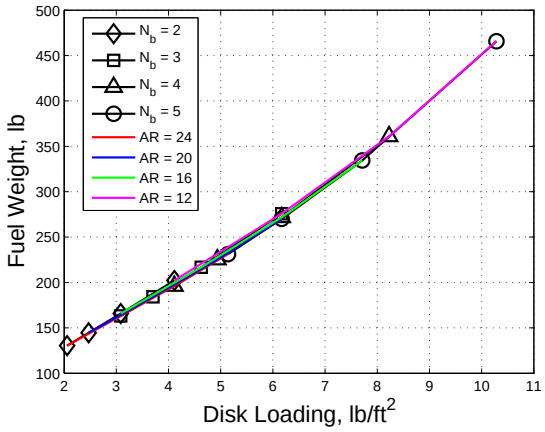


**Figure 2.2:** Fuel Weight vs. Disk loading

disk loading. In general, increasing the number of blades results in higher disk loading while increasing the aspect ratio lowers the disk loading. Figure 2.2 shows that the fuel weight required for hover increases with increasing disk loading (i.e., increases with increasing blade number and decreases with increasing aspect ratio). However it should be noted that more installed power allows the helicopter to attain higher flight speeds and climb rates. The analysis also showed that empty weight and acquisition cost increase with increasing disk loading .

Another important parameter determining the operating efficiency of the helicopter is the Direct Operating Cost (*DOC*) per passenger per kilometer. The *DOC* is estimated using Tischenko's formula, which is given by:

$$\text{DOC}_{fh} = \frac{3P}{\text{Total Flight Hours}} + P_{\text{fuel}} \times Q + N_{\text{crew}} \times S_{\text{crew}}$$

where $P$ is the acquisition price, $P_{\text{fuel}}$ is the fuel price per gallon, $Q$ is the fuel consumption in gallons per flight hour, $N_{\text{crew}}$ is the number of crew members and $S_{\text{crew}}$ is the crew salary per flight hour. The Penguin is assumed to have a life of 10,000 hrs. Figure 2.3 shows the trends in *DOC* per passenger per kilometer. It is observed that increasing the aspect ratio reduces the *DOC* per passenger km, while no monotonic behavior is observed with change in the number of blades. While an increased disk loading increases the acquisition cost ($P$) and fuel consumption, it also increases the maximum speed (and hence also the range) because of the higher installed power. Studies were also performed for other quality metrics such as gross weight, cruise speed, etc. Because all quality metrics do not show the same trend on varying aspect ratio and number of blades, a Multi-component quality index is defined in which weight factors are assigned to different quality metrics. The best choice of blade

number and aspect ratio is therefore arrived at by using the *Multi-Component Index (MCI)* which is defined as:

$$\text{MCI} = \sum_{i=1}^{m} \chi_i \frac{Q_i - Q_{min_i}}{Q_{max_i} - Q_{min_i}} + \sum_{i=m+1}^{N} \chi_i \frac{Q_{max_i} - Q_i}{Q_{max_i} - Q_{min_i}}$$

where $Q_i$ is the quality metric that needs to be optimized and $\chi_i$ is the weight assigned to the metric. The first summation term consists of the metrics that need to be maximized (cruise speed, weight efficiency, etc.) and the second summation term corresponds to those metrics that need to be minimized (gross weight, cost, etc.). In accordance with the requirements of the RFP, appropriate weights are assigned to each quality metric (Table 2.1).

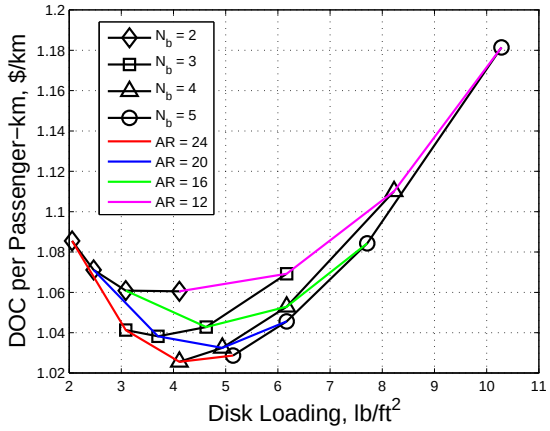


**Figure 2.3:** DOC vs. Disk Loading

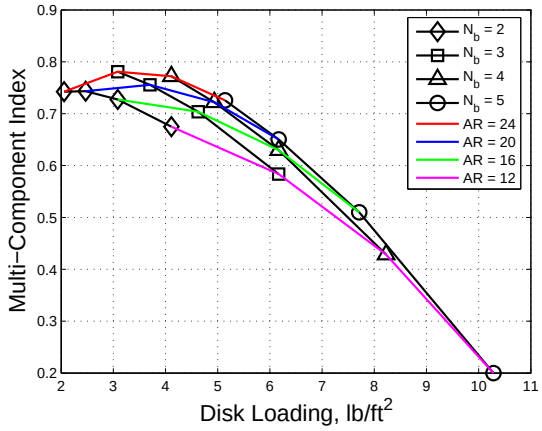


**Figure 2.4:** MCI vs. Disk loading

| Quality Parameter | Weight |
|---|---|
| Acquisition Cost | 0.45 |
| *DOC* per passenger kilometer | 0.15 |
| Cruise Speed | 0.15 |
| Gross Weight | 0.1 |
| Weight efficiency | 0.1 |
| Main rotor diameter | 0.05 |
| Total | 1.00 |

**Table 2.1:** Weights of Quality metrics

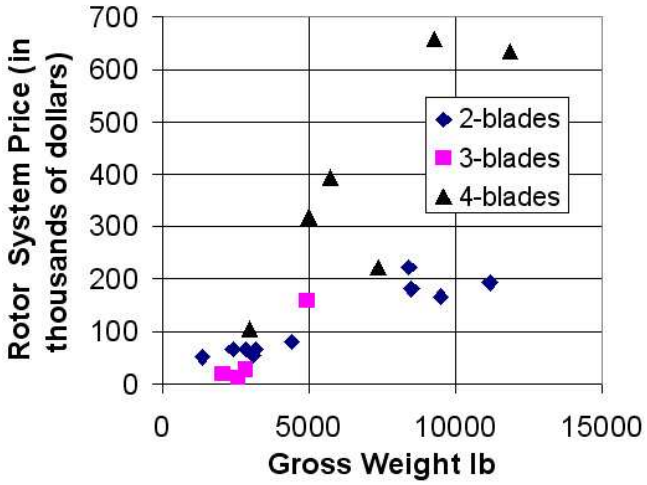


**Figure 2.5:** Comparison of Rotor System Cost

Figure 2.4 shows the Multi-component quality index versus disk loading. Based on this criterion, it is seen that a rotor having three blades with an aspect ratio of 24 gives the best overall results. Although an aspect ratio

of 24 is on the high side, it is still an acceptable value for this weight class of helicopters. For example, the Schweizer 300C and 300CB rotors also have an aspect ratio of 24 [3]. The use of droop-stops and composites (higher stiffness) in the main rotor design solves the problem of blade droop associated with high aspect ratios. Other possible alternatives are the two and four bladed rotors with an aspect ratio of 24. However, other factors influenced the choice of three blades. Three blades leads to reduced vibration levels and greater control authority compared to the two-bladed teetering rotor. With a teetering two bladed rotor, pilots have to be careful to avoid mast bumping. A three bladed hingeless rotor will not have this issue. Also, most new helicopters have three or more blades, so the need for the pilot to learn how to avoid mast bumping is becoming less relevant. The cost penalty in choosing three blades over two is minimal. A survey of helicopters from the Helicopter Blue Book [5] shows that opting for three blades instead of two blades does not necessarily lead to a higher rotor system cost (Figure 2.5) . However, moving to more than three blades leads to a significant cost increase.

Once the number of blades and aspect ratio are chosen, the next task is to decide on the blade loading ($C_T/\sigma$). For the same solidity and blade tip speed, an increased blade loading would result in higher disk loading, which in turn would lead to a smaller rotor diameter. Analysis showed that for a three bladed rotor with an aspect ratio of 24, increasing the blade loading from 0.07 to 0.08 decreases the gross weight slightly (because of the decrease in size related weights due to a decrease in diameter). However, increasing the blade loading from 0.07 to 0.08 is found to increase the hover power and fuel requirements because of the increase in disk loading. A higher disk loading also results in a lower autorotative index. Therefore, based on a detailed analysis, and keeping in mind the good autorotational performance required by the RFP, a moderate blade loading of 0.075 is chosen. This also provides a good stall margin, which in turn improves the maneuverability of the Penguin. Better maneuverability would prove useful for advanced training as required by the RFP.

Having fixed the number of blades, aspect ratio and blade loading, the final sizing depends on a reliable weight estimate of different helicopter components. The weight estimation procedure is first validated using the Tischenko method [2] to estimate the weights of the R22 helicopter components and compared with available data for the R22 [4]. A good correlation between the predicted and the actual R22 component weight values was obtained.

Wherever possible, a conservative weight estimate is made in order to account for the expected increase in empty weight when the helicopter enters the manufacturing/servicing stage. Special care has been taken to modify the weight estimates for additional design features/constraints. For example, the main rotor weight ($\approx 40$ lbs) increased because of the addition of 2.8 lbs of tip mass to each blade to improve autorotational performance. The increased centrifugal forces associated with the tip mass resulted in about 16 lbs increase in the rotor hub weight. The weight of the instrument system and batteries is also taken to be about 37 lbs more than that of the

R22 inorder to account for the enhanced instrument panel and the additional voltage required to start a turbine engine. The final gross weight of the Penguin is 1345 lbs (610 kg). This is lower than any existing certified helicopter. The use of an oil-free turbine design is the primary reason behind the low gross weight.

Based on the sizing and weight estimates, the power required to satisfy the RFP HOGE requirement (i.e., hover at 6000 ft alititude on an ISA $+20^{\circ}$ day) is found to be 125 hp. This is provided as input to the engine design. The engine analysis showed that in order to satisfy the aforementioned RFP HOGE requirement, the power available at ISA conditions at Mean Sea Level (MSL) is 165 hp. However, a high installed power can increase the drive-system weight significantly. Therefore, the engine is derated to 145 hp, thereby reducing the transmission weight and cost. However, care is taken to ensure that the derated engine provides adequate power that more than satisfies the RFP requirement to provide better forward flight performance than existing piston trainers.

| | |
|---|---|
| Number of blades | 3 |
| Aspect Ratio | 24 |
| Main Rotor Diameter | 23.36 ft (7.12 m) |
| $C_T/\sigma$ | 0.075 |
| Solidity | 0.0398 |
| Takeoff Weight | 1345 lbs (610 kg) |
| Empty Weight | 743 lbs (337 kg) |
| Empty Weight Fraction | 0.55 |
| Fuel Weight | 161 lbs (73 kg) |
| Engine Power (derated) | 145 hp (derated) |
| Disk Loading | 3.14 lb/$ft^2$ (15.35 kg/$m^2$) |

**Table 2.2:** Final Helicopter Sizing

Once the engine, transmission and electrical systems designs are finalized, the combined weight and sizing calculations are repeated. These are then refined by extracting volume information from the component drawings and specifying material/density. The weight breakdown for the Penguin is listed in the MIL-STD-1374 weight Statement. Table 2.2 provides the final sizing of the Penguin.

Having finalized on the weights and sizing, the longitudinal center of gravity (CG) of the Penguin is calculated based on CG locations of each component. The CG is calculated for two important cases:

- With pilot, passenger and payload (no fuel) the CG lies 4.75 in ahead of rotor hub axis.
- With just the pilot and fuel, the CG lies 2.53 in behind the rotor hub axis.

The CG always lies within a $5^{\circ}$ angle cone drawn from the center of the rotor hub. The CG location is used as input for the longitudinal trim code used for the performance analysis.

# 3 Main Rotor and Hub Design

## 3.1 Blade Aerodynamic Characteristics

The main rotor sizing, done using Tishchenko's method as described in Ch. 2 on preliminary sizing, resulted in the main rotor diameter, chord, solidity and tip speed (Table 3.1). The Penguin is expected to fly only at moderate forward flight speeds, hence sweep at the rotor tips can be avoided to reduce the blade manufacturing cost. The use of taper was also avoided in order to minimize the manufacturing cost.

The effect of blade twist on performance was studied using blade element momentum theory with empirical corrections to account for tip loss effects. Twist improves the hover performance, but it is not favorable for forward flight performance. Blade twist of $-11^\circ$ was chosen based on detailed studies for both hover and forward flight. Tip losses in hover are reduced by an anhedral of $10^\circ$, thereby improving the figure of merit by about 2–3%. The use of anhedral also reduces blade vortex interaction (BVI) noise by increasing the axial separation of tip vortices.

| | |
|---|---|
| Diameter | 23.36 ft (7.12 m) |
| Number of Blades | 3 |
| Chord | 0.97 (0.15 m) |
| Solidity | 0.04 |
| Twist | $-11^\circ$ |
| Anhedral | $10^\circ$ (from 95 %) |
| Tip speed | 672 ft/s (205 m/s) |
| Airfoil | SC1095 |

**Table 3.1:** Main Rotor Specifications

## 3.2 Blade Structural Design

**3.2.1 Blade Material.** The blade structure was designed to achieve the stiffness distribution required to carry the centrifugal force and both steady and oscillatory flap, lead-lag and torsional moments. The blade should also have adequate mass for autorotation. Composites are superior to metals in terms of specific strength, fatigue life and damage tolerance. Suitable composite ply layups can provide the blade favorable structural couplings. Therefore, the blade structure is made out of composite laminates. The composite materials considered are in Table 3.2. S-2 glass is the most affordable. However, it has low specific strength and stiffness when compared to Kevlar and Graphite. Kevlar is the lightest among the materials considered and it has good damage tolerant characteristics. However, it is susceptible to ultra-violet

| Material | Density (lb/$in^3$) | Young's Modulus (Mpsi) | Cost ($/lin. yard, 48" W) |
|---|---|---|---|
| S-2 Glass | 0.072 | 6.24 | 5.60 |
| Kevlar-149 | 0.05 | 12.62 | 16.50 |
| IM7 Graphite | 0.058 | 29.44 | 21.50 |

**Table 3.2:** Properties of Possible Composite Blade Materials

radiations and requires more complex bonding techniques. IM7 graphite was chosen for its superior specific stiffness and specific strength characteristics.

**3.2.2 Blade Structure.** The D-spar is the main structural element of the blade (Figure 3.2). The D-spar is mainly comprised of prepreg unidirectional plies running spanwise. At the blade root these plies are wound around the bushing for the two torque tube attachment bolts and the titanium sleeve for the lag pin. This forms a continuous load path for transferring the blade forces to the hub. The winding of the prepreg is automated. Automation and the use of prepreg ensure more uniform structural characteristics for all the blades and eliminates resin squeeze-out during winding. The D-spar extends from 2% chord to 38% chord location. 3 channel sections provide additional strength to the blade structure (Figure 3.2). They also help to maintain the airfoil shape of the blade skin. The first channel section extends from 38% to 45% chord location. It is constructed out of a symmetric layup of 6 [0/90] plies. The second and third channels extend from 57% to 63% and 70% to 75% chord location respectively. Both of them are made of 4 [0/90] plies laid symmetrically. Blade skin is made of 4 balanced [+45/-45] plies. The skin provides large torsional stiffness. The blade structure was designed such that the static droop of the blade is less than $4^{\circ}$. The torque tube rests on a droop stop when the blades are not rotating, which prevents the flexbeam from bending . Titanium erosion strips are mounted over the blade leading edge.

**3.2.3 Vibration Reduction with Structural Coupling.** Recent studies at the University of Maryland by Bao and Chopra [6], have shown the effect of pitch-flap structural couplings on the reduction of hub loads. Tests done on Mach scaled rotor of UH-60 showed reduction in vertical shear, in-plane shear and head moments by 14, 12 and 18% respectively. Couplings also led to a power reduction at high speeds due to the elimination of negative lift regions. Therefore, Penguin's rotor blade incorporates pitch-flap structural couplings. UMARC was used to obtain the optimum coupling for Penguin's rotor blade for the reduction of the vibratory loads. The 3/rev vibratory loads produced by Penguin's rotor blade are compared with a baseline uncoupled blade design in Figure 3.1. The outboard region (60%R to 100%R) of Penguin's blade has positive pitch flap coupling and the inboard region (13%R to 60%R) is uncoupled. The coupling is incorporated in the top and bottom flanges of the D-spar which are made of 14 plies. The top and the bottom flanges of the outboard region of the spar have the same ply layup of $[0_{10}/+15_4]$ to provide the required positive pitch-flap coupling. However, the flanges in the inboard region have a symmetric $[+15_2/0_{10}/-15_2]$ ply layup. The webs of the D-spar are also made of 14 plies. However, the web is uncoupled with $[+15_2/0_{10}/-15_2]$ ply layup.

**3.2.4 Leading Edge Mass.** A leading edge mass of 3.1 lb (1.4 Kg) is placed ahead of the D-spar to bring

the CG of the blade section close to the quarter chord location. The leading edge mass is a tungsten rod segment shaped as the leading edge, which is bonded to the spar and tightly held in place with the skin wrapped around it (Figure 3.2). This mass is equally distributed along the entire length of the blade.

**3.2.5 Tip Mass.** A Tip mass of 2.8 lb (1.3 Kg) is distributed from 90% radius to the blade tip inside the D-spar to improve the autorotative blade inertia. The tip mass is a tungsten rod inserted into the D-spar from the tip. The cross-section of the rod is shaped in such a way that the CG of the rod falls at 22% of the chord to avoid aeroelastic instabilities. The rod is firmly bolted on to the spar. The spar is strengthened locally around the bolts by adding 6 [90] plies. The whole blade structure is wrapped in the blade skin and cured in a closed cavity metal tooling. The total mass of a single blade including the tip mass is 13.4 lb (6.1 Kg).

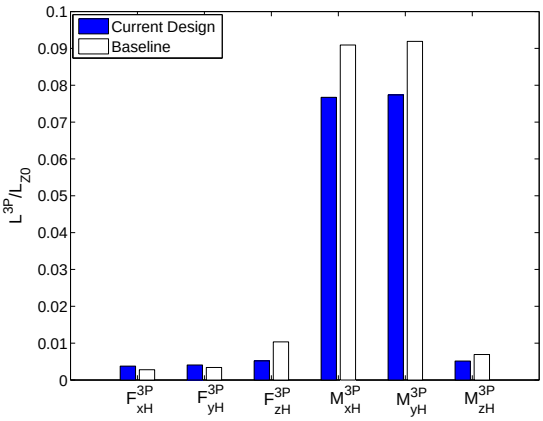


**Figure 3.1:** Elastic Coupling Vibration Reduction

**3.2.6 Trim Tab.** Trim tabs are used to track the blade in order to reduce vertical vibrations. Vibration sensors are mounted on the hub and airframe at optimized locations to capture various vertical vibration amplitudes. The vertical vibration sensor is positioned at the nose end of the cabin. The once-per-revolution source is a magnetic pickup mounted on the non-rotating swashplate. A ferrous metal interrupter passing in close proximity to the magnetic core produces an electrical impulse, which triggers the pickup. The time history of the vibrations is stored in the memory device on the helicopter. This data is then transferred to a ground station once the helicopter is landed. A software program specifically developed for Penguin does the balancing calculation using the amplitude and phasing of the various vibratory loads measured. The software identifies the tab to be adjusted.

**3.2.7 Lightning Protection.** The rotor blades are designed to be able to withstand a 200 kA lightning strike and be able to land safely [7]. Heating caused by the lightning strike can cause delamination of the composite blades. Aluminum mesh screens integral with the blade skin conduct the current from a strike to the titanium abrasion strip. The abrasion guard conducts the current to the blade root. A titanium strip connects abrasion guard to the hub lightning ground cable. This avoids any electrostatic charge build up on the blade.

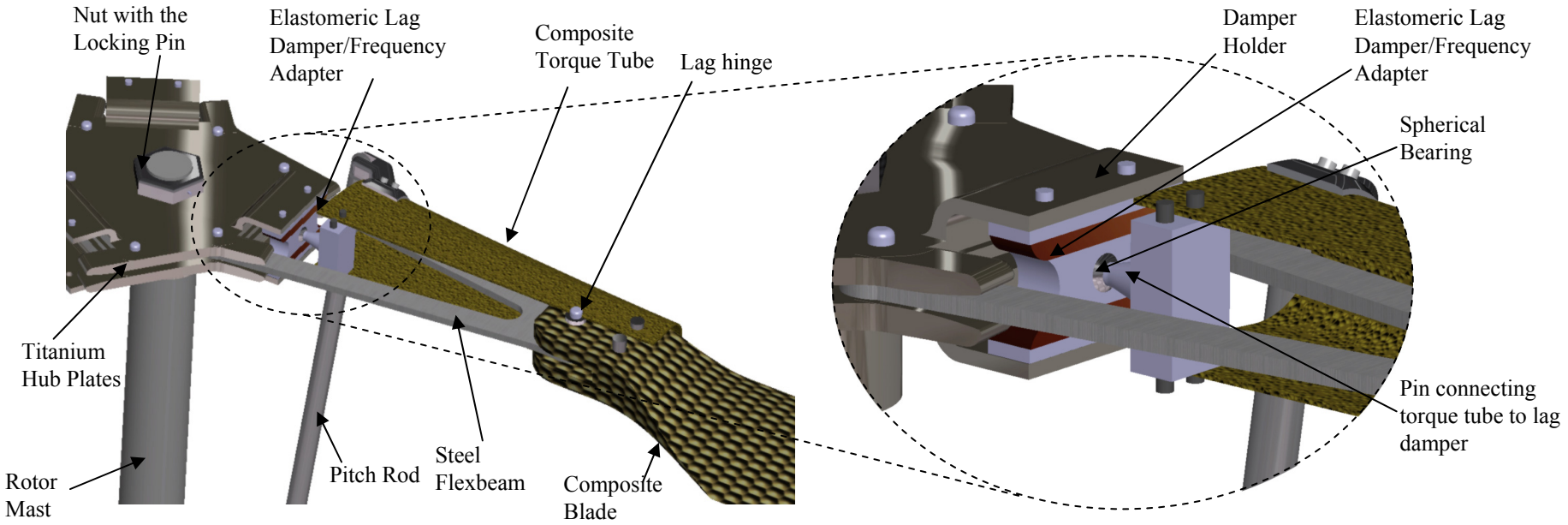


Note: -11° twist over the entire blade span

**Figure 3.2: Rotor Blade and Hub Detail**

## 3.3 Hub Design

For the hub design, emphasis was placed on mechanical simplicity, reduced cost of manufacture, reduced maintenance and low drag. A fully articulated hub with mechanical hinges has high parts count, high drag and high maintenance cost. Elastomeric bearings can eliminate mechanical hinges and can provide more than one degree of articulation resulting in a more compact design. Such a system also requires low maintenance. However, elastomeric bearings are relatively expensive and require hydraulics to enable pitch actuation. A pure bearingless design uses a flexbeam which is tailored to give the required flap, lag and pitch articulations. The design, testing and certification of such a flexbeam can be an expensive process. Therefore, in the Penguin hub, the flexbeam accommodates only the flap and torsion motion. The lag motion is accommodated by a mechanical lag hinge at the end of the flexbeam. An elastomeric lag damper/frequency adaptor is attached near the root of the flexbeam. The hub consists of the following components (Figure 3.2):

**3.3.1 Hub Plates.** The machined titianium hub plates were sized to carry the static and oscillatory forces and moments transferred to it from the blade through the flexbeam. The hub plates have curved lips in the regions above and below the flexbeam to avoid stress concentrations when the flexbeam bends in flapping. The axis of the flexbeam is aligned such that it does not pass exactly through the axis of the mast (Figure 3.3). This pre-lag built into the hub plate is equal to the constant lag angle of the blade in hover. This is done so that when the blade lags due to drag, the axis of the blade is aligned along the axis of the flexbeam. Therefore, the forces acting on the blade pass through the axis of the flexbeam, causing both arms of the flexbeam to take equal axial loads. The two plates are bolted together with the flexbeam between them (Figure 3.2). The rotor mast passes through a splined hollow boss in the center of the bottom plate and the whole hub aligns with the mast. The 30 splines were designed to take twice the maximum torque from the gearbox. The top plate has a clearance hole in the center which allows the shaft to pass through it and is tightly secured on the top using a nut and a pin locking system. The drive shaft has an outer diameter of 2.25 in and inner diameter of 1.75 in.

**3.3.2 Flexbeam.** The flexbeam consists of a stack of 20 Y-shaped steel 40 mil (1 mm) thick laminae bolted to the hub plates. The stack of plates was used because it provides a very low torsional stiffness so that hydraulic actuators are not required for pitch actuation. UMARC was used to obtain the oscillatory stresses for level flight at an advance ratio of 0.2 at the flexbeam root (Figure 3.4). The flexbeam was designed to handle these stresses with the stress amplitude being 0.39 times the endurance stress limit.

**3.3.3 Torque Tube.** The torque tube is connected to the blade root at the outboard end and to the pitch link

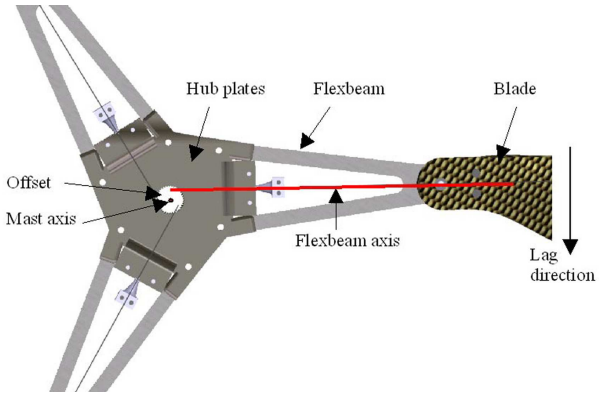


**Figure 3.3:** Hub Pre-Lag Offset

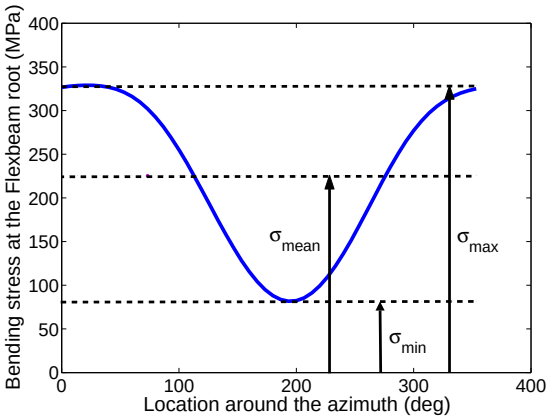


**Figure 3.4:** Flexbeam Oscillatory Stresses

and lag damper at the inboard end as shown in Figure 3.2. The torque tube is stiff in flap, lag and torsion. It is constructed out of 26 [+45/-45] graphite epoxy plies. The linear motion of the pitch link rotates the torque tube about the pitch axis providing the blade pitch actuation.

**3.3.4 Elastomeric Lag Damper/Frequency Adaptor.** Compared to hydraulic dampers, elastomeric dampers have long service life, high reliability and low maintenance/inspection requirement. They work efficiently over a range of temperature from $-65°$F to $+200°$F. [8] In order to avoid the maintenance problems associated with hydraulic dampers, an elastomeric lag damper was chosen. The lag damper is attached between two extensions from the hub plates as shown in Figure 3.2. There is a spherical bearing at the center of the lag damper. The inboard end of the torque tube is connected to this spherical bearing through a pin that allows the flapping and pitching of the blade. This acts as the pitch axis. When the blade leads or lags, it will shear the alternate rubber and metal layers in the lag damper thus providing damping.

## 3.4 Rotor Dynamics

The dynamic characteristics of the blade and the flexbeam were tuned to place the frequencies at suitable locations on the fan plot to avoid aeromechanical instabilities

**3.4.1 Dynamic Analysis.** UMARC was used to obtain the blade frequencies. The blade and the flexbeam were modeled with 16 and 4 finite elements respectively. The stiffness and the mass distributions of the blade are given in Figure 3.5. The fan plot (Figure 3.6) shows that the important rotating natural frequencies of the blade are well separated from the rotor harmonics at the operational RPM. The blade natural frequencies are given in Table 3.3.

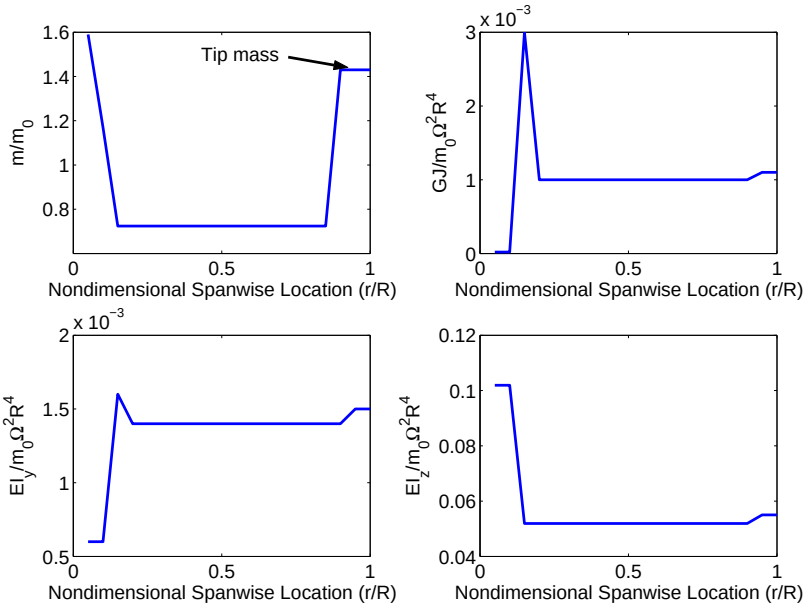


**Figure 3.5:** Blade Stiffness and Mass Distribution

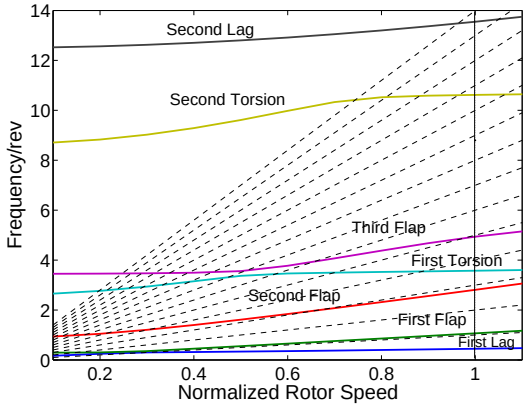


**Figure 3.6:** Rotor Fan Plot

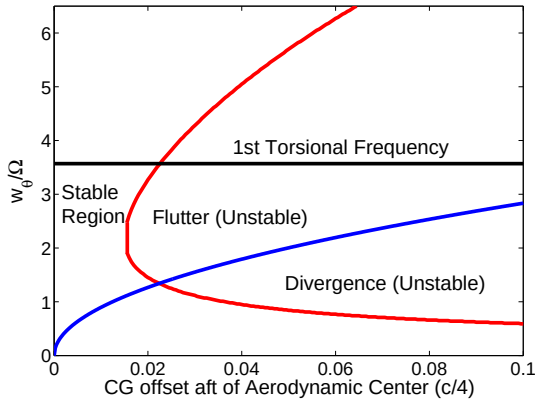


**Figure 3.7:** Pitch-Flap Flutter/Divergence Stability Boundaries

**3.4.2 Aeroelastic Analysis.** Pitch-flap flutter and divergence analysis [9] was performed to ensure that the rotor is free from any aeroelastic instability. The analysis indicated that the critical c.g. location to prevent pitch-flap flutter and divergence is 27.5% from the leading edge (Figure 3.7). The tip mass weight moves the c.g. ahead to 22% chord location. This provides adequate margin to avoid pitch-flap flutter and divergence.

| Mode | Flap | Lag | Torsion |
|---|---|---|---|
| First | 1.06 | 0.45 | 3.57 |
| Second | 2.84 | 13.54 | 10.61 |
| Third | 4.87 | - | - |

**Table 3.3:** Main Rotor Blade Natural Frequencies

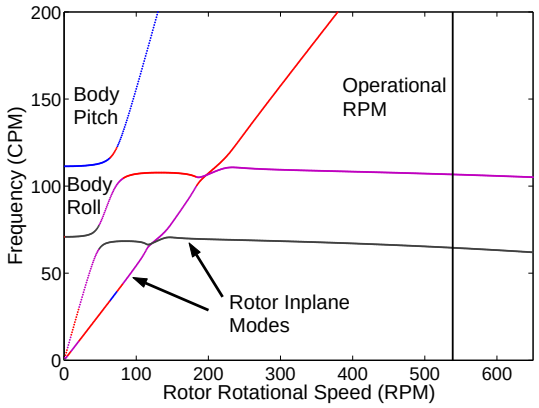


**(a)** Frequency

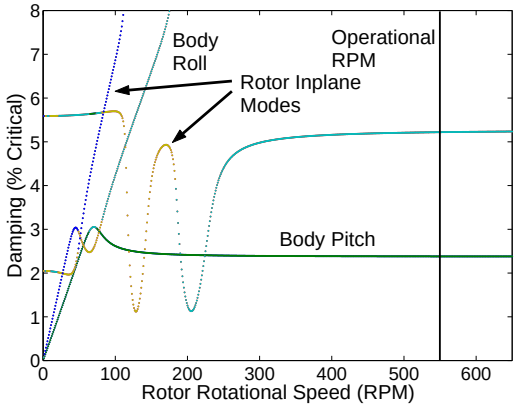


**(b)** Damping

**Figure 3.8:** Ground Resonance Analysis

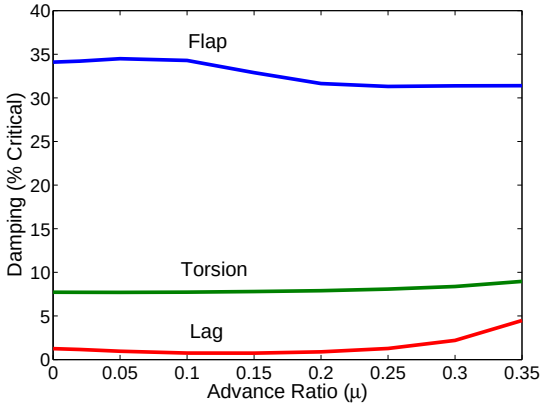


**Figure 3.9:** Flap/Lag/Torsion Analysis

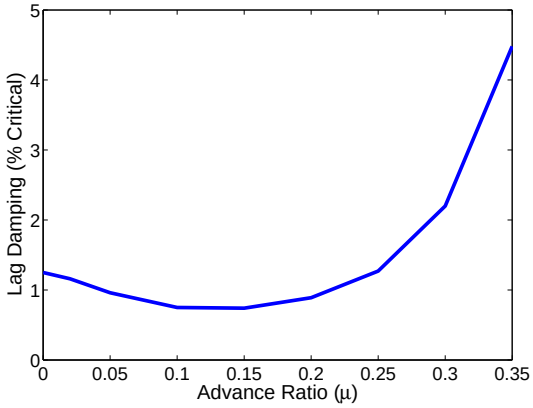


**Figure 3.10:** Air Resonance Analysis

**3.4.3 Ground and Air Resonance.** A ground resonance analysis [9] was performed to ensure that body frequencies and the lag frequencies do not coalesce near the operating RPM. The analysis showed that the frequencies are well separated near the operating RPM and all the modes are adequately damped (Figures 3.8). A comprehensive air resonance analysis was performed and showed in (Figures 3.9, 3.10) that rotor lag modes remain stable even in the absence of elastomeric damper for all the advance ratios. Inclusion of the auxiliary elastomeric lag dampers would further augment the stability of the lag modes.

# 4 Tail Rotor

The tail rotor is sized using Tishchenko method. The tail rotor diameter was initially estimated by assuming it to be a fraction (1/5th to 1/7th) of the main rotor diameter. The solidity of the tail rotor is then estimated based on the thrust required to counteract the main rotor torque. Assuming a moderate blade loading ($C_T/\sigma$) of 0.075 and

fin interaction losses of 6%, the tail rotor aspect ratio and the corresponding chord are computed for the given thrust requirements. It was found that a main-rotor-tail-rotor diameter ratio of 6.5:1 provides realistic aspect ratios with two tail rotor blades. Symmetric airfoil was chosen to limit pilot control loads. Linear twist of $-8^\circ$ was used to improve the aerodynamic performance of the tail rotor. Pusher rotor reduces the penalties associated with vertical fin blockage. Aft-at-the-top rotation minimizes tail rotor interaction with the main rotor [10].

Table 4.1 shows the basic sizing of the tail rotor. The tail rotor hub structure consists of a straight laminated metal torsion bar mounted within a socket attached to the hub - the arms of which accommodate centrifugal forces, and also serve to transmit torque from the driveshaft to the blades. The hub is constructed of steel, while the torsion bar is constructed of Titanium. The pilot pedal control input is fed to a non-rotating shaft which is connected to a rubber boot. The rotating shaft is connected to the fixed shaft-boot structure through a spherical bearing. A $\delta$-3 coupling of $45^\circ$ is provided to minimize blade flapping.

| | | | |
|---|---|---|---|
| **Diameter (ft)** | 3.59 | **Number of Blades** | 2 |
| **Chord (ft)** | 0.27 | **Solidity** | 0.095 |
| **Blade Twist (deg)** | -8 linear | **Tip Speed (ft/s)** | 672 |
| **Shaft RPM** | 3592 | **Airfoil Sections** | NACA 0012 |
| **Type** | Pusher | **Direction of Rotation** | Aft-at-the-top |

**Table 4.1:** Tail Rotor Specifications

# 5 Variable Handling Qualities

In a trainer helicopter, it is desirable to have the option to change the "feel" or, the handling qualities of the helicopter. Variable handling qualities (VHQ) offers the pilot an inexpensive installed-standard system for this. VHQ allows the Penguin to emulate the handling qualities of different classes of helicopters. A beginner pilot can learn with the best handling qualities and then progress to a more difficult level in the same helicopter.

## 5.1 Approaches to Variable Handling Qualities

There are several ways of implementing a VHQ scheme on a helicopter. The most common and intuitive approach today involves a model following algorithm implemented in the flight control software, as has been done for CH-47B variable stability helicopter [11] and the RASCAL program [12]. Such a state-of-the-art approach, although very suitable for application on a trainer helicopter, can only be implemented on a platform with a full electronic (fly-by-wire or fly-by-light) flight control system.

Long before the advent of modern control systems, Arthur Young designed the stabilizer bar, and Stanley Hiller, the servo-paddle system to mechanically alter the handling qualities of a helicopter. These systems use

feedback from inertial or aerodynamic components to introduce a desired amount of phase change in the helicopter response [13]. Later, several other mechanical control systems [14] were suggested to achieve similar results. One such mechanical system is the damper based phase-lead compensator [15], as shown in Fig. 5.1(a), which can be incorporated in the cyclic control push-pull rods. It has been tested on the lateral, fore and aft systems of an H-13 helicopter, and was shown to be more effective than a control gyro, because it does not alter the maximum obtainable rates, the control sensitivity, or increase the inherent gust sensitivity of the aircraft [15].

In its original form, this system was used as a 'control quickener' to achieve shorter time constant. For a trainer helicopter, a 'quickener' (phase-lead), as well as a phase-lag element is desired, so as to emulate the response of helicopters with both, better and worse handling qualities than the given platform. Therefore, several innovative modifications have been made before adopting this system for Penguin.

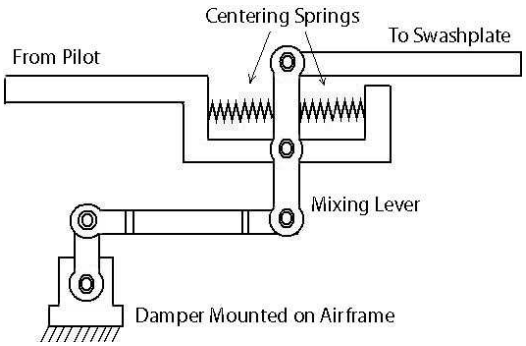


**(a)** Schematic of Mechanical Quickener

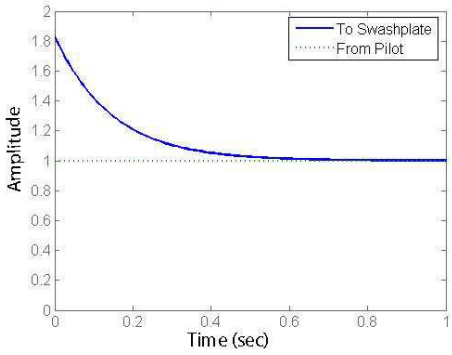


**(b)** Step Response of Mechanical Quickener

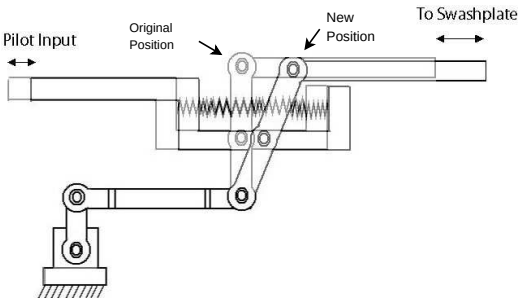


**(c)** Instantaneous Response to Step Input

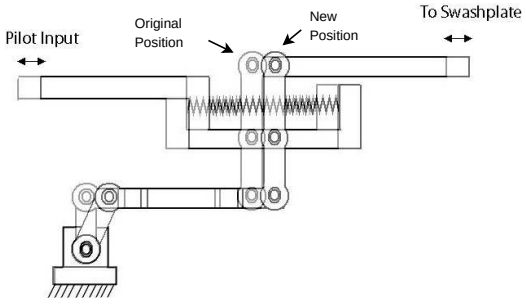


**(d)** Steady State Response to Step Input

**Figure 5.1:** Mechanical Phase-Lead Compensator

## 5.2 Mechanical Phase-Lead System

The schematic for a quickener system is shown in Fig. 5.1(a). When the pilot moves the stick, the damper does not move instantaneously, and causes the mixing lever to overshoot the pilot's motion as shown in Fig. 5.1(c). Then, as the final angular rate (steady state, as commanded by the pilot) is reached, the centering springs re-center the mixing lever and reduce the control to pilot input level (Fig. 5.1(d)). A first order model was derived for this configuration from first principles, and a Laplace domain transfer function from pilot input to swashplate output was obtained. A time history of step response is shown in Figure 5.1(b). The control overshoot directly increases the control power, or angular acceleration per unit control input. The Bode plot for this system in Figure 5.4(a), shows how this system effectively works as a phase-lead compensator.

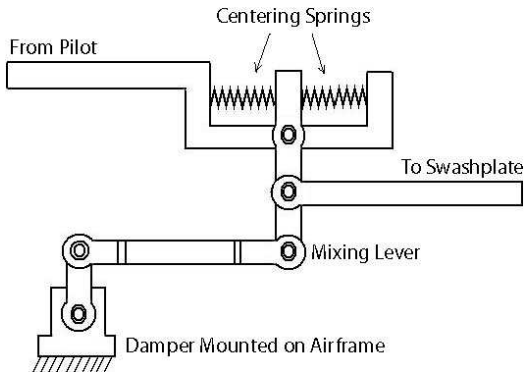


**(a)** Schematic of Phase-Lag System

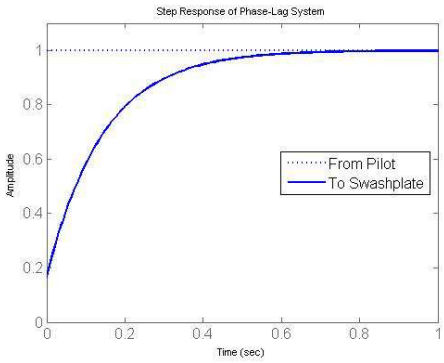


**(b)** Step Response of Phase-Lag System

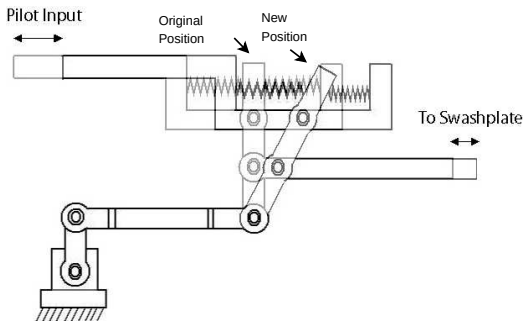


**(c)** Instantaneous Response to Step Input

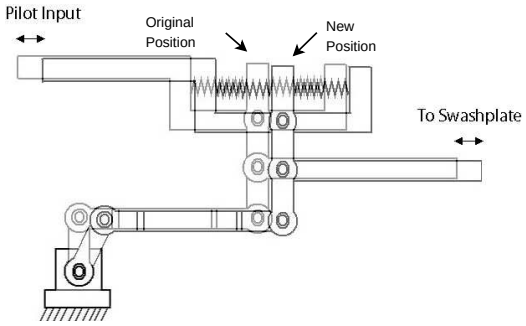


**(d)** Steady State Response to Step Input

**Figure 5.2:** Mechanical Phase-Lag Compensator

# Figure 5.3: Control System Layout

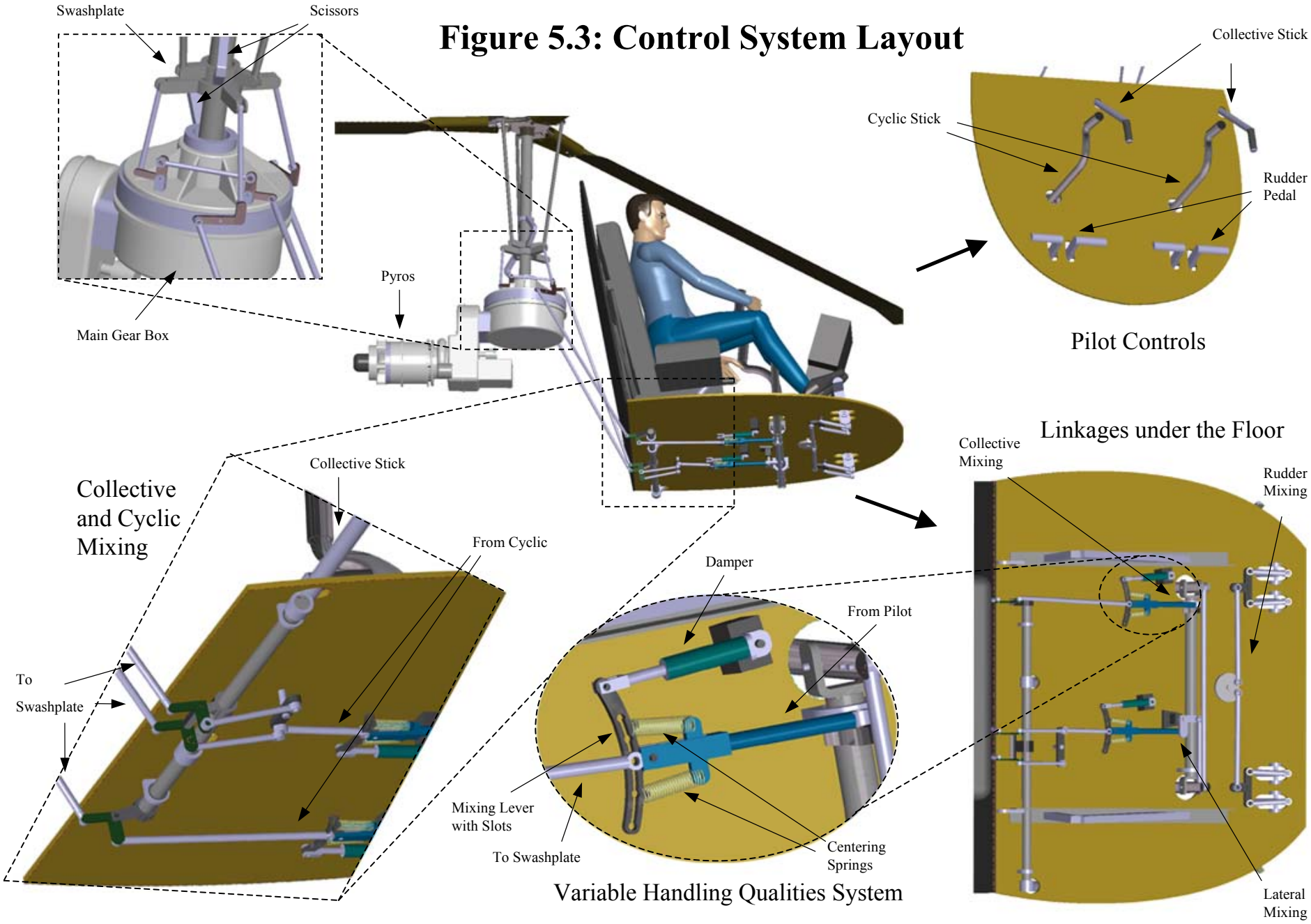

## 5.3 Mechanical Phase-Lag System

By sliding a single linkage on the mixing lever, as shown in Fig. 5.2(a), the same basic system can be made to work like a phase-lag filter (Bode plot shown in Fig. 5.4(b)). As before, the damper does not move instantaneously, but now initially leads to an undershoot of the pilot input, as shown in Fig. 5.2(c). In the steady state, the centering springs re-center the mixing lever, and the final angular rate is achieved (Fig. 5.2(d)). The time history of a step response is shown in Fig. 5.2(b). This system introduces a pair of pole and zero in the left half plane, such that the pole is closer to the imaginary axis than the zero. This results in reduced bandwidth of the system.

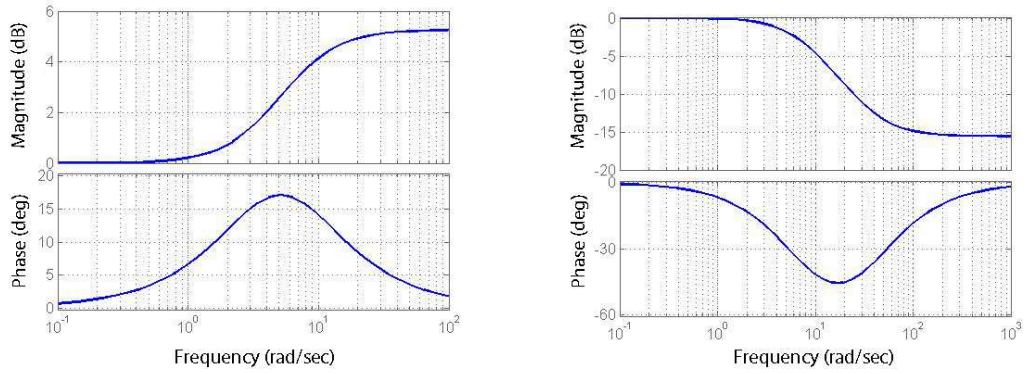


**(a)** Bode Plot of Mechanical Phase-Lead System **(b)** Bode Plot of Mechanical Phase-Lag System

**Figure 5.4:** Bode Plots of Mechanical Lead and Lag Compensators

## 5.4 Hybrid Lead-Lag Compensator Design for Penguin

Fig. 5.3 shows the mechanical control system that can work both as a lead as well as a lag filter by moving the output push-pull rod (connected to the swashplate) to different slots on the mixing lever. Bandwidth is one of the most important criteria used for evaluation of handling qualities of a helicopter, as identified by Aeronautical Design Standard (ADS-33E) [16]. Typically, higher bandwidth corresponds to better handling qualities. ADS-33E defines the overall bandwidth as the smaller of the phase bandwidth and gain bandwidth.

The effect of the mechanical lead-lag compensator (the VHQ system) in nominal and extreme slot positions on a hingeless helicopter's (BO-105) roll bandwidth is shown in Fig. 5.5(a). Gain Bandwidth for this system is undefined (the phase plot crosses the -180° line at infinity), and therefore, phase bandwidth is the overall bandwidth of the system. Fig. 5.5(b) shows an example of how handling qualities, as given by the bandwidth and phase delay criteria of ADS-33E (target acquisition and tracking), can be significantly altered by this system.

Penguin is equipped with such mechanical lead-lag compensators on both, longitudinal and lateral cyclic

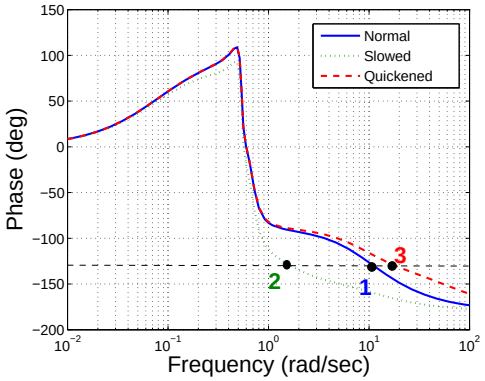


**(a)** Bode Plots (Phase Bandwidth)

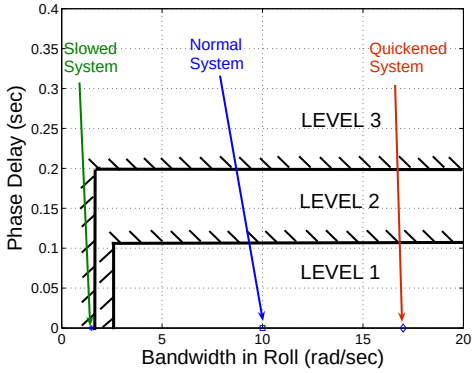


**(b)** ADS-33E Bandwidth and Phase Delay Criteria (Target Acquisition and Tracking (Roll))

**Figure 5.5:** Effect of Mechanical Lead-Lag Compensator on Roll Bandwidth of BO-105 for Hover

controls (Fig. 5.3). There are five slot positions for five different settings; two for the "quickened" response, two for 'delayed', and a center position for normal operation without any phase compensation. An access panel is provided in the cockpit so that the output rod can be easily switched between different slots, as desired by the instructor. The system installation is fail-safe in terms of damper or centering spring failure. In the case of a loss of hydraulic pressure in the damper, a lock-out device centers the unit. Hydraulic bypass valves are placed in the lock-out lines, so that the pilot can switch the system off and on, easily during flight in case of emergency.

In the later stages of design, a more detailed analysis of the effect of this system on dynamics of Penguin would be performed. A better correlation between handling qualities of Penguin for different slot positions, handling qualities of existing helicopters can be established, and operators can be provided with information suitable for *ab initio* and advanced training.

# 6 'Pyros' Engine

## 6.1 Configuration Selection

The Pyros is a two-spool turboshaft engine. The engine layout and the exploded views are shown in Foldout 3. The following are the major components of the engine:

- Bell mouth inlet with inlet filter.
- Gas generator section:
  - Single stage radial compressor.
  - Reverse flow annular combustor.

    - Single stage radial high-pressure (HP) turbine.
- Power section:
    - Single stage axial low-pressure (LP) turbine.
- Exhaust duct.

The compressor and high pressure (HP) turbine are mounted on a single shaft. The free turbine is mounted on a separate shaft with no mechanical connection between the two shafts. Both shafts are supported by radial and thrust foil air bearings. This configuration avoids the usage of any concentric shafts and has the following advantages over other configurations:

- The power turbine is separated from the gas generator section. This prevents any sudden loads from propagating to the gas generator, which could result in an undesirable compressor/turbine operational mode.
- It allows the use of solid compressor and turbine disks with no internal bores which reduces the size of the rotating components and results in a compact engine with high specific power.
- The power turbine output shaft can be located close to the transmission gearbox.
- The hot section can be completely separated from the cold section of the engine by disassembling at just one location. This allows for easier maintenance.

**6.1.1 Inlet.** The function of the inlet is to provide clean air to the impeller with minimal pressure losses. A bell mouth inlet is used to provide smooth air in the axial direction to the compressor. The air intake is almost at zero velocity. The inlet has a particle separator to expel contaminants separated by centrifugal force.

**6.1.2 Radial Compressor/Turbine.** The Pyros uses a single stage radial compressor-turbine combination in the gas generator section. In the size range of small engines like the *Pyros* (0.5 to 5 lbs/second of air/gas flow), radial flow impellers offer minimum surface and end wall losses. Radial compressors/turbines can handle small volumetric flow of air with higher component efficiency as compared to axial devices. They are significantly lower in unit cost for the same flow capacity and pressure ratio. Finally, they deliver significantly larger compression/expansion ratio per stage, and are considerably shorter for a given mass flow, making for a more compact engine. Surge is an additional consideration for compressors. A radial compressor has better low speed surge characteristics than multi-stage axial compressors. This eliminates the need for accessories like bleed valves, variable inlet guide vanes and variable stator vanes, required to avoid low speed surge problems. This reduces overall engine cost and weight.

**6.1.3 Reverse Flow Annular Combustor.** The Pyros has an annular reverse flow combustor with radially arranged fuel injectors. When compared to a can-annular configuration, it allows for a clean aerodynamic design, with lower cooling air requirements while eliminating the need for transition ducts between the combustor and the turbine, and as many accessories like igniters and fuel injectors. However, such a configuration would result in less uniform temperature distribution at the exit affecting turbine durability.

The advantages offered by the annular combustors make it a popular choice for almost all the well established turboshaft engines. The reverse flow configuration incurs higher pressure losses but results in a compact engine with a short gas generator shaft.

**6.1.4 Axial Flow Free Turbine.** The selection of axial flow turbine as the free turbine was determined primarily by the advantage obtained by the elimination of complex ducting needed to direct flow from one radial turbine to another, which would otherwise be the case with the selection of a radial turbine for the power turbine.

## 6.2 Engine Cycle Design

**6.2.1 RFP requirements.** In order for the Penguin to satisfy the RFP requirements, the engine is required to develop a power output of 125 hp (93.2 kW) at an altitude of 6000 feet on an ISA+20°C day.

The chief variables to be considered in a turboshaft engine cycle design are the compressor pressure ratio and turbine inlet temperature. These two factors determine engine specific power and specific fuel consumption. Specific power determines engine size while SFC determines engine operating cost. Since the trainer helicopter is a light weight, low payload vehicle it is important to optimize the engine specific power so as to achieve a light weight engine. A parametric study of the design space was carried out to determine the pressure ratio and turbine inlet temperature for the turboshaft engine that maximizes specific power while providing a reasonable SFC. Constraints were placed on the maximum pressure ratio and turbine inlet temperatures that could be used in the engine due to limits on overall engine cost, design complexity and the available technology level. The radial compressor design places an upper limit on the compression ratio that can be employed in the engine cycle. Commercial radial compressors have been built to give compression ratios up to 8 and research grade compressors give compression ratios as high as 11.

Turbine inlet temperature is the most important variable in maximizing engine performance. Much of the development in gas turbine technology over the years has been in advancing materials and technologies to operate at high turbine inlet temperatures. Improvements in materials technology have enabled blades to operate up to 1300 K (1880 F) without using blade cooling. Current state-of-the-art cooling technology has allowed engines to operate with turbine inlet temperatures as high as 1700 K (2600 F). However, this adds complexity and cost

| | Value | Units | Value | Units |
|---|---|---|---|---|
| Power | 125 | hp | 93.21 | kW |
| Gas generator speed | 100,000 | RPM | 100,000 | RPM |
| Power turbine speed | 75,900 | RPM | 75,900 | RPM |
| Mass flow rate | 1.12 | lb/s | 0.51 | kg/s |
| Fuel consumption | 11.59 | gal/hr | 32.37 | kg /hr |
| Turbine inlet temperature | 1790 | F | 1250 | K |
| Compressor pressure ratio | 7 | N/A | 7 | N/A |
| Specific fuel consumption | 0.625 | lb/hp-hr | 0.381 | kg/kW-hr |

**Table 6.1:** Engine Design Point Parameters at 6000ft and ISA+20°C

to the engine design. In the design of the Pyros, the maximum turbine inlet temperature was limited to 1250 K (1790 F) in order to have a factor of safety between the design point and the material temperature capability.

The parametric analysis, cycle design and off-cycle analysis were carried out using a commercially available software called GASTURB. This software uses traditional engine cycle analysis methods and incorporates them into a menu driven easy-to-use graphical user interface. The user enters the inputs for the cycle, which include the engine component layout, the thermodynamic cycle, operating conditions, and component efficiencies. The software can be used to do a parametric study of the design variables and to evaluate engine design point as well as off-design performance. Compressor and turbine operating maps can be input in order to establish operating lines for these components. In the present analysis, reference compressor and turbine operating maps from GASTURB were used to determine the operating lines.

**6.2.2 Parametric Study.** The two variables chosen for the parametric study were the compressor pressure ratio and the turbine inlet temperature. The results of the parametric study are shown in Fig. 6.1 where specific power is plotted against SFC for a range of compressor pressure ratios and turbine inlet temperatures. The contours in blue correspond to lines of constant turbine inlet temperature while the contours in red correspond to lines of constant compressor pressure ratio. Optimum engine performance is obtained by maximizing specific power and minimizing power specific fuel consumption. The figure shows that increasing turbine inlet temperature and compressor pressure ratio have favorable effects on engine performance. Since the primary objective is to maximize specific power, the turbine inlet

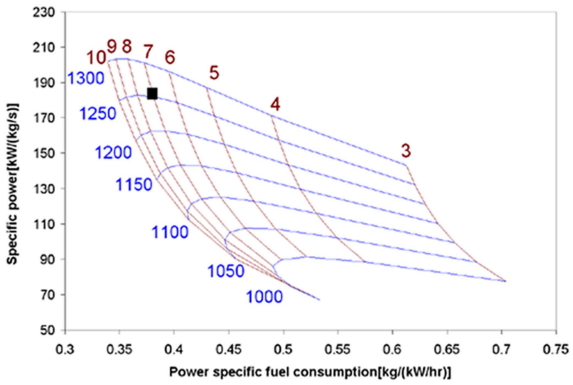


**Figure 6.1:** Results of Parametric Study of Turboshaft Cycle from GASTURB

temperature is chosen to be the highest permissible value (1250 K for uncooled blades). At any set value of turbine inlet temperature, increasing compression ratio from 3 to about 8 is found to improve performance. Beyond this, increasing compression ratio gives a marginal improvement in SFC but has a detrimental effect on engine specific power. Based on recommendations of Eames and in accordance with the limit of current technology, the compression ratio was set to be 7 [17]. Another design variable is the engine operating speed. The Pyros is designed to run at a high operating speed of 100,000 RPM at rated power. A high operating speed means that the sizes of the compressor and the turbine disks can be made small allowing an overall reduction in engine size and weight.

| | Value | Units | Value | Units |
|---|---|---|---|---|
| No. of stages | 1 | N/A | 1 | N/A |
| Pressure ratio | 7 | N/A | 7 | N/A |
| Speed | 100,000 | RPM | 100,000 | RPM |
| Mass flow | 1.12 | lb/s | 0.51 | kg/s |
| No. of stages | 1 | N/A | 1 | N/A |
| Pressure ratio | 2.68 | N/A | 2.68 | N/A |
| Speed | 100,000 | RPM | 100,000 | RPM |
| Mass flow | 1.12 | lb/s | 0.51 | kg/s |
| Max. inlet temp. | 1790 | F | 1250 | K |
| No. of stages | 1 | N/A | 1 | N/A |
| Pressure ratio | 2.27 | N/A | 2.27 | N/A |
| Speed | 75,900 | RPM | 75,900 | RPM |
| Mass flow | 1.12 | lb/s | 0.51 | kg/s |
| Max. inlet temp. | 1389 | F | 1250 | K |

**Table 6.2:** Design Operating Characteristics of Engine Components

**6.2.3 Design Point Calculation.** The next step in the design was to calculate the parameters for the engine design condition. The engine mass flow was iterated to achieve the required power output at the operating conditions specified by the RFP and at the design values calculated earlier for compressor pressure ratio, turbine inlet temperature and operating speed. Table 6.1 gives the engine design performance parameters and Table 6.2 gives the design operating characteristics of the engine components.

**6.2.4 Off-Design Analysis.** An off design analysis was carried out to determine the engine performance at different turbine inlet temperatures. The relevance of this analysis arises from the fact that turbine inlet temperature is the chief engine control variable. This analysis helps to establish the operating lines for the compressor and for the radial and axial flow turbines.

The operating lines are plotted on reference charts for the components. They help determine the surge margin and component efficiency at each operating point. Figures 6.4 6.2 and 6.3 show the operating maps for the compressor, radial inflow turbine and the axial turbine. component pressure ratio is plotted as a function of mass flow rate. Constant speed and constant effi-

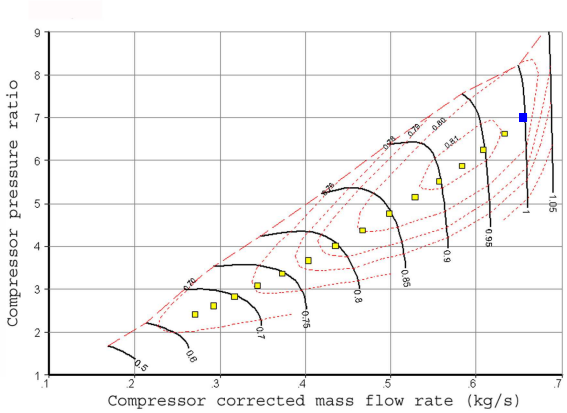


**Figure 6.2:** Compressor Operating Map

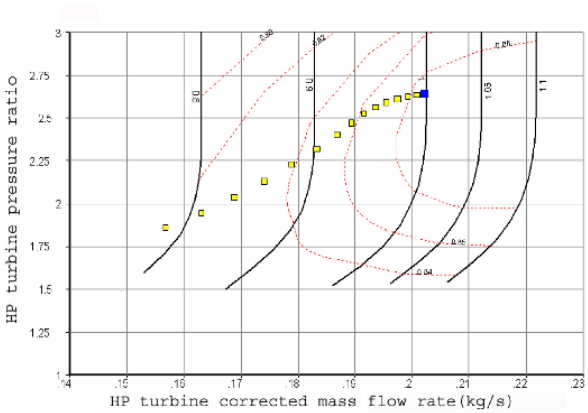


**Figure 6.3:** Radial HP Turbine Operating Map

ciency contours are marked on the plots. Component operating maps are an integral part of predicting gas turbine performance at design and off-design conditions. The contours in red are lines of constant efficiency while the contours in black are lines of constant speed. The yellow squares refer to the operating points of the components at different operating points of the engine. As seen, component efficiency is close to the highest achievable at the design point (blue squares) and decreases as the engine is operated away from the design point.

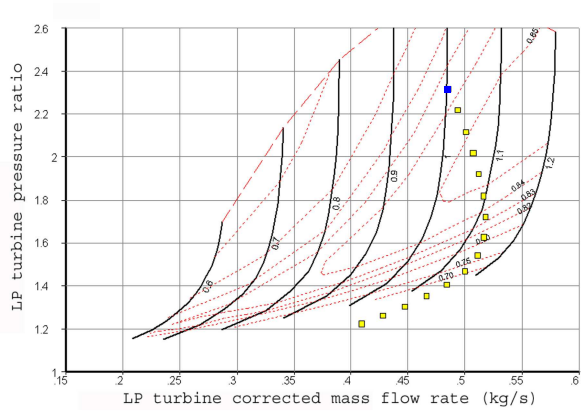


**Figure 6.4:** Axial LP Turbine Operating Map

**6.2.5 Altitude Performance.** A study was carried out to establish altitude performance charts for the engine. These charts are useful in guiding the helicopter pilot as to the operational envelope of the engine. They also help in overall design of the helicopter as well as optimizing other systems such as the engine control system and the transmission system. The GASTURB off-design performance codes were used to determine altitude performance. These charts are presented in figures 6.5 and 6.6.

## 6.3 Compressor Design

The following are the components of the radial compressor:

- Open faced impeller disk with backward curved vanes: There is no pre-whirl imparted by inlet guide vanes (IGV) and the flow enters the impeller blades axially.
- Radial first stage diffuser: The diffuser is designed as a single stage radial diffuser with a vaneless space.

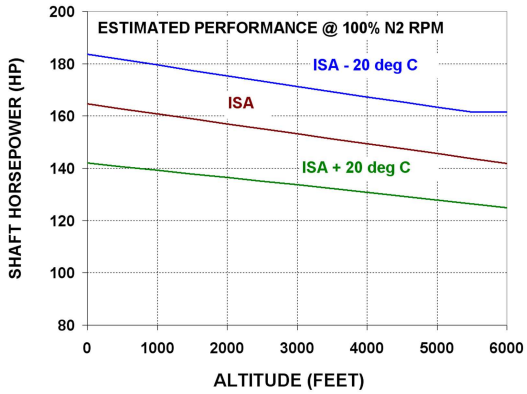


**Figure 6.5:** Engine Altitude Performance - Power Output

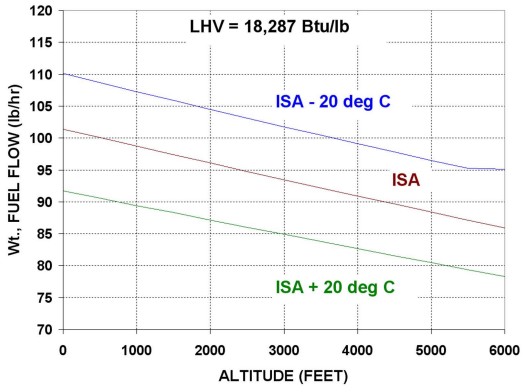


**Figure 6.6:** Engine Altitude Performance - Fuel Consumption

The vaned diffuser is designed as a low-solidity diffuser. The diffuser reduces exit swirl before the flow enters the combustion chamber. The gas turns 90° from radial to the axial direction downstream of the diffuser.

- Second stage axial diffuser: This is an axial stage that allows the flow to remain attached beyond the 90° turn and removes most of the remaining exit swirl before the gas enters the combustor. There is minimal pressure loss incurred when the flow turns and it allows for a more compact system.

**6.3.1 Impeller Disk.** The impeller is designed as a 14 bladed open-faced impeller. Fig. 6.7 shows the front and side views of the impeller. A mean line analysis was used to carry out a preliminary sizing of the impeller.

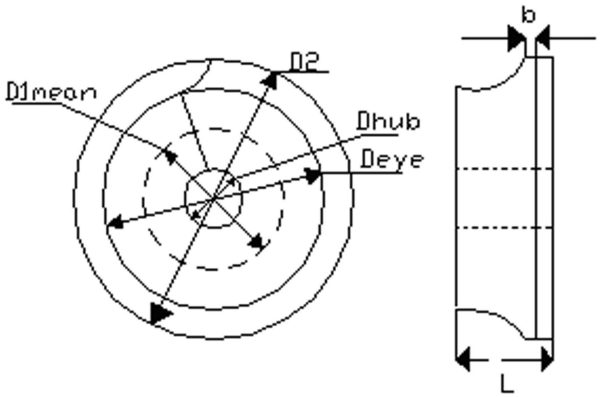


**Figure 6.7:** Impeller Layout

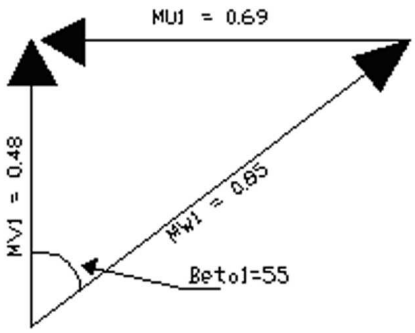


**Figure 6.8:** Inlet Velocity Triangle

The impeller blades are twisted at the inlet with an angle of 55° at the mean inlet diameter. This angle is low at the hub and increases towards the eye. Air enters the impeller axially with no pre-whirl component. The blades are curved backward at the exit. This allows a higher surge margin since pressure head decreases with increasing

flow rate for this type of impeller. The inlet relative Mach number is fixed at 0.85. The inlet velocity triangle with the corresponding Mach numbers is shown in Fig. 6.8 . A slip factor equal to 0.82 is assumed in accordance with the Balje slip factor [18]. The required pressure ratio of 7 and the operating speed of 100,000 RPM gives a tip speed of 1800 ft/s according to the following equation [19]:

$$U_2 = \sqrt{\frac{\gamma R T_{01}}{\mu(\gamma-1)}\left(\left(\frac{P_{02}}{P_{01}}\right)^{\frac{\gamma-1}{\gamma}} - 1\right)} \tag{6.1}$$

where,

$U_2$ =Impeller tip speed $\gamma$=Ratio of sp. heats

$R$=Universal gas const. $\mu$=slip factor

$P_{01}$=Inlet total pressure $P_{02}$=Exit total pressure

The maximum impeller tip speed that can be achieved depends on the impeller design (solid or counter bored) and the disk material. A high impeller tip speed gives a compact design. Based on the recommendations of Eames [17], the tip speed was taken to be 1800 ft/s. A stress analysis is done to further ensure that the induced stresses in the impeller are below acceptable stress levels in the selected material. The impeller diameter is calculated using the following relationship:

$$D_2 = \frac{U_2}{\pi N} \tag{6.2}$$

| | Value(in.) | Value(cm.) |
|---|---|---|
| $D_{hub}$ | 0.71 | 1.8 |
| $D1_{mean}$ | 1.7 | 4.32 |
| $D_{eye}$ | 2.68 | 6.81 |
| $D_2$ | 3.4 | 7.87 |
| b | 0.85 | 2.16 |
| L | 1.18 | 3 |

**Table 6.3:** Impeller Dimensions

where, $D_2$ = Impeller diameter, $N$=Rotational speed, $U_2$=Impeller tip speed

The major dimensions of the impeller are presented in Table 6.3. The calculated specific speed for the impeller is 87 and the specific diameter is 1.34. This gives an efficiency of about 82% using the charts in Balje [18]. Assuming a blockage factor of 3%, the blade height can be calculated. A length correlation [20] is used to find the axial length of impeller. The meridional velocity component is assumed to remain constant. This gives an exit velocity triangle as shown in Fig. 6.9. The backward curved angle is 20°.

### 6.3.2 Vaneless Radial Diffuser.

The Mach numbers at the exit of the impeller are supersonic due to the high pressure ratio. The gas is slowed down in the vaneless space before entering the radial diffuser stage. This prevents shock formation and associated losses at the radial diffuser vanes. The dimensions of the vaneless space are found by using mass conservation equations. Fig. 6.10 shows the layout of the vaneless space and Table 6.4 shows the dimensions.

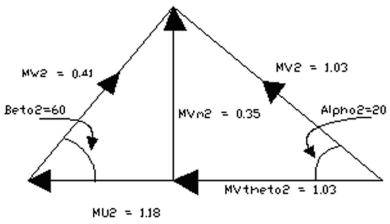


**Figure 6.9:** Exit Velocity Triangle

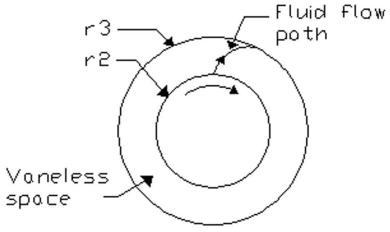


**Figure 6.10:** Vaneless Radial Diffuser

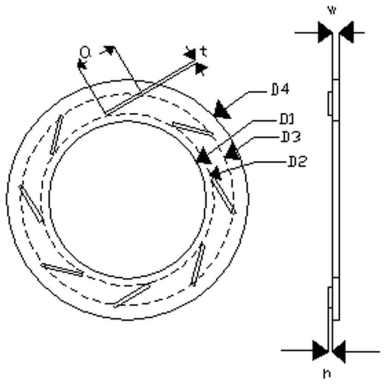


**Figure 6.11:** Radial Vaned Diffuser

**6.3.3 Vaned Radial Diffuser.** A vaned radial diffuser stage follows the vaneless space. There are several options for the vane geometry including airfoil sections, channels, low solidity vanes and ribs.

| | Value(in.) | Value(cm.) |
|---|---|---|
| $D_2$ | 3.4 | 8.64 |
| $D_3$ | 4.66 | 11.84 |

**Table 6.4:** Vaneless Diffuser Dimensions

The low solidity vaned diffusers give enhanced range, higher flow range and better efficiency with reduced manufacturing cost [21]. The design of the vanes consists of the calculation of the vane profile, spacing and number of vanes. The dimensions of the diffuser were calculated using a low solidity value of 0.7, number of vanes as 8 and a leading edge angle of 75°. Fig. 6.11 shows the layout of the vaned radial diffuser and Table 6.5 presents the major dimensions.

**6.3.4 Vaned Axial Diffuser.** The vaned axial diffuser reduces the swirl component of velocity of the gas entering the combustor and helps reduce pressure losses through the $90^0$ turn by keeping the flow attached.

**6.3.5 Rotor Dynamics.** Most rotating machinery have imbalances and these are due to uneven distribution of mass, shaft deflection, static eccentricities amplified by shaft rotation and shaft movement inside the bearing. Care should be taken to ensure that the engine operation does not excite resonant frequencies of the system caused by these imbalances. Campbell diagrams are used to determine resonant frequencies of the rotating components at various shaft speeds [22].

**6.3.6 Stress Analysis and Material Selection.** The two main considerations for impeller material selection are failure due to creep and failure due to disk burst at high centrifugal loading. Centrifugal stresses are extremely high for the design speed of 100,000 RPM. Creep stress is estimated assuming a stress factor of 0.2 for the radial impeller and estimating the maximum stress as the yield strength of the material adjusted for the

temperature rise in the impeller. Titanium and aluminum alloys were considered for the impeller material. The stress in the aluminum alloy is close to the maximum allowable for 0.1% creep while the stress in the titanium impeller is well below the maximum allowable value.

A simple radial stress calculation at the outermost radius of the impeller disk at the rated speed of 100,000 RPM results in a radial stress of 358 MPa using Aluminum 7075-T6 alloy and 615 MPa using a titanium alloy (Ti-6Al-4V). The yield strength of these materials are 538 MPa and 930 MPa respectively. A useful ratio to judge material capability under centrifugal loading is the breaking length, given by:

$$Breakinglength = \frac{UTS}{\rho g}$$

where UTS is the ultimate tensile strength of the material, ρ is the material density and g is due to centrifugal force.

| | Value(in.) | Value(cm.) |
|---|---|---|
| $D_1$ | 4.66 | 11.84 |
| $D_2$ | 5.13 | 13.03 |
| $D_3$ | 6.3 | 16 |
| $D_4$ | 7.14 | 18.14 |
| a | 1.22 | 3.1 |
| t | 0.1 | 0.254 |
| w | 0.2 | 0.51 |
| h | 0.13 | 0.33 |

**Table 6.5:** Vaned Diffuser Dimensions

The breaking length of Titanium alloys is greater than Aluminum alloys by about 67%. An impeller disk made of titanium satisfies the stress requirements of the impeller for creep and burst failure, and also has a higher strength to weight ratio. The superior material benefits outweigh the higher material cost. A coating may also be used on the impeller blades to improve erosion resistance for operation in adverse environments.

**6.3.7 Manufacturing Methods.** Traditionally, casting and five-axis milling have been the main manufacturing methods for centrifugal compressors. Titanium is difficult to machine because it absorbs little of the heat generated in the machining process leading to the thermal failure of the cutting head. A new machining process has been pioneered at Makino for CNC machining of titanium impellers for NASA's low cost turbopumps [23]. This allows for a considerable reduction in machining time. This process has also demonstrated excellent surface finish with high dimensional control giving very good agreement with the design gas path and low part to part variation. The improved impellers have demonstrated a longer life as well as very low structural imbalance.

## 6.4 Combustor Design

**6.4.1 Sizing of Combustion Chamber.** Fig. 6.12 shows the layout and major dimensions of the annular, reverse flow combustion chamber. The combustor can be divided into the primary and the dilution zones. The flame front is located in the primary zone where the fuel-air combustion occurs. The dilution zone adds air to the

| | Mach number | Q | Area ($cm^2$) |
|---|---|---|---|
| Combustion chamber | 0.01 | 0.6806 | 108 |
| Annular chamber | 0.1 | 6.9414 | 19.84 |

**Table 6.6:** Combustor Design Parameters

combustion products from the primary zone to reduce the temperature of the exhaust gases from about 2300 K in the primary zone to about 1250 K at the inlet of the radial turbine.

| | Value(in.) | Value(cm.) |
|---|---|---|
| $D_1$ | 6.45 | 16.38 |
| $D_2$ | 6.6 | 16.76 |
| $D_3$ | 8.06 | 20.47 |
| $D_4$ | 8.2 | 20.83 |
| L | 4.95 | 12.57 |
| L2 | 1.22 | 3.1 |
| L1 | 1.88 | 4.77 |

**Table 6.7:** Combustion Chamber Dimensions

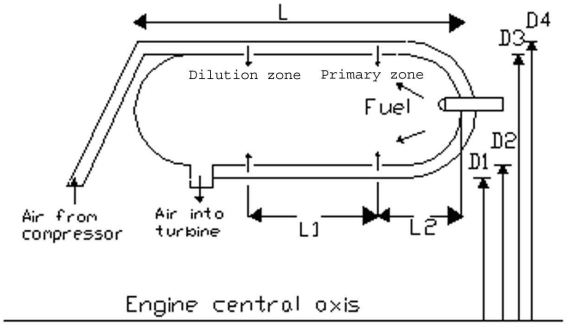


**Figure 6.12:** Combustor Layout

The sizing of the combustor was carried out using the design guidelines given by Fletcher [20]. The combustor is designed based on the maximum loading condition which occurs at the highest altitude and the coldest day. A range of combustor loading from 10 to 75 $kg/s - atm^{1.8}m^3$ was selected to ensure acceptable efficiency based on the design guidelines. The combustor volume is determined as the maximum value derived using the range of inputs for combustor loading.

The maximum combustor volume is obtained for the combustor loading of 10 $kg/s - atm^{1.8}m^3$ and this volume is selected for the design. This is the volume of the inner combustion chamber excluding the annular region. Combustor intensity is a measure of the rate of heat release per unit volume. The design guidelines [20] specify a maximum value of 60 $MW/m^3 - atm$. The calculated value of combustor intensity for the selected volume is 57 $MW/m^3 - atm$. Hence the design volume satisfies both criteria.

The design guidelines specify local Mach numbers and equivalence ratios in the different sections of the combustor. The equivalence ratio is taken to be 1.02 in the primary zone and 0.6 in the secondary/dilution zone. The equivalence ratio along with the stoichiometric fuel air ratio for the fuel gives the local fuel air ratio. This, along with the fuel flow rate from the engine cycle calculations, is used to determine the local air mass flow rate. The local Mach numbers are used to determine flow coefficient Q from which the area of the combustion chamber can be calculated [20]. The local temperature in the primary zone is assumed to be 2300 K which is close

to the adiabatic flame temperature for jet fuel. The local Mach numbers, Q values and areas of the chamber and the annulus are presented in Table 6.6.

Using an annulus Mach number of 0.1 gives a ratio of injector port to annulus Mach number of 3. This ratio is higher than 2.5 and it should result in a good coefficient of discharge. These results are used to compute the diameters of the combustor. The gas velocity in the combustor volume is calculated using the local Mach number. This determines the residence time which should be higher than 3 ms for conventional combustors. The residence time for this design is calculated as 14 ms which meets the design guidelines. The length of the combustor is determined from the combustor volume and the cross-sectional area of the burner. Table 6.7 gives the major dimensions for the combustion chamber.

### 6.4.2 Combustor Performance.

**Pressure drop**: The pressure drop from the exit of the compressor to the inlet of the turbine is one of the major concerns in combustor design. Aerodynamically, it can be regarded as a drag coefficient [24]. A pressure-loss factor, defined as the ratio of the total pressure drop across the combustor to the inlet total pressure is used to quantify the pressure drop. This term only represents the "cold" losses as it does not include the additional losses due to heat addition and entropy generation during combustion. The "cold" pressure loss in a typical annular combustor is around 6%.

**Combustion Efficiency**: Combustion efficiency is defined as the ratio of heat released in combustion to heat available in the fuel. It is usually computed using CFD calculations or is measured experimentally. Emissions regulations usually stipulate combustion efficiencies in excess of 99%. Experimental measurements have shown that combustion efficiency follows a predictable relationship using a "theta" factor. This factor relates to the engine operating condition and is a function of inlet temperature and pressure, the mass flow rate and combustor geometry. The exact relationship of the "theta" factor is determined experimentally.

**6.4.3 Fuel.** Gas turbine engines can operate with a variety of kerosene-type fuels. Different fuels have different properties affecting the ignition performance. Evaporation rate of the fuel is affected by the fuel volatility and fuel spray quality is affected by the fuel viscosity. The Pyros engine cycle was developed using Jet-A as the fuel. It can be run on other fuels including Jet A-1 and Jet-B which have only slight differences in properties from those of Jet-A.

**6.4.4 Materials and Coatings.** The primary consideration in selecting materials for the fuel injection system, the combustion liner and the transition piece is to achieve high temperature creep rupture strength. The materials also need to incorporate high corrosion and oxidation resistance. Silicon carbide and silicon nitride

ceramics satisfy these requirements. Based on cost estimates for the two materials, silicon carbide is chosen to construct the combustion liner[25]. A thermal barrier coating of stabilized zirconium prevents thermal wear.

## 6.5 Turbine Section Overview

The turbine section consists of the gas generator section high pressure turbine spinning at 100,000 RPM followed by the power generator section consisting of a power turbine mounted on an output shaft spinning at about 75,000 RPM.

**6.5.1 Radial Turbine Design.** The function of the radial turbine in the gas generator section is to provide power to the compressor. The way in which the gas flowing through the radial turbine produces this power is discussed through the use of velocity triangles (Fig. 6.13).

The gas enters the nozzle (stator) blades at an angle $\alpha_1$ with velocity $V_1$, expands and leaves with an increased velocity $V_2$ at an angle $\alpha_2$. The rotor blade inlet angle is chosen to suit the direction $\beta_2 = \chi_2$ of the gas velocity $W_1$ relative to the blade at inlet. After being deflected in the rotor impeller passages, the gas leaves with relative velocity $W_3$ at an angle $\beta_3$. The change of the tangential (or whirl) component of momentum per unit mass flow, which produces the useful torque, is represented by $Cw_2 + Cw_3$.

In the present design, the simplest possible scenario of gas flow is considered. It is assumed that the flow entering the impeller is completely radial (no axial component) and the flow exiting the impeller is completely axial (no radial component). It is also assumed that the flow impinging on the radial NGV (nozzle guide vanes or stators) is completely axial. Accordingly, $\beta_2 = \alpha_3 = 0$.

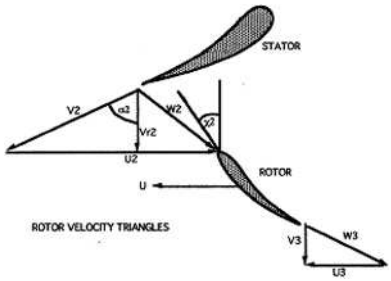


**Figure 6.13:** Radial Turbine Velocity Triangles[26]

The various relative and absolute flow velocities are then calculated using trigonometry and applying the continuity equation at the entry and exit of the impeller. The following are the design variables to be calculated:

1. Inlet and exit tip radii of the impeller: $R_{tip}$, $R_{exit}$
2. Exit hub radius of the impeller: $R_{hub}$
3. Inlet and exit radial distances of the stators from the shaft centerline: $R_{NGVinlet}$, $R_{NGVexit}$

The input variables for the calculations are:

1. Inlet and exit total temperature: (T4, T5) - 1250 (K), 1027.4(K)
2. Inlet and exit total pressure (P4, P5)- 545.89 (KPa), 203.21 (KPa)
3. Impeller mass flow - 0.5412 (kg/s)

4. Gas generator shaft speed - 100,000 (RPM)

Combining the above with velocities obtained from the velocity triangles as outlined, it is possible to obtain an estimate of the various parameters (design variables), which constitute the preliminary design space.

The steps needed to realize the preliminary design of the radial turbine along with all the guidelines and the charts in the design algorithm have been taken from Fletcher [20]. The following are the salient features of the algorithm:

1. The turbine isentropic efficiency is calculated from the inlet and exit total temperature and pressure
2. Specific speed ($N_s$) is calculated from isentropic efficiency and gas generator shaft speed
3. The impeller tip speed can then be calculated from the power extracted by the turbine

$$U_{tip}^2 = C_p(T_4 - T_5); R_{tip} = U_{tip}/\Omega$$

4. From chart [20], $R_{exit}/R_{tip} = 0.7 =>$ obtain $R_{exit}$; set $M_{exit} = 0.35 =>$ determine flow function $Q = \dot{m}\sqrt{T}/P(Kg/Kpa - s)$; where $\dot{m}$ is the engine mass flow (Kg/s), T is the turbine inlet total temperature (K), P is the turbine total inlet pressure (KPa) [20]
5. Determine impeller wheel area A => calculate $R_{hub}$
6. Set Nozzle Guide Vane exit angle from chart [20]
7. Set NGV exit radius ratio $R_{NGVexit}/R_{tip} = 1.1 =>$ obtain NGV exit radius, $R_{NGVexit}$
8. Set $R_{NGVexit}/R_{NGVinlet} = 1.45 =>$ obtain NGV entry radius, $R_{NGVinlet}$
9. Calculate axial length $L = 1.3(R_{tip} - (R_{exit} + R_{hub})/2)$
10. Draw velocity triangles at the entry and exit of the impeller
11. Calculate slip using the Wiesner formula $s = 1 - \sqrt{cos\beta_3}/N_b^{0.7}$, $N_b$ is the number of blades and $\beta_3$ is the impeller exit angle.

The procedure outlined above provides only a first order estimate of the various unknown parameters that make up the turbine design problem. However, obtaining the number of blades on the impeller requires the use of more sophisticated and time intensive computational techniques that minimizes frictional and boundary layer losses between the blades. In the present stage of the design, the parameters that cannot be obtained using the above algorithm have been estimated based on literature survey.

Accordingly, a 20-bladed impeller is considered which minimizes slip losses and hence maximizes work output. This results in the following design parameters:

- $R_{tipinlet} = 2.0611$ in, $R_{tipexit} = 1.4428$ in, $R_{hubexit} = 0.5340$ in, $NGVheight = 0.4534$ in, $R_{NGVexit} = 2.2672$

in, $R_{NGVinlet} = 3.2875$ in, $N_s = 0.7043$

- NGV exit angle = 72°
- Blade width at impeller tip 'b' = 0.344 in

In addition, the velocity components corresponding to the velocity triangles are:

- $\alpha_1 = \beta_1 = 0°$ (assuming radial entry into the NGV), $\alpha_2 = 72°$ (stator exit angle, according to the guidelines), $\beta_2 = 0°$ (assuming relative velocity to be completely radial at the impeller tip), $\alpha_3 = 0°$ (rotor exit angle, assuming flow to be completely axial at the rotor exit),
- $\beta_3 = 60.5°$ at the axial blade tip; $\beta_3 = 33.2°$at the axial blade hub; Slip $\sigma = 0.9$

### 6.5.2 Axial Turbine Design.

The axial power turbine provides power (torque) to the main rotor. The way in which the gas flowing through the axial turbine produces this power is discussed through the use of velocity triangles (Fig. 6.14). The gas enters the nozzle blades at an angle $\alpha_1$ with velocity $C_1$, expands and leaves with an increased velocity $C_2$ at an angle $\alpha_2$. The rotor blade inlet angle is chosen to suit the direction $\beta_2$ of the gas velocity $V_2$ relative to the blade at inlet. After being deflected in the rotor impeller passages, the gas leaves with relative velocity $V_3$ at angle $\beta_3$. The change of the tangential (or whirl) component of momentum per unit mass flow, which produces the useful torque, is represented by $Cw_2 + Cw_3$. The axial component will be assumed constant; $Ca_3 = Ca_2 = Ca$. Therefore, the annulus has a diverging cross-section area, to accommodate the decrease in density as the gas expands through the stage [27].

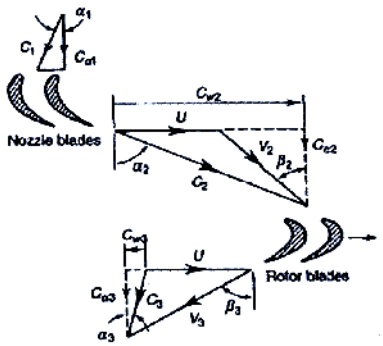


**Figure 6.14:** Axial Turbine Velocity Triangles [27]

The various relative and absolute flow velocities are calculated by trigonometry and applying the continuity equation at the entry and exit of the turbine.

In contrast to the radial turbine design, the axial turbine design is more straightforward, with a smaller design space. The design variables to be calculated are:

- Tip radius of the turbine blade (measured from the shaft centerline): $R_{tip}$
- Hub radius of the turbine blade (measured from the shaft centerline): $R_{hub}$
- Power turbine shaft speed: N

The input variables are:

- Inlet and exit total temperature - 203.21 (KPa), 89.33 (KPa)

- Inlet and exit total pressure -1027.4 (K), 867.583 (K)
- Turbine mass flow - 0.5124 (kg/s)

Combining the above with velocities obtained from the velocity triangles as outlined, it is possible to obtain an estimate of the various parameters (design variables), which together constitute the preliminary design space. Following are the steps needed to realize the preliminary design of the radial turbine. All the guidelines and the charts in the above algorithm have been taken from Fletcher [20]

1. Given the inlet and exit total temperature and pressure, the isentropic efficiency of the turbine can be calculated; set $M_{exit} = 0.5 =>$ determine Flow function $Q = \dot{m}\sqrt{T}/P(Kg/KPa - s)$; where $\dot{m}$ is the Engine mass flow (Kg/s), T is the turbine inlet total temperature (K), P is the turbine total inlet pressure (KPa)čiteFletcher01
2. Set $R_{hub}/R_{tip} = 0.71$
3. Determine impeller wheel area A => calculate $R_{tip}$, $R_{hub}$
4. Obtain power turbine shaft speed N, using $AN^2 = 50x10^6$ ($AN^2$ corresponds to the maximum stress that the turbine blades can withstand during operation.)
5. $U_{tip} = R_{tip}$N, $U_{hub} = R_{hub}$N, $U_{pitch} = R_{pitch}$N
6. Rotor tip exit swirl angle $= 5^\circ$
7. Stator exit angle $= 72^\circ$
8. Set Aspect Ratio $AR = 0.5$
9. Draw velocity triangles at the entry and the exit station of the turbine stator and rotor

The procedure outlined above, as noted, provides only a first order estimate of the various unknown parameters that make up the turbine design problem. However, calculating the number of blades that make up the axial turbine requires the use of more sophisticated and time intensive computational techniques that minimizes frictional and boundary layer losses between the blades. In the present stage of the design, the parameters that cannot be obtained using the above algorithm have been estimated based on literature survey. Accordingly, a 20-bladed turbine is considered that again minimizes slip losses and maximizes the work output of the turbine. This results in the following design parameters:

- $R_{tip} = 2.411$ in, $R_{hub} = 1.73$ in, $N = 75000$ RPM, $U_{tip} = 486.68$ m/s, Chord 'c' $= 0.23$ in,$U_{hub} = 348.87$ m/s, $U_{pitch} = 417.77$ m/s, $NGVexitangle = 72^\circ$ (according to guidelines listed above).

Also, the velocity components corresponding to the velocity triangles are:

- $\alpha_1 = \beta_1 = 0^\circ$ (assuming axial entry into the stator), $\alpha_2 = 87^\circ$ (stator exit angle),

- $\beta_2 = 53.4^\circ$ at the axial blade tip; $\beta_2 = 61.4^\circ$ at the axial blade hub
- $\alpha_3 = 5^\circ$(rotor exit angle, according to the guidelines listed above),
- $\beta_3 = 69.9^\circ$ at the axial blade tip; $\beta_3 = 66^\circ$ at the axial blade hub

**6.5.3 Inter-Turbine Duct.** The inter-turbine duct is required to pass the gas from the high pressure radial turbine to the low pressure axial free turbine. A scrolled inter-turbine duct typical of a single can is usually employed. The pressure loss that accompanies the flow through the duct needs to be minimized. The pressure losses due to duct geometry are usually accounted for by a loss coefficient, $\lambda$, given by[20], $\lambda = (1 - A_1/A_2)^2$ where, $A_1$ is the inlet area of the duct and $A_2$ is the exit area of the duct. $A_1, A_2$ can be obtained once the dimensions of the impeller and axial turbine are determined. Accordingly, we get, $\lambda = 0.13$. Finally, the length of the inter-turbine duct can be found by employing the 'swan neck duct parameter' (SNDP), given by $L = (D_{inlet} - D_{exit})SNDP$; $D_{inlet}$, $D_{exit}$ are the duct diameters at the entry and exit stations and can be found once the impeller and axial turbine dimensions are determined. Assuming $SNDP = 6$ for $A_2/A_1 = 1.57$, we get $L = 1.38$ in.

**6.5.4 Turbine Blade Materials.** Turbine blades experience extreme stress, temperature and corrosion conditions. To ensure long life and high performance in such environments, it is necessary for the turbine blades to have the following characteristics at high temperatures.

1. Limited creep ($< 1\%$)
2. High rupture, yield and fatigue strength
3. High corrosion resistance
4. Low coefficient of thermal expansion, to prevent the turbine blades from deforming out of shape
5. High thermal conductivity, to prevent development of thermal stresses within the blade
6. Good ductility
7. Thermal (structural) stability

These properties can be achieved through a judicious combination of a suitable blade material and an appropriate manufacturing process.

Traditionally, nickel based superalloys have been extensively used as turbine blade materials in aeroengines. They have good metallurgical stability and high specific strength at elevated temperature; they are more resistant to creep, and have better resistance to oxidation, carburization, and halogen attack than other superalloys.

| Base metal | Composition by weight% |
|---|---|
| Titanium | 1-3% |
| Aluminum | 1-3% |
| Chromium | 20 % |
| Nickel | Balance |

**Table 6.8:** Major Constituents of a Typical Nickel Based Superalloy

A typical nickel based superalloy would have the major constituents as shown in Table 6.8. Apart from these, small quantities of Cobalt, Manganese, Tungsten, Thallium and Molybdenum are also usually present in the superalloy. Each of these metals alters the properties of the superalloys in the following manner:

1. The addition of 3-5 % Titanium - Aluminum increases the γ' phase fraction in the superalloy, increasing elevated temperature strength and large creep deformation resistance.
2. The addition of 10-20 % Cr increases oxidation and corrosion resistance at high temperatures.

The high temperature properties of the nickel-based superalloys can be improved in the following ways:

1. The high temperature rupture strength of the superalloy can be increased by the creation of dislocation networks within the microstructure. These networks depend on and grow with γ' phase particles during creep, increasing the strength of the superalloy. Also, a large volume fraction ($> 0.6$) of the γ' phase with large particle size (r = 0.5 $\mu$m) increases thermal fatigue resistance at high temperatures.
2. The addition of dispersoid particles like Tungsten and $Y_2O_3$ increases high temperature rupture and fatigue strength of the superalloy. Also, they increase creep resistance by maintaining a fine dislocation network, which prevents the jog movement necessary for creep. Ashby deformation maps plotting areas of different creep mechanisms in the stress temperature plane for a MAR-M Ni-based superalloy show that the turbine blade material deforms rapidly with a grain size of 100 $\mu$m, but not with a grain size of 1 cm [28].
3. One of the most important ways of dramatically improving the superalloy properties is through the process of grain orientation and grain boundary control of the superalloy microstructure. The process of grain orientation, creating an octahedral slip system, results in the superalloy having higher strength than the cube slip system of the γ' phase. Concurrently, ductility can also be improved if weak transverse grain boundaries are removed, as in directional multi- or single-crystal hardware (direction solidification). Thermal fatigue resistance benefits from both the orientation and grain boundary changes. Grain boundary control can be achieved through the use of dispersoids, which creates large aspect ratio (L/D - length-to-diameter ratio) grains during processing and heat treatment. Grain orientation can be achieved through the process of directional solidification.

A recent study of materials for high temperature applications showed that a conventionally cast or wrought Ni- based superalloy can operate upto about 1400 K and costs among the lowest of all the selected alloys [28]. A cost based superalloy for use as turbine blade material at high temperatures would have the following constitutents:

- Nickel, for large specific strength at high temperatures

- Chromium for large high temperature corrosion resistance
- Aluminum, Titanium to form γ' precipitates for improved high temperature rupture strength, creep resistance and thermal fatigue strength
- Dispersoid particles - $Y_2O_3$/Tungsten - for improved high temperature rupture strength, thermal fatigue strength and creep resistance
- 5 % Fe to reduce cost (ferrochrome/industrial scrap in place of pure more expensive Chromium)

Additionally, the superalloy would not contain expensive elements like Cobalt, Molybdenum, Thallium, Niobium, Hafnium and Rhenium [29].

From the above, it is apparent that the proposed superalloy resembles Nimonic 80A superalloy most closely. The composition of Nimonic 80A is [30]: Ti - 2.5%, Al - 1.3 %, Ni- Balance

However, Nimonic 80 A can withstand a maximum of 1101 K (828°C) [30]. For the present application, the superalloy needs to withstand a temperature of 1250 K (977°C). In addition, Ni-based superalloys have very poor corrosion resistance to elements like salt water which are ingested in marine environments. Diffusion coatings using Pt-Al (Platinum- Aluminum) provide a cost effective way of minimizing corrosion due to contaminants, thus making the engine operation amenable to all environments and conditions.

Hence, the desired superalloy is a modified version of Nimonic 80 A, having the following constituents:

**Nimonic 80 A + Directionally Solidified microstructure +**
**Increased Al, Ti content (3 - 5 %)+$Y_2O_3$/Tungsten (1.5 - 5 %) + 5 % Fe**

This gives a predicted maximum temperature capability of about 1000 °C (1273 K), which is suitable for use in the present application. The turbine blade would consist of the base material (the Ni-based superalloy, described above) with a layer of Pt- Al coating on the substrate.

**6.5.5 Manufacturing Methods.** Nickel based superalloys have been manufactured through the process of casting, where the alloying additions are enough to lead to gross structural segregation and lack of homogeneity. The problems directly attributable to this segregation in ingots include cracking during forging and heat treatment, non-uniform strength and ductility and a wider scatter of mechanical properties from part to part.

Similar alloys when produced by powder metallurgy show a minimum of macro-segregation and thus improved hot workability. The development of an inert method of production, collection and densification of prealloyed powders has resulted in improvements in both creep strength and ductility [30]. Moreover, the development of dispersion-strengthened metal alloys, which retain useful long-term mechanical properties up to temperatures close to their melting points, is possible using the powder metallurgy process. These cannot be manufactured using the conventional casting process.

**Powder Production And Processing Techniques**

The powder metallurgy approach is based on a few principles: powder production and processing in inert gas atmospheres, densification via hot consolidation techniques and the achievement of desired mechanical properties via thermo-mechanical processing.

- Inert gas atomization - This technique results in the creation of relatively coarse Nickel, Chromium powders which form the substrate.
- Mechanical alloying - This is the process of addition of highly reactive Aluminum, Titanium powders to the substrate (Ni/ Cr powder), which introduces the γ' phase in the superalloy. This results in the formation of precipitation-hardened powders, which can exhibit useful strengths upto intermediate temperatures ($\sim$800°C/1173 K). Additionally, the mechanical alloying process allows the production of dispersion-strengthened powders, hence combining both γ' precipitation hardening at low and intermediate temperatures and use of $Y_2O_3$ dispersion strengthening for elevated temperature service. However, the resultant powder is highly porous, and hence there is a need to decrease the porosity (and hence, increase density) of the mixture. This is accomplished through the process of densification, which results in achievement of 99-100% of theoretical density.
- Densification - Forging is a technique which enables the production of large shaped bodies having very low porosity. The advantages of this technique are:
    1. Superior mechanical properties resulting from metal flow and the development of preferred crystallographic texture
    2. Low material losses, since component can be produced which is closer to the final shape.
- Thermo-mechanical processing- The mechanical properties of superalloys are determined not only by the chemical composition of the alloy but also by heat treatment. Thermo-mechanical processing is the deliberate manipulation of mechanical working and heat treatment to obtain the desired microstructure and mechanical properties. Usually, after forging, a high-temperature heat treatment for grain growth and a final aging treatment is necessary to restore original creep properties.

Powder metallurgy materials have an inherently fine grain size which is advantageous for creep strength, tensile strength, ductility and fatigue strength at intermediate temperatures. However, coarse grained Ni-based superalloys need to be produced for use at high temperatures. As noted, powder metallurgy allows for this through the process of dispersion strengthening- which allows for increased tensile, fatigue and creep strength at high temperatures- and precipitation hardening, which allows for increased strength at intermediate temperatures.

Hence, powder metallurgy is recommended as a suitable manufacturing method for producing high strength Ni-based superalloys for use as turbine blade materials.

## 6.6 Foil Air Bearings

The DN value (diameter of gas generator shaft in mm x rotating speed in RPM) for the present turbine is 2.7 million with the shaft rotating at 100,000 RPM. Conventional rolling element bearings are being currently designed for DN values going beyond 2.7 million, with 4.5 million considered the maximum possible value from a design standpoint [31]. This constraint is primarily due to the need to keep the rolling surfaces well lubricated to lessen the heat generated by frictional forces at such speeds.

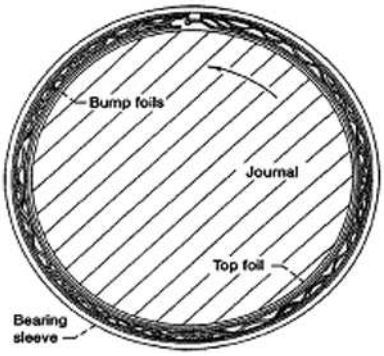


**Figure 6.15:** Foil Air Bearing [32]

The use of oil lubricants presents an obstacle to their use at high operating pressures and temperatures. While oil is a good medium as a coolant, it can tolerate local temperatures only up to 204 to 232 °C (400 to 450 °F). In addition, oil lubricated ball and roller bearings suffer from the effects of centrifugal loading at high speeds (DN values), which imposes limits on shaft diameter (and hence stiffness) and shaft speed [31]. Finally, oil requires a bulky support system such as scavenging, sealing, buffering, etc. In addition to adding significant weight, cost and maintenance chores, the support system interrupts the flow path and penalizes engine performance.

Foil Air Bearings are a suitable alternative to rolling element bearings. They are non contact, hydrodynamic, self acting fluid film bearings which use air as their working fluid or lubricant and require no external pressurization, dispensing away with the need for oil and the associated lubrication, pump and cooling system. The compliant characteristics (arising from several layers of sheet metal foils) accommodate misalignment and distortion and allow for micro-sliding between foil layers which gives the bearing coulomb damping. When coupled with new high temperature solid lubricant coatings (PS304) for startup and shutdown wear protection, these bearings are capable of operating over 650° C (923 K). Also, foil air bearings have load bearing capacities that increase linearly with speed. The latest generation of foil air bearings have respectable load bearing capacities at high speeds. In contrast, rolling element bearings have load capacities that do not vary with speeds and are very low at high speeds [31]. Hence, this latest generation of foil air bearings is ideal for small turboshaft engine applications which have very high shaft rotational speeds. These positive attributes have led to many commercial applications benefiting from high reliability, low cost, low friction, and long life performance.

In 1999, advanced foil bearings together with new NASA developed high temperature coatings and modeling was used to successfully demonstrate the world's first Oil-Free turbocharger which operated at 95,000 RPM at

temperatures to 650° C (923 K) and produced 150 hp. This experience, coupled with further advances in bearings and high temperature solid lubricants enabled Oil-Free technology to be used in gas turbine engines [31].

Currently, efforts are being made to demonstrate that foil air bearings can provide adequate rotor support, stability and durability necessary for small turboshaft engines [33]. MiTi (Mohawk Innovative Technology Inc.) has developed foil bearings ranging from 6 mm to 150 mm in diameter having large load capacities, which can be operated upto 650° C (923 K), hence making them suitable for use in gas turbines. Owing to the lack of sufficient data (maximum steady state loads in both the radial and axial directions) at this preliminary design stage, the design of foil air bearings is very difficult. However, knowing the shaft diameter of the engine ( 27mm), foil bearings can be selected off the MiTi catalog list for use in our engine [34].

The loads acting on the gas generator shaft are dominated largely by the radial loads. The thrust loads in small engines are usually one order lower than the radial loads. Hence, two foil air journal bearings (for supporting radial loads) and one foil air thrust bearing (for supporting axial loads) are used for supporting the gas generator shaft. Also, one foil air journal bearing and one foil air thrust bearing are used to support the free turbine shaft, which spins at a lower speed of about 75,000 RPM.

Foil air bearings are placed away from the engine 'hot section', which eliminates the need for compressor air bleed (for bearing housing cooling purposes), thus helping improve engine efficiency. The bearings are located at the engine inlet section (leading to the compressor inlet) on the gas generator shaft, and beyond the exhaust duct on the power turbine shaft. The engine foldout provides locations of the bearings.

The use of foil air bearings results in an 'Oil-free' engine, with reduced weight and maintenance compared to a conventional engine. Since regular oil maintenance checks constitute a large part of overall engine maintenance, the potential payoffs of using an 'Oil-free' engine to direct operating costs (DOC) are large.

## 6.7 Accessories

**6.7.1 Fuel System.** The reverse flow combustor design permits an easy installation for the fuel injectors. The reverse flow design usually requires a large number of injectors in order to have a uniform temperature distribution at the combustor exit. The Pyros has 6 simplex type fuel nozzles. The nozzles are supplied with fuel using a circular distribution tube. The fuel is supplied to the tube by the fuel pumps controlled by the fuel control section of the FADEC. The geared fuel pumps are driven through the accessory gearbox. A separate pump drives fuel from the fuel tank to the fuel control section. A shut-off valve is installed in the line between the fuel tank and the fuel control section. This is connected by wires to a shut-off lever in the cockpit of the *Penguin*. The fuel control system is a fully electronic device that controls the fuel flow rate into the nozzles depending on engine

operating conditions and the commands from the FADEC. Fuel filters are installed in the fuel lines at different points. The fuel pump - fuel line connections are frangible satisfying FAR 27 specifications.

**6.7.2 Ignition System.** The Pyros has a capacitance type ignition system. It consists of an exciter, an ignition lead and the igniter plug. The exciter pulls input current from the engine electrical system, steps up the voltage and delivers a high voltage signal through the ignition lead to the igniter. Smaller engines usually use systems producing high frequency, low energy sparks while bigger engines use low frequency, high energy sparks. The Pyros has a low-voltage AC input ignition system which is favored due its longer life. For redundancy, two igniter plugs are located on the combustion chamber. They are the annular-gap type and are recessed into the combustor casing allowing them to operate at lower temperatures. The spark spreads out in an arc over the tip of the igniter. This ignites the fuel nozzles closest to the igniter and the combustion spreads quickly to the other nozzles.

**6.7.3 Starting System.** The starting system fulfills two primary functions:

- Rotate the gas generator until it reaches its self-sustaining speed.
- Purge the gas generator and the exhaust duct of any volatile gases prior to ignition.

A combined starter-generator device is selected to reduce part count and weight of the engine. The starter motor drives the gas generator until the engine attains a self-sustaining speed. After engine start it functions as an alternator and supplies electrical power.

The specifications of the starter system are set by the peak torque it needs to produce which is the torque required to overcome the drag torque of the gas generator at the maximum gas generator speed. This is another advantage of using a free turbine in that a lower power starter motor can be used as it does not have to generate torque to overcome friction and drag in the rotor system.

The starting sequence is as follows:

- The starter motor turns the gas generator shaft by producing enough torque to overcome the gas generator load.
- At 15% of idle speed, the fuel system starts fuel flow to the nozzles. Idle speed is usually defined as 40% of engine speed (for the Pyros, idle speed is 40,000 RPM). The ignition system is energized and combustion is initiated. The starter motor continues to supply some amount of torque to assist in the engine acceleration.
- The engine becomes self-sustaining at 50% of idle speed. Beyond this point it accelerates to 100% of idle speed without the help of the starter motor. AT 100% speed the starter switches to the alternator mode of operation.

**6.7.4 Control System.** The Pyros has a full authority digital engine control system (FADEC). The FADEC regulates the engine operation in order to supply the required amount of power without allowing any of the components to operate in a potentially damaging mode. Fig. 6.16 shows a simple control flow diagram of the FADEC. The power turbine shaft is connected to the engine gearbox through an over-running clutch. The clutch allows one way transmission of power from the power turbine to the transmission box. When the speed of the transmission gears exceeds the power turbine speed, the clutch is disengaged, preventing the rotor from driving the engine. On the other hand, increased rotor load decays the transmission speed resulting in a reduced power turbine speed. Speed sensors are mounted on the power turbine and gas generator shafts whose output signals are fed to a summing junction which combines these signals along with pilot inputs and other reference speeds to generate an output speed error signal. The error signal computes a command signal to regulate fuel flow rate which is fed to the fuel control section. The fuel control section uses this signal to generate an input signal for the fuel pumps. This is an iterative process, where the fuel flow rate is altered till the engine produces the exact amount of power to drive the rotor at the rated speed.

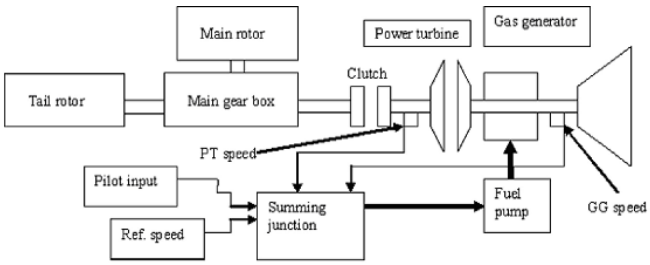


**Figure 6.16:** Control Schematic of Engine FADEC

## 6.8 Engine Summary

**6.8.1 Engine Weight and Dimensions.** The engine weighs 132 lbs. This is a first order estimate, arrived at by estimating the volume of the various components and looking up the densities of the materials making up the various components from the Materals Data Handbook [25]. The weight of the Pyros is lower than corresponding engines in the same class due to elimination of the lubrication system.

The total length of engine is 21.44 in. The largest outer diameter of the engine is 11.57 in. These dimensions have been displayed in the foldout.

**6.8.2 Engine Assembly and Disassembly.** The Pyros is easy to assemble/disassemble,with the gas generator section being bolted to the power turbine section at just one location. This allows for the 'hot section' to be separated from the 'cold section' completely, making for easy inspection and maintenance.

**6.8.3 Engine Design Characteristics - A Comparison.**

| Engine | Man. | Power (hp) | Airflow (lb/s) | SFC (lb/hp/hr) | GG RPM | Power/Wt. (hp/lb) | T.I.T (deg K) | C.R |
|---|---|---|---|---|---|---|---|---|
| T41 | Solar | 50 | 2.5 | 2.3 | 40,000 | 0.53 | 950 | 2.63 |
| JFS-100 | Garrett/ Allied Signal | 90 | 1.6 | 1.3 | 73,000 | 1.07 | 1283 | 3.5 |
| A-381 | Chrysler | 130 | 2.2 | 0.5 | 46,000 | 0.3 | 1200 | 4 |
| 502-6 | Boeing | 160 | 3.5 | 1.5 | 36,500 | 0.8 | 950 | 3.5 |
| T62T-32 | Solar | 160 | 2.2 | 1.4 | 61,091 | 1.12 | 910 | 3.5 |
| Pyros | UMD | 165 | 0.66 | 0.61 | 100,000 | 1.25 | 1250 | 7 |
| C250 | Rolls-Royce | 317 | 3 | 0.7 | 51,000 | 2.2 | 1283 | 6.2 |

**Table 6.9:** Engine Comparison

A baseline comparison of the Pyros was made with other gas turbine engines in its class. Table 6.9 has details of other existing engines and their design point features [35]. All values are compared at sea level and ISA conditions. The sfc of the Pyros is among the lower than only the Chrysler engine,which achieves a better SFC only by using a heavy regenerative cycle which lowers the power to weight ratio. The Pyros achieves a 50% reduction in sfc and a 25% increase in power to weight ratio among engines of the same hp rating (Boeing and Solar engines). This is achieved by using a higher turbine inlet temperature, compression ratio and operating speed. These improvements are a direct result of using superior materials in the engine construction (Titanium alloy in the compressor, Ceramics in the combustor and Ni-based superalloys in the turbines) as well as lightweight high-speed foil bearings. The table highlights the fact that smaller legacy engines (items 1-5 in the table) could not match the performance of the larger state-of-the-art Rolls-Royce C250 engine due to existent limitations on materials and bearing technologies. This could be done only with a drastic increase in engine cost. The Pyros bridges this gap by introducing low-cost, modern high-performance technologies to provide comparable performance to that of a larger engine.

# 7 Drive System

## 7.1 Design Criteria

One major differences between helicopters with piston engines and turbine engines is that the transmission is significantly heavier and costlier in the turbine helicopter. This is because greater reduction is needed due to the higher speed of the engine's output shaft. In many cases, turbine engines incorporate a nose gearbox to reduce the rotational speed of the engine output shaft. The Pyros does not have a nose gearbox. Therefore, this reduction must be taken care of in the drive system.

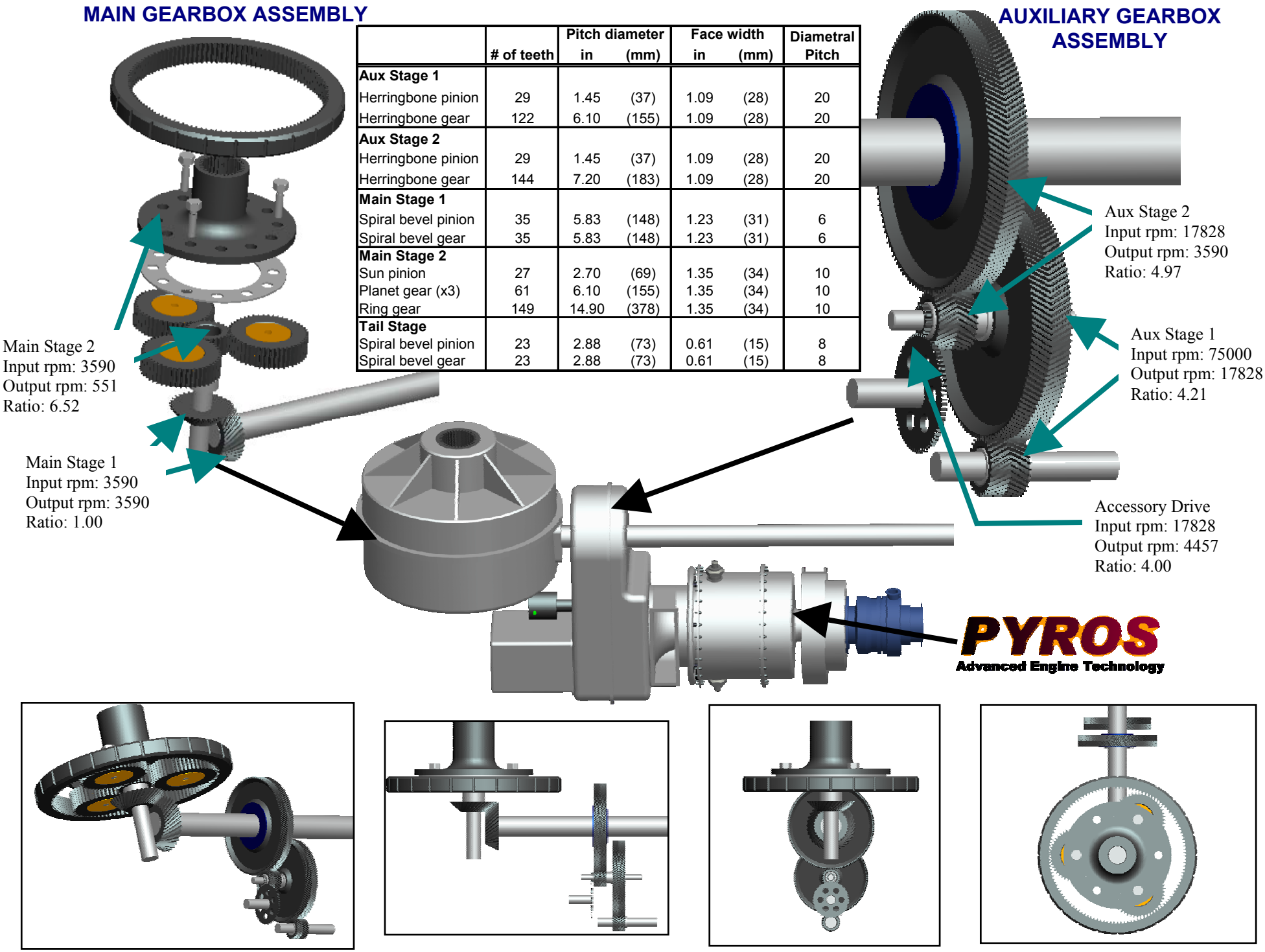


| | # of teeth | Pitch diameter in | (mm) | Face width in | (mm) | Diametral Pitch |
|---|---|---|---|---|---|---|
| **Aux Stage 1** | | | | | | |
| Herringbone pinion | 29 | 1.45 | (37) | 1.09 | (28) | 20 |
| Herringbone gear | 122 | 6.10 | (155) | 1.09 | (28) | 20 |
| **Aux Stage 2** | | | | | | |
| Herringbone pinion | 29 | 1.45 | (37) | 1.09 | (28) | 20 |
| Herringbone gear | 144 | 7.20 | (183) | 1.09 | (28) | 20 |
| **Main Stage 1** | | | | | | |
| Spiral bevel pinion | 35 | 5.83 | (148) | 1.23 | (31) | 6 |
| Spiral bevel gear | 35 | 5.83 | (148) | 1.23 | (31) | 6 |
| **Main Stage 2** | | | | | | |
| Sun pinion | 27 | 2.70 | (69) | 1.35 | (34) | 10 |
| Planet gear (x3) | 61 | 6.10 | (155) | 1.35 | (34) | 10 |
| Ring gear | 149 | 14.90 | (378) | 1.35 | (34) | 10 |
| **Tail Stage** | | | | | | |
| Spiral bevel pinion | 23 | 2.88 | (73) | 0.61 | (15) | 8 |
| Spiral bevel gear | 23 | 2.88 | (73) | 0.61 | (15) | 8 |



**Figure 7.1: Transmission System Layout**

Table 7.1 shows the parameters that the drive system must satisfy. The design objective is to fulfill these requirements while minimizing the weight, minimizing the number of stages, keeping the design compact and controlling the cost.

| | |
|---|---|
| Continuous Power | 150 HP (112 kW) |
| Engine Output Shaft Speed | 75000 RPM |
| Main Rotor Shaft Speed | 550 RPM |
| Tail Rotor Shaft Speed | 3592 RPM |

**Table 7.1:** Drive System Design Parameters

## 7.2 Drive System Configuration

Several drive system layouts were considered. One layout included the use of NASA's compound planetary gear bearing (Figure 7.2). This seemed to be a promising solution because it offered a reduction in part count, lighter weight and the option of using lower grade steel. However, using it in our single engine configuration introduced an additional stage that was needed to provide clearance for the tail rotor drive shaft over the engine. This additional stage not only negated the potential weight savings of the NASA's technology, but also imposed more assembly constraints.

The Penguin's drive system starts with an auxiliary gearbox that gives a 21:1 reduction before the power is transmitted into the main gearbox. This gearbox connects to the engine via a special coupling to allow for small axial, radial and angular misalignments. The auxiliary gearbox consists of a two-stage helical arrangement (Fig. 7.1). The advantages of using an auxiliary gearbox is that it provides clearance for the tail rotor drive shaft over the engine and it reduces the pitch line velocity of the bevel gear set in the main gearbox, which helps prevent scoring. Herringbone gears are the gears of choice for this stage. Unlike single-helix gears, herringbone gears produce equal and opposite thrust, which eliminates the need for thrust bearings.

**Figure 7.2:** NASA's Gear Bearing

After the auxiliary gearbox, the power flows through the main gearbox. A sprag clutch is located on the output shaft of the auxiliary gearbox in order to disconnect the rotors from the auxiliary gearbox and the engine in case of autorotation. The clutch is located here because it is unnecessary to drive the auxiliary gearbox when the clutch is disengaged. The main gearbox includes a spiral bevel gear set, a planetary gear set and a gear to drive the oil pump. After several studies, it has been found that it is optimal to achieve full reduction - 6.5:1 - from the planetary gear set and have the bevel set only for changing direction. The drive system layout is shown in Figure 7.1

The gears are made from case-carburized, AISI 9310 steel. The gears are hobbed and then lapped to provide the appropriate surface finish. Undercutting is avoided by choosing the appropriate face width to pitch diameter ratio, which are recommended by Dudley [36]. In addition, the pinions in stages 1 and 2 of the auxiliary gear box

are identical, which reduces the part number count in the drive system. This trades manufacturing cost for weight. The weight penalty is 2 lb (0.91 kg).

## 7.3 Gear Sizing

Bending and Hertz stresses are calculated to determine the size of the gears used in this application. The formulas for these stresses are simplified versions of AGMA formulas for the rating of gears [36]. The bending and Hertz stresses are calculated by the following equations:

| | |
|---|---|
| $s_t = K_t U_t K_d$ | $s_c = C_k \sqrt{K C_d}$ |
| $s_t$ = bending stress | $s_c$ = Hertz stress |
| $K_t$ = geometry factor for bending strength | $C_k$ = geometry factor for durability |
| $U_l$ = unit load, index for tooth breakage | K = K factor, index for pitting |
| $K_d$ = overall derating for bending strength | $C_d$ = overall derating for durability |

The allowable bending and hertz stresses are chosen from an S-N curve in order to give each gear a life of 4000 hours with a 25% margin of safety.

In addition to stresses constraining the gear sizes, manufacturing constraints are also a factor in the sizing of the gears. In order to avoid building new tooling and adding manufacturing costs, standard diametral pitches are selected. Doing this also gives an additional margin of safety since the gears are manufactured to the next available diametral pitch. A table of gear sizes is shown in Figure 7.1.

## 7.4 Weight Estimation

The weight of the gearbox is estimated using a technique developed by Schmidt [37]. This method allows calculation of the drive system weight from the size of the job that it has to do, how the arrangement is supported and some special features. The equation for determining the gearbox weight is: $W = 150\left(\frac{QPUAB}{S_a N}\right)^{0.8}$
The factors U, A, and B are selected from tables provided by Schmidt. P is the transmitted power and N is the pinion rpm. The terms Sa and Q are the average Hertz index and the non dimensional weight factor respectively and are defined as follows:

For spur and helical: $S_a = (800 + K)/2000$

For bevel: $S_a = (670 + K)/2000$ $Q = Ratio + Ratio^{-1} + 1$

For planetary sets:

$$Q = Ratio\left(\frac{0.4}{num.of\,planets} + 0.25\right) + \left(\frac{1.4}{num.of\,planets\,(Ratio - 2)}\right) - 0.25 \tag{7.1}$$

This method also provides means for estimating the weight of the required lubrication and the main rotor shaft. The derived weight of the drive system is 122.3 lb (55.6 kg). The weight contribution of each subassembly to the overall weight is shown in Table 7.2.

| **Subassembly** | **lb** | **(kg)** |
|---|---|---|
| Aux gearbox weight | 18.9 | (8.6) |
| Main gearbox weight | 64.3 | (29.2) |
| 90° (TR) gearbox weight | 8.0 | (3.6) |
| **Dry weight** | **91.1** | **(41.4)** |
| Lubrication | 18.3 | (8.3) |
| **Serviced weight** | **109.4** | **(49.7)** |

**Table 7.2:** Subassembly Weights

| | **Main** | | **Auxiliary** | | 90° | |
|---|---|---|---|---|---|---|
| **Component** | **lb** | **(kg)** | **lb** | **(kg)** | **lb** | **(kg)** |
| Gears & Shafts | 18.5 | (8.4) | 6.3 | (2.9) | 2.7 | (1.2) |
| Main Rotor Shaft | 8.7 | (4.0) | — | — | — | — |
| Housings | 9.8 | (4.5) | 3.3 | (1.5) | 1.4 | (0.6) |
| Bearings | 8.0 | (3.6) | 2.7 | (1.2) | 1.2 | (0.5) |
| Lube | 6.9 | (3.1) | 2.3 | (1.1) | 1.0 | (0.4) |
| Other | 12.3 | (5.6) | 4.2 | (1.9) | 1.8 | (0.8) |
| **Total** | **64.3** | **(29.2)** | **18.9** | **(8.6)** | **8.0** | **(3.6)** |

**Table 7.3:** Component Weights

According to Burroughs[38], the main gearbox weight is distributed as 25% gears, 25% housing, 10% bearings, 14% rotor shaft, 8% lubrication, and 18% for everything else. This distribution is used as a guide to get the component weight contribution of entire drive system (Table 7.3). It is assumed that the weight estimation method by Schmidt uses conventional materials for each component. Using a magnesium-zirconium alloy in place of the conventional aluminum alloy for the casings reduces the weight of the drive system by approximately 12.9 lb (5.9 kg). This brings the final estimated weight to 109.4 lb (49.7 kg).

## 7.5 Tail Rotor Drive and Gearbox

There is a bearing and coupling approximately midway down the tail rotor drive shaft in order to account for shaft misalignments due to bending of the tail boom and assembly. A KAflex coupling is used to eliminate the requirement for lubrication and to minimize maintenance . The bearings and couplings along the tail rotor drive shaft are repaired or replaced on condition. Reduction is not needed for the tail rotor drive. A spiral bevel gear set is used to make the final 90° turn to the tail rotor.

## 7.6 Lubrication, Filtering, Heat Removal and Sensors

The main gearbox will be pressure lubricated while the tail gearbox is splash lubricated. The oil passageways will allow lubrication of all bearings and will spray oil at the mesh of the gears to prevent metal-to-metal contact. The efficiency of the main gearbox is assumed to be 97% based on the configuration. About 4.5 HP is lost and is expended as heat to the system. Since the drive system is in a low power application, natural convection is sufficient to cool the oil, which eliminates the need for a heat exchanger.

A magnetic particulate trap (MPT) and filter are used to remove debris and foreign objects from the oil path.

If the MPT is clogged and no longer removes particles, a bypass valve opens in order to allow the oil to continue flowing through the system. Various embedded sensors provide information to the HUMS (Ch. 8) such as oil temperature, oil pressure. Accelerometers mounted onto the bearings and casings provide vibration data.

## 7.7 Summary

The Penguins drive system achieves the demanding 136:1 reduction while remaining lightweight and compact. It is also a robust system, having a 4000 hour MTBF. The modular design of this drive system allows for quick, easy removal of individual components during overhaul, thus reducing the MTTR. Also, HUMS is integrated into the system in order to detect and prevent catastrophic failure.

# 8 Health and Usage Monitoring System

Health and usage monitoring system (HUMS) has been shown to substantially reduce direct operating cost (DOC) in the long run [39]. Therefore, in order to reduce the maintenance cost, and improve reliability and safety of the Penguin, HUMS has been incorporated in its design. While a full state-of-the-art HUMS would significantly add to the cost of penguin, a basic HUMS has been designed so as to help keep the acquisition cost low, but at the same time, provide important health information of different systems. Transmission, engine, rotor system and other miscellaneous subsystems have been designed with embedded sensors for HUMS, so that an independent certification procedure for these is not required later, when HUMS is enabled. To further reduce the cost, complexity and certification issues, most of the data is stored in raw format with minimal onboard processing. This is achievable with readily available inexpensive flash memory. The data acquisition, processing, and data recording systems for HUMS is shared with the flight data recorder (FDR) system, and it can also be interfaced with the Smart Display or MFDs, when installed.

## 8.1 Sensors for HUMS

Sensors in the transmission provide oil particulate content from the magnetic particulate trap (MPT), and vibration data from accelerometers. Besides sharing information with the FADEC sensors, the Pyros has embedded accelerometers to provide bearing vibration levels. Rotor system incorporates MEMS accelerometers for monitoring the condition of hub and pitch links. Various subsystems, like, electrical system, avionics, and landing gear are other possible candidates for inclusion in the HUMS monitoring list.

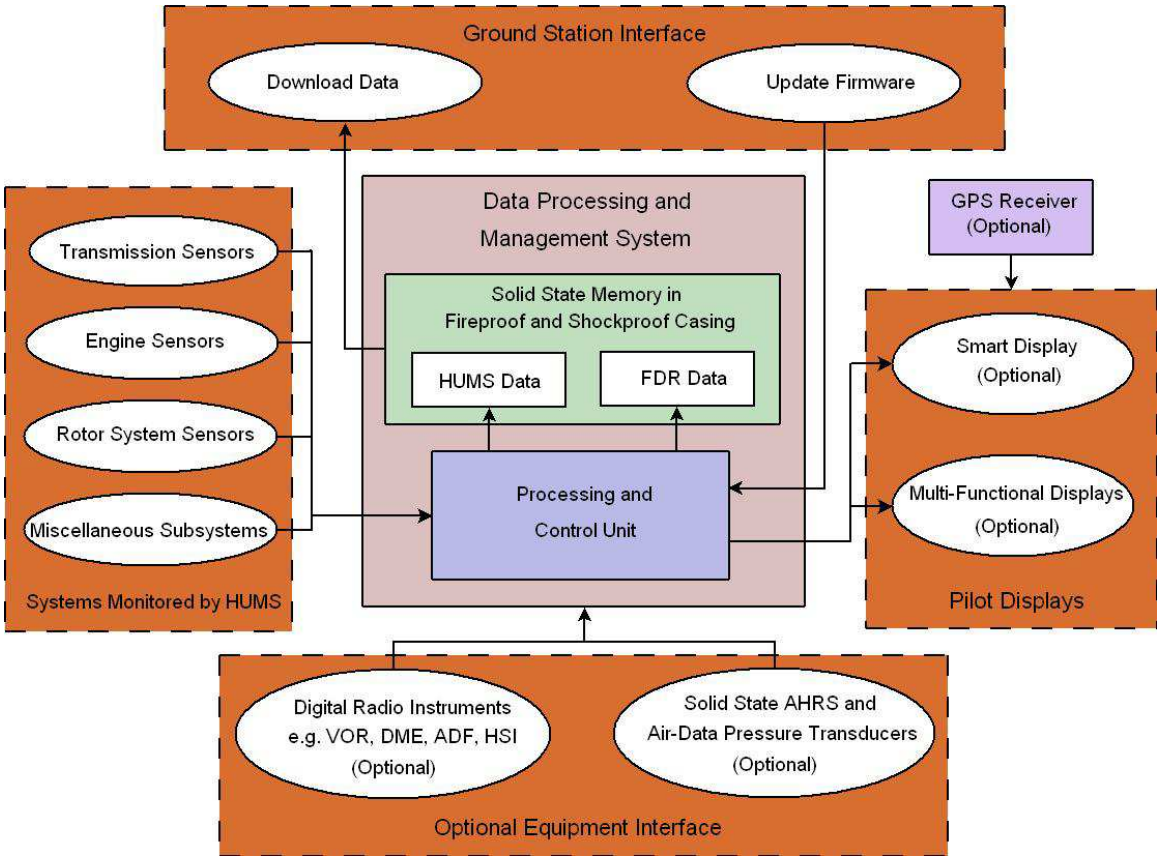


**Figure 8.1:** Data Processing and Management System with its Interfaces

## 8.2 Data Processing and Management System

The data acquisition and processing system is designed around the ARM7 class of RISC microprocessors to provide sufficient computing power at low cost and low power consumption. The data is stored in a bank of solid-state non-volatile flash memory. This modular unit (Figure 8.1) has ports for interfacing various sensors, display units (if installed), upgrading firmware, and downloading data from memory. It is housed in a fireproof and shockproof casing. Once the Penguin is on ground, this unit can be removed and connected to the ground station to allow data download, and firmware upload. The recorded parameters, and recording bandwidth can be re-programmed, as desired.

## 8.3 Vibratory Database

The key to exploiting the full potential of HUMS is the vibratory database (dBV). The manufacturer maintains the dBV, and based on its analysis, the operators are provided with necessary maintenance actions. The vibratory database will be initialized during the development, testing and FAA certification of each of the salient systems. Penguin's HUMS data will later be downloaded at selected time intervals, for example 50 hours, and will

be electronically transmitted to the manufacturer's database. This database will be supplemented by teardown inspections. As experience and supporting data are gathered, HUMS can be fine-tuned.

# 9 Airframe Structural Design

## 9.1 Structural Sections

The structure (Foldout 2) of the Penguin has been designed according to FAR27, subpart C. The maneuvering load is assumed to be a maximum of +2.0g and -0.5g and the probability of exceeding these limits is extremely remote[40]. The penguin consists of three major structural sections, which can all be seen in (Foldout 2). The first, the cockpit, is separated from the other sections by the rear fireproof composite wall. This wall acts as a firewall for the occupants and as a bulkhead for the outer skin of the aircraft. The composites for this wall are made using fireproof resin such as FyreRoc made by Goodrich[41]. The cockpit frame is made of 3/4" aluminum box tube. It holds the shape of the cabin and protects the occupants in case of a crash. The aluminum frame runs around the windshield, the nose cone, and forms the door frames. The door hinges are on the front of the door frame. The helicopter can be piloted without doors and the doors can be removed by pulling single pin from the hinge and unlatching the latch. The top section of the cockpit frame extends over the doors, through the firewall and is pin attached to the main rotor gearbox with two struts.

The windows of the aircraft are single curvature transparent acrylic. A film coating has been added that reduces infrared and ultraviolet light from entering the cockpit. Complex window curvature was avoided to save cost. Most of the skin of the aircraft is formed and riveted aluminum sheet where severe complex curvature could be avoided. Since it would be expensive to form aluminum for the nose and also to save weight, composites are used for the nose and tail cones. Both are made of fiberglass and Kevlar composites sandwiched and molded around a 1/8" Rohacell core. The weight of the pilots is distributed by a carbon and Kevlar composite floor which is a sandwich of composite and 1/2" Nomex honeycomb. The carbon allows for high strength and stiffness, while the Kevlar will absorb energy in a crash and prevent splintering. Beneath the floor are two aluminum rail "L" brackets which carry the floor loads to the structural members directly beneath the seats. Those structural members carry in compression the weight of the cockpit to the front landing gear brackets. While on the ground, this ensures that the second structural section, the airframe truss, is required to hold a minimal amount of force in compression.

While the helicopter is on the ground, the airframe truss supports in compression the weight of the main rotor, main rotor gearbox, engine, and part of the tail boom. The load on the upper members of the truss is minimized by angling the triangles on an axis that passes through the hub, where the all the flight loads originate. This

is somewhat similar to Bell's "focused pylon" design for transmission mounting. The truss is designed by the laws of statics and vector mechanics to be structurally constrained and, in this case, there are multiple redundant members[42]. The structure is all aluminum and is welded together in a single jig with pin attachments at the ends that attach to the landing gear brackets and the main gearbox. Since the surface of aluminum oxidizes quickly and that oxide layer requires over twice the temperature of the base material in order to melt, proper preparation is crucial prior to welding. Aluminum also dissipates the heat from welding very quickly, so it must be done "hot and fast"[43]. As long as proper precautions and techniques are utilized, the welds can be very robust. While in flight, the majority of loads come through the upper truss in tension and are transferred to the reinforced ring located just outside the planetary gearset of the main rotor gearbox. Inside the gearbox, this location is already the strongest part of the gearset and is further fortified by the casing around it. The rotor forces and moments are transferred to this ring through the planetary gearset itself and through the bearing at the top of the gearbox case. The truss structure is pin attached to this ring at four points, one of which is redundant. This fourth point ensures that if a critical truss attachments fails, the pilot is still able to fly home. In flight, the truss structure is designed to carry most loads in tension. The only exceptions are the two main tailboom struts, the two engine struts, and the struts between the landing gear crosstubes. The engine struts hold most of the engine weight while it is also supported by the flange on the rear of the auxiliary gearbox. The auxiliary gearbox case carries this minor load to the main rotor gearbox as a shear force. The struts between the landing gear crosstubes hold the fuel tank in place, which causes bending moments on the lowest members of the structure. Upon landing, the airframe truss is designed to deform in a load factor greater than 2, but all major components will remain attached to the airframe under much higher loads in accordance with FAR 27.561.

The tail boom is the third major section. Most of its weight is carried by the two struts which carry a compressive load between the middle of the tail boom and the rear landing gear brackets. These two struts also support half of the tail rotor torque. The load from the main tail boom struts is transferred to the truss structure at the two rear landing gear brackets and then carried through the truss to the main rotor gearbox. In addition to the two long main struts, the tail boom root is connected to the reinforced ring of the main gearbox with two short struts. While these two points do not carry much of the weight of the tail boom, they do carry up to half of the torque of the tail rotor and transfer that torque directly to the main rotor gearbox. The tail boom is a cylindrical monocoque design, manufactured in two parts and riveted together lengthwise. There are three equidistant bulkheads inside that hold bearings in place for the tail rotor shaft and also support the tail rotor control cable. The tail rotor force causes a bending moment on the boom. Therefore, the boom is reinforced on the sides with two aluminum stringers that run the entire length of the tail boom. The stringers transfer load to the root brackets which transfer the tail rotor torque through the two short struts to the main gearbox.

## 9.2 Crashworthiness

During a normal landing, the rear landing gear tube supports 75% of the weight of the aircraft, leaving 25% of the aircraft weight to be supported by the front cross tube. The landing gear has been designed to FAR27 crashworthiness specifications. In case of a hard landing, the landing gear is designed to deform first, before any other components. It will protect the airframe during hard landings that are not hard enough to cause injury. During a crash landing, the landing gear is designed to permanently deform in order to absorb a significant fraction of impact energy, thus minimizing shock transmission to the fuselage. The fuselage belly will then impact the ground and deform to absorb some of the energy. Extra measures have been taken to lessen the forces on the pilot's body during a crash landing. Instead of using expensive off-the-shelf crashworthy seats, a simple, effective and inexpensive method for adding a margin of safety into the seats themselves was developed. Like other crashworthy seats, the penguin's seats are allowed to "stroke" to lessen the forces on the pilot during a crash. However, instead of a complex mechanism that requires a large force peak prior to deformation, crushable and lightweight aluminum foam is used for energy absorption. The foam crushes under a uniform stress [44], without the typical force peak associated with typical stroking devices, as seen in. This foam is located in two columns inside the seat rails. The foam crushes under a force of 14.5 g's [45]in order for the pilot to sustain the crash with minimal injury. The aluminum foam in our seats provides a constant force while being crushed to less than half its original size. With 12 inch columns of foam, they will stroke more than 6 inches before "densification" occurs and the force increases, as seen in Figure 9.1 [46].

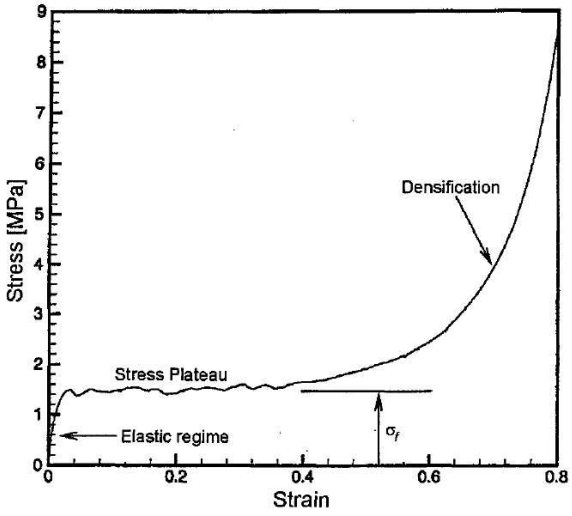


**Figure 9.1:** Stress vs. Strain for Aluminum foam

The foam compressive strength can be tailored depending on the density of the foam. The ultimate stress varies almost linearly with density. The foam chosen is only 9.5% of the density of solid aluminum. If the density of foam is much higher, our cost would be lower, but the "densification" region starts to occur at a lower strain and energy absorbtion would suffer. Our chosen foam columns needs to be $6.16in^2$ in order to crush under a 14.5 g load from a 170lb pilot, which is a 50th percentile pilot. Seen in (Foldout 2) is a male pilot of exactly this stature. The total foam volume for 2 seats would be $6.16in^2$ * 12 in * 2 seats = $148in^3$. This foam can be acquired for \$3/$in^3$ in large quantities, so it would add less than \$500 to the material costs of the seats. With such

crashworthy features, the cost of insuring the helicopter could be reduced.

## 9.3 Engine Mounting

The engine is mounted with the inlet facing the rear of the aircraft. Output power is supplied by the power turbine shaft facing the helicopter cockpit. This allows the power turbine output shaft to be directly coupled to the transmission gearbox, eliminating the need for a long and heavy concentric shaft running through the entire length of the engine. The engine inlet faces the starboard direction. The exhaust is directed towards port to ensure no contamination of intake air by engine exhaust. The engine is coupled to the gearbox using a flexible shaft. Care has been taken to ensure that the engine fits well within the airframe structure. The engine attachments have also been designed to satisfy FAR27 Engine Crashworthiness requirements.

# 10 Subsystems

## 10.1 Cockpit Instruments Layout and Options

Penguin's cockpit incorporates flight and navigation instruments listed in FAR 27.1303 and power-plant instruments list in FAR 27.1305. A set of warning and caution lights as per FAR 27.1322 is also located on the panel. The layout of instruments conforms to FAR 27.1321. Penguin will be certified for Visual Flight Rules (VFR). Therefore, the instruments listed in FAR 91.205 have been designed in the cockpit. Penguin is available in two basic cockpit layouts. While the first one uses the standard "steam-gauges", and the other layout has been designed around two modern Multi-Functional Displays (MFDs).

**10.1.1 Steam-Gauge Cockpit.** This version of cockpit features only the basic standard "steam-gauge" type of instruments listed in Table 10.1. The instrument panel layout for this configuration is shown in Figure 10.1(a). The operator may choose to compliment the functionality by adding the retrofit upgrade options described below to the same basic cockpit. This modular and upgradeable design would lower the initial cost of acquisition of the Penguin, while still providing flexibility to add more options, as and when required by the operator.

**Upgrade Options:**

**(a) Smart Display**

As described in the HUMS chapter (Ch. 8), the data processing and management system has access to a plethora of information from subsystems, air-data sensors, attitude and heading reference system (AHRS), and navigation radio equipment (if installed). This information is stored in the memory unit and is not accessible to the pilot

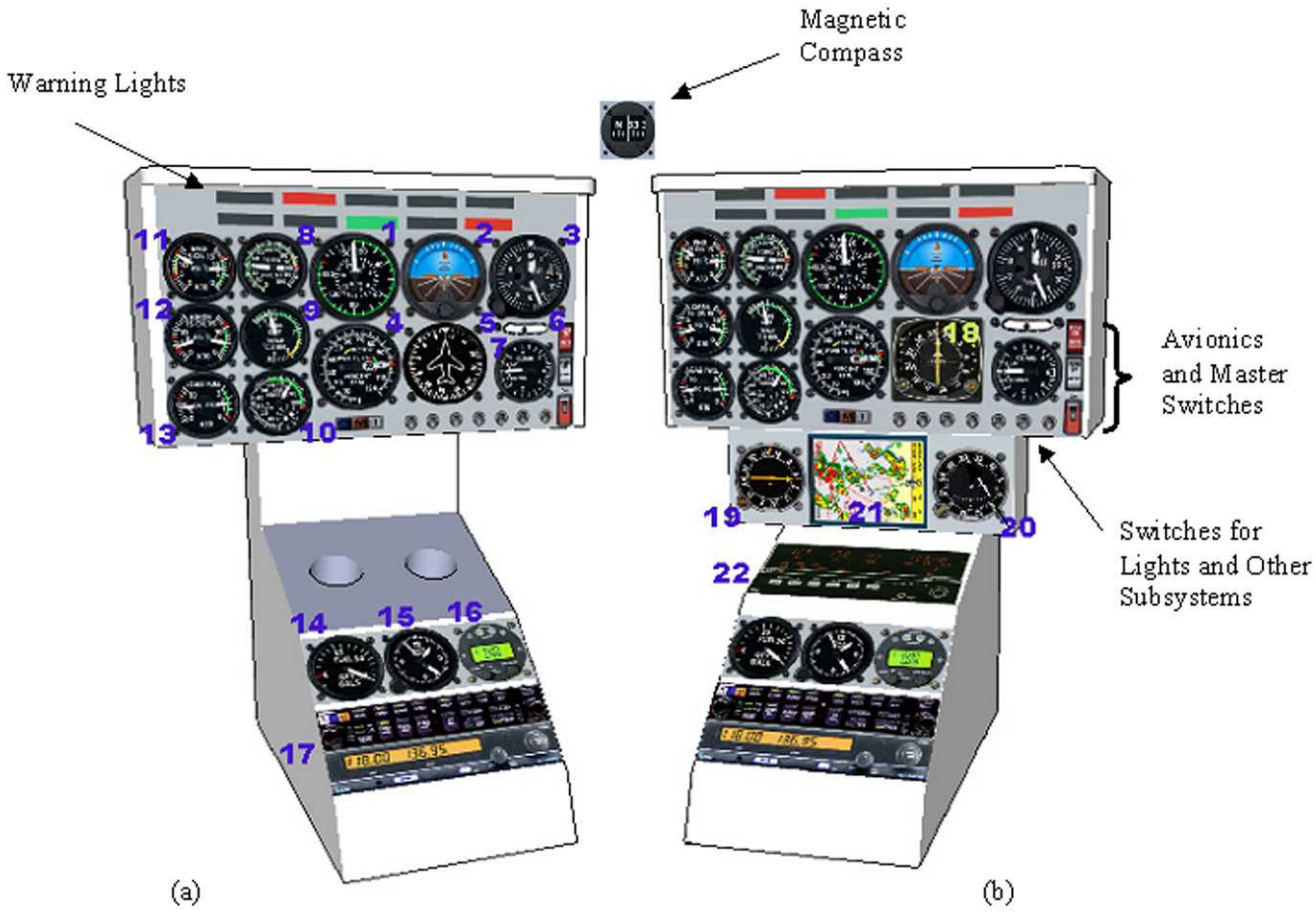


**Figure 10.1:** (a) The Basic "Steam-Gauge" Cockpit Layout, (b) Layout With all Options Installed (List of Equipment in Table 10.1)

| | | | |
|---|---|---|---|
| **1** | Airspeed Indicator | **2** | Artificial Horizon |
| **3** | Altimeter | **4** | MR RPM and power turbine RPM (N2) |
| **5** | Heading Indicator | **6** | Inclinometer |
| **7** | Vertical Speed Indicator | **8** | Engine Torque |
| **9** | Turbine Outlet Temperature | **10** | Gas Generator RPM (N1) |
| **11** | Voltmeter and Ammeter | **12** | MR Transmission Oil Temp and Pressure |
| **13** | Generator Load and Fuel Pressure | **14** | Fuel Quantity |
| **15** | Clock | **16** | Transponder |
| **17** | Audio Panel and Communication Radio | **18** | Horizontal Situation Indicator (HSI) |
| **19** | Automatic Direction Finder (ADF) | **20** | VHF Omnidirectional Range (VOR) |
| **21** | Smart Display | **22** | Navigation Radio (VOR, HSI, ADF, DME) |

**Table 10.1:** List of Cockpit Instruments as Labeled in Fig. 10.1

during flight. Smart Display interfaces with the data processing and management system, and a global positioning system (GPS) receiver to provide a wide variety of valuable information to the pilot (Figure 10.1(b)). It is

designed to make use of recent advances in the display and processing power of Personal Digital Assistants (PDAs), which are mass-produced and are thus available at a very low cost. Inexpensive GPS receivers, GPS software with aviation maps, electronic air-data sensors, and AHRS units are readily available for several PDA platforms [47, 48, 49].

The data processing and management system continuously streams a predefined set of data to the Smart Display. The software on the Smart Display then decides on the parameters to be displayed and their layout based on the pilot input. Audio-visual warnings for conditions such as high descent rate or low altitude can be programmed on the smart display. The sound output of the smart display connects to the audio panel and therefore instead of generic 'beep' for all warnings, specific voice messages can be programmed to alert the pilot. Smart Display also provides display of several derived parameters such as current position on "dead man's curve", estimate of flight time left (based on available fuel), or low tail-rotor authority. In order to reduce pilot workload, basic functions like zooming in or out of the map, and changing views between different predefined sets of parameters are accessible through the buttons on the collective stick.

It is expected that most operators will choose to upgrade to Smart Display over installing an off-the-shelf GPS, as Smart Display provides a lot more features at comparable cost. Regular firmware updates will be released in order to upgrade the firmware on the Smart Display to include improved and better versions, as its design evolves.

**(b) IFR Instruments**

While GPS is fast becoming a primary means of navigation, most helicopters in service still rely on conventional IFR radio instruments such as VHF omnidirectional range (VOR), horizontal situation indicator (HSI), automatic direction finder (ADF) and distance measurement equipment (DME). The Penguin's cockpit can be upgraded to include any or all of these instruments for advanced pilot training, as shown in Figure 10.1(b). As Penguin is not certified for IFR operation, these instruments can only be used for training while still flying under VFR conditions.

**10.1.2 Glass Cockpit.** With advancement in electronic sensors and display systems, most modern helicopter cockpits are being designed around a few multi-functional displays (MFDs) instead of a variety of "steam-gauges". This not only leads to saving in weight, but also provides access to more flight information (by switching between different displays on MFDs), and a cleaner and more simplified cockpit design for reduced pilot workload.

In order to train pilots for such modern helicopters, the glass cockpit version of the Penguin comes equipped with two MFDs that serve as primary flight displays (Fig. 10.2). These MFDs are interfaced with the data

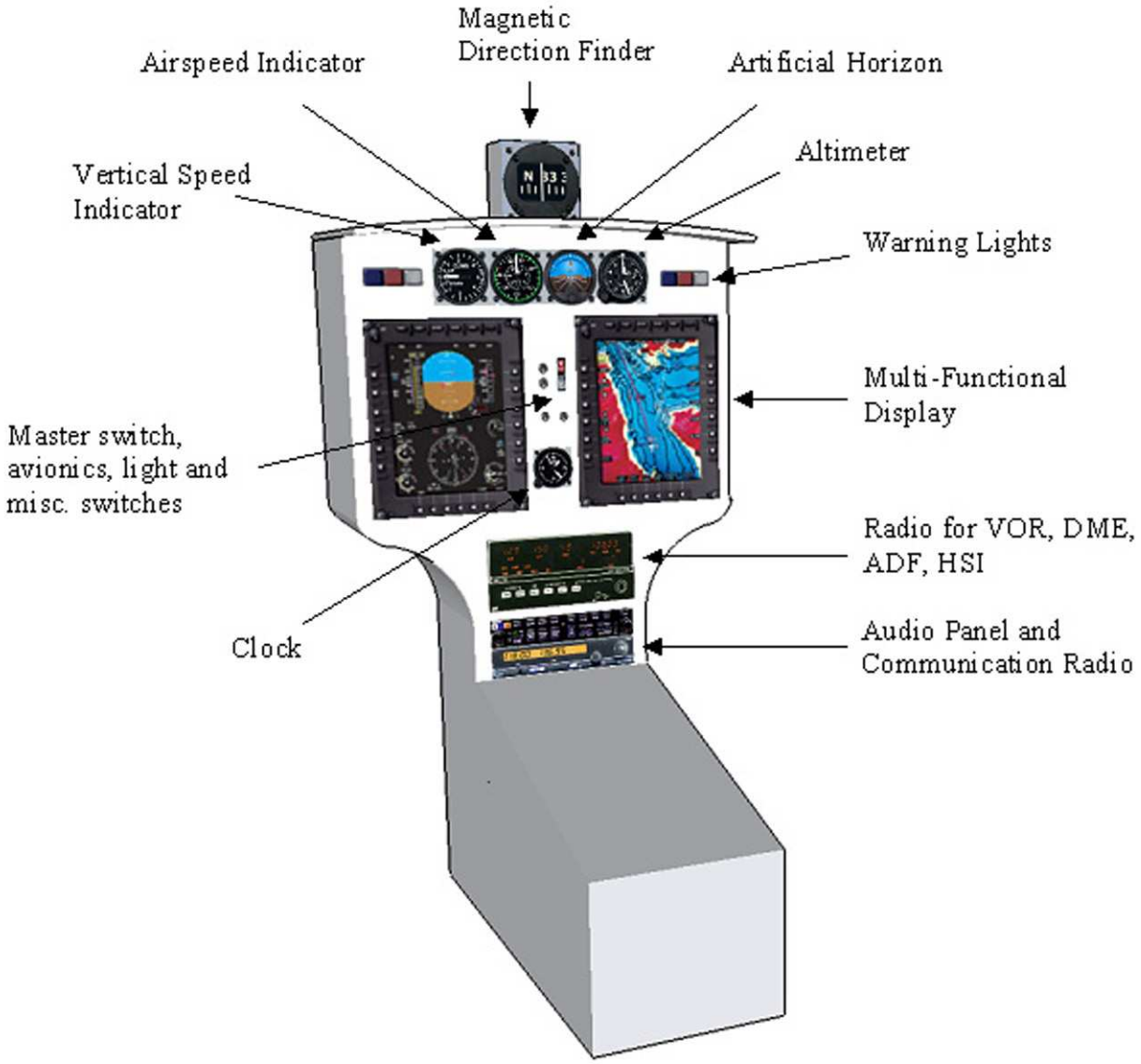


**Figure 10.2:** Glass Cockpit Layout

processing and management system to access subsystem information. These are also capable of displaying the radio-instrument data (VOR, DME, ADF, HSI). Four basic steam-gauges, as shown in Figure 10.2, are provided to serve as backup in case of electrical failure.

The glass cockpit is about 15 lbs lighter than the "steam-gauge" version, which translates into higher payload capability or extended range. Although certified equipment for glass cockpit costs in excess of $50,000, several highly rated, but not yet certified electronic flight information systems (EFIS) consisting of one MFD, sensors (air-data, AHRS, engine probes, GPS, etc) and software are available below $10,000 [49, 50]. This indicates that future versions of glass cockpit could be made available at much lower cost than today and it could eventually

replace the standard “steam-gauge” version.

## 10.2 Flight Controls

In order to reduce the weight, complexity, acquisition cost and maintenance, mechanical flight controls are best suited for this small helicopter. The low pitch link loads and low torsional-stiffness design of flex-beam hub eliminates the need for hydraulic boost.

Individual main rotor collective, cyclic, and tail rotor collective controls are provided for both the pilots. The co-pilot controls are removeable for the transport of passengers. Only the pedals are adjustable, as the cyclic stick is within convenient reach for pilots in the 5% to 95% stature range. The tail rotor is operated with two cables connected to a pulley that is driven by the pedals. The lateral cyclic actuates two push-pull linkages and the longitudinal cyclic actuates one. All three inputs pass through the collective mixer before being reversed just prior to the swashplate. Based on the blade rotating flap frequency, the fixed swashplate is oriented at an angle of 75° prior to the desired flapping response. The mechanical advantage of the control system is designed so that the loads on pilot controls never exceed the limits specified in FAR 27.397. These control linkages and swashplate connections are shown in Figure 5.3. The cyclic push-pull tubes incorporate the lead-lag system for variable handling qualities as described in Ch. 5.

## 10.3 Electrical System

Penguin uses a 28-volt, negative earth, direct current (DC) electrical system and the power is supplied by the starter-generator system, which is permanently coupled to the engine gearbox. A 24-volt, 17 ampere-hour, sealed lead-acid battery provides the electrical power to the starter-generator to start the engine. Once the engine is running, the starter-generator is driven by the engine and is then used as a generator. Power is distributed through a single bus system. The reverse current relay prevents the generator from being connected to the line until reaching operating voltage. In the event of main generator failure, the battery powers the bus. External power may be applied through a receptacle located in the forward section of the fuselage.

## 10.4 Lighting System

The lighting system comprises of a red strobe anti-collision light installed on the tail-boom (as per FAR 27.1401), twin landing lights in the nose (as per FAR 27.1383), optional navigation lights below doors and end of tail, and instrument panel and map lights (as per FAR 27.1381) in the cockpit.

## 10.5 Heating and Ventilation System

Air is forced through a muffler shroud around the engine exhaust system by a fan, and warmed by the exhaust pipes. It then enters the cockpit from an outlet in pilot's foot-well after passing through a shut-off valve. The volume of warm air entering the cockpit can be controlled by the cabin heat control. This heating system conforms to FAR 27.859. A fresh air vent in the nose, and one small vent in each door are provided for ventilation in accordance with FAR 27.831. The doors may also be removed on a very hot day.

## 10.6 Pitot Static System

A heated pitot tube, a static source, and three pitot static instruments (airspeed indicator, altimeter and vertical speed indicator) form the pitot static system. Pitot tube is mounted on the front edge of mast fairing above the cabin. The static system has been designed in accordance with FAR 27.1325.

## 10.7 Flight Data Recorder

No special flight data recorder (FDR) hardware is required on the Penguin, as HUMS (Section 8) has been designed to incorporate its features. The FDR data is stored in a separate file on the same flash memory bank that stores the HUMS data. Different parameters and frequency of data can be programmed on the processor. This entire processing and memory unit is housed in a fireproof and shockproof casing (Fig. 8.1), so that this data can be retrieved in the event of an accident and can be used for investigation. This unit can also be used to record different parameters for evaluation of trainee's performance, flight experiments and research, and for evaluation of new systems, as and when they are installed. Once the Penguin is on ground, this data can be downloaded for post-analysis. Trainees can benefit from this system as the trajectories flown can be reconstructed and even simulated to help understand different flight conditions and maneuvers.

# 11 Performance Analysis

## 11.1 Drag Estimate

The frontal areas of different components of the Penguin were computed from the CAD drawings and the equivalent flat plate areas were estimated based on the methods outlined by Prouty [51]. The estimated flat plate area was increased by 20% as recommended by Prouty to account for future uncertainties, protuberances and other modifications. Table 11.1 shows the drag breakdown for the Penguin. The total flat plate area of Penguin is 4.33 $ft^2$ (0.4 $m^2$). The flat plate area of the fuselage is slightly high because it is not streamlined all the way to the tail rotor. The sharp change in cross-sectional area at the start of the tail boom results in a region of reversed

flow, thereby increasing the parasitic drag. However, the Penguin's cockpit is aerodynamically well designed. Also, Penguin uses a faired landing gear that results in significant drag reductions. The higher rotor-fuselage interference drag may be attributed to the close proximity of the main rotor to the fuselage.

Overall, the estimate of flat plate area of the Penguin is slightly conservative. For example, the OH-6A has a flat plate area of 4.5 $ft^2$ [53], even though it weighs nearly twice as much as the Penguin and has the same overall configuration. An estimate of the equivalent flat plate area of the R22 was also made by simulating the power required versus forward speed curve based on available R22 power, size and cruise speed specifications. The analysis estimated that the flat plate area of the R22 was about 15-20% lower than that of the Penguin, indicating that Penguins drag estimate lies in the same ballpark while also being a conservative estimate. This increases the confidence in the forward flight performance analysis based on the drag estimate obtained above.

| **Component** | **Flat Plate Area** | | **%** |
|---|---|---|---|
| | $ft^2$ | $m^2$ | |
| Fuselage | 1.54 | 0.145 | 42.84 |
| Main Rotor Hub & Shaft | 0.99 | 0.092 | 27.49 |
| Tail Rotor Hub | 0.0537 | 0.005 | 1.49 |
| Landing Gear | 0.441 | 0.041 | 12.25 |
| Horizontal Stabilizer | 0.0035 | 0.0003 | 0.098 |
| Vertical Fin | 0.0073 | 0.001 | 0.202 |
| Interference drag | 0.463 | 0.043 | 12.8 |
| Miscellaneous | 0.1 | 0.009 | 2.77 |
| Subtotal | 3.6 | 0.335 | 100.0 |
| 20 % Increase | 0.72 | 0.067 | |
| Total | 4.33 | 0.402 | |

**Table 11.1:** Drag Breakdown

## 11.2 Hover Performance

The Penguin was designed for good hover performance by an appropriate choice of airfoil (SC-1095), twist ($-11°$) and anhedral ($10°$). The high aspect ratio (and hence low disk loading) also results in relatively low power requirements in hover in comparison with other three bladed rotors. Figure 11.1 shows the HOGE ceiling versus gross weight for different temperature conditions. It is seen that while the HOGE ceiling at maximum gross weight (1345 lb [610 kg]) in ISA+20° C conditions is 6000 ft (as required by the RFP), it is about 10,000 ft in ISA conditions. This is nearly twice the HOGE ceiling of the R22 or Schweizer 300CBi. With a gross weight of 1102 lb (i.e., zero payload), the HOGE ceiling in ISA conditions can be as high as 16,000 ft. These figures indicate the excellent high altitude performance capability of the Penguin in comparison with other helicopters in its weight category. At still lower gross weights (i.e. zero payload and less fuel) higher altitudes are attainable. At altitudes lower than the maximum HOGE altitude, the excess power can be used to climb. Figure 11.2 shows the variation of vertical rate of climb with altitude. At MSL and ISA conditions, the vertical rate of climb is 900

ft/min.

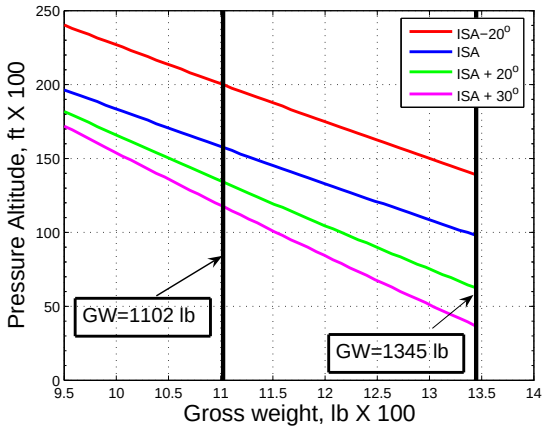


**Figure 11.1:** HOGE Ceiling vs. Gross Weight

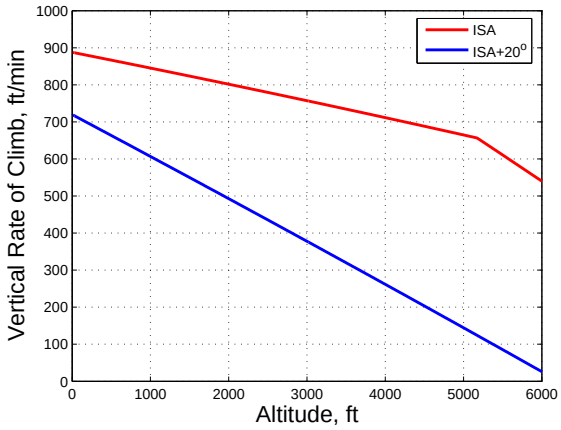


**Figure 11.2:** Vertical Rate of Climb vs. Altitude

## 11.3 Forward Flight Performance

In accordance with the RFP's suggestion that forward flight performance should exceed current piston trainers, the Penguin has a forward flight performance that is far superior to those of its competitors. The high power requirements imposed by the HOGE specifications in the RFP and a proper choice of the derated engine power, enables the Penguin to attain high forward speeds and climb rates in comparison with other competing piston trainers. Longitudinal trim analysis was carried out to determine the power required by the helicopter as a function of forward speed. The analysis used Glauert's theory with rigid blade flapping and uses a table lookup procedure for airfoil properties. Figure 11.3 shows the variation of power required versus airspeed at MSL in ISA conditions.

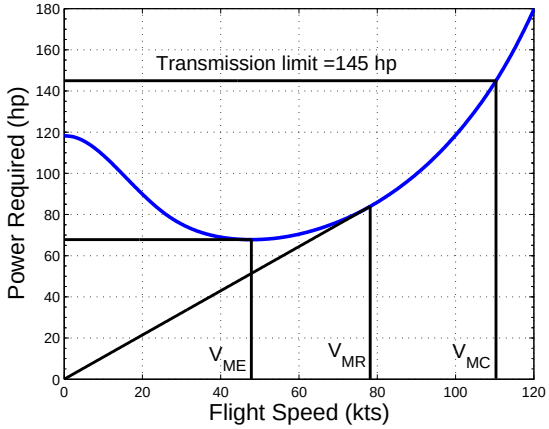


**Figure 11.3:** $P_{reqd}$ vs. Flight speed

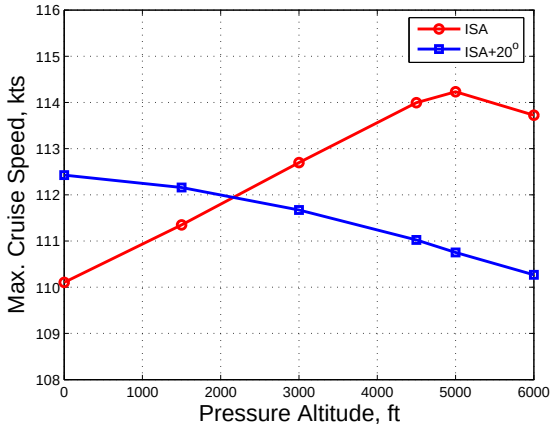


**Figure 11.4:** Max. Cruise Speed vs. Altitude

The maximum cruise speed can be estimated by finding the point of intersection of the power required curve with the power available curve (Figure 6.5). Figure 11.4 shows the variation of maximum cruise speed with altitude. In ISA conditions, the maximum cruise speed ($V_{MC}$) increases with altitude because the power required in high speed forward flight decreases with altitude due to the reduced drag, whereas the power available is equal to the transmission rating (145 hp) up to an altitude of about 5000 ft. On an ISA $+20^\circ$ C day, the maximum cruise speed decreases with altitude because the power available is now below the transmission rating and decreases more rapidly with altitude than the power required. Figure 11.5 shows the fuel required versus airspeed for different gross weights in ISA conditions at MSL. The velocity for maximum endurance ($V_{\mathrm{ME}}$) and maximum range ($V_{\mathrm{MR}}$) can be calculated from the fuel required curves by determining the points corresponding to minimum fuel and minimum-fuel-per-mile (or slope) respectively. Under ISA conditions at Mean Sea Level (MSL), $V_{\mathrm{MC}} = 110$ kts (204 km/hr, 126 mph), $V_{\mathrm{MR}} = 78$ kts (144 km/hr, 90 mph), $V_{\mathrm{ME}} = 48$ kts (89 km/hr, 55 mph).

Because the RFP does not define the cruise speed, it is taken to be the speed corresponding to the the power available at 6000 ft and ISA $+20^\circ$ conditions (i.e., corresponding to $0.862 \times P_{\text{trans. limit}} = 125$ hp). This corresponds to a cruise speed of 103 kts (190 km/hr) at MSL and ISA conditions. Going by this definition for the cruise speed, at 6000 ft and ISA $+20^\circ$ conditions, the cruise speed equals the maximum cruise speed (110 kts [204 km/hr]). The rate of climb of the helicopter while in forward flight, can be obtained by dividing the excess power ($P_{\text{available}} - P_{\text{required}}$) by the gross weight. Figure 11.6 shows the variation of rate of climb with airspeed for different altitude and temperature conditions. At MSL and ISA conditions, the maximum rate of climb of the Penguin is 1894 ft/min. This is nearly twice that of the R22 (1000 ft/min).

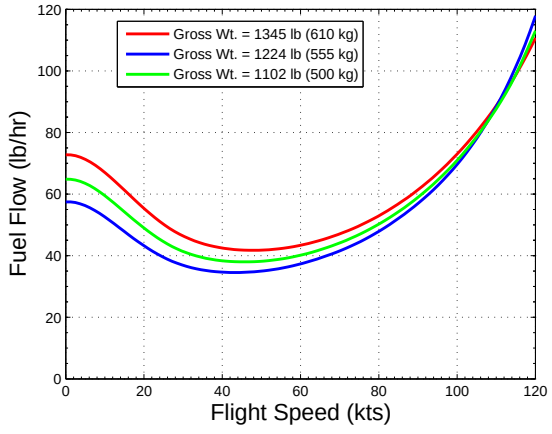


**Figure 11.5:** Fuel Flow vs. Forward Speed

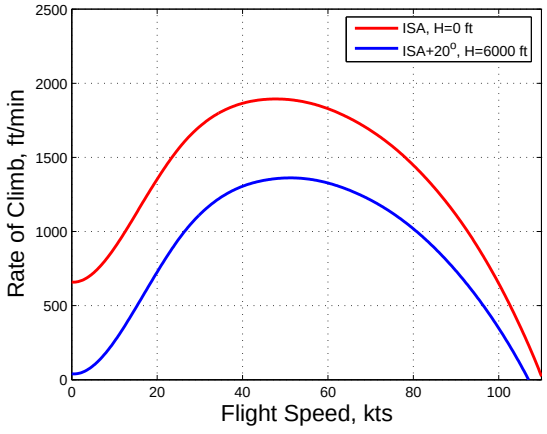


**Figure 11.6:** Rate of Climb vs. Airspeed

## 11.4 Range and Endurance

The range and endurance can be computed from the fuel/power required curves for a given gross weight and altitude. The fuel consumption for maximum endurance corresponds to the minimum point in the curve. Based on this, the endurance of the Penguin at full gross weight (1345 lbs [610 kg]) was obtained as 3.85 hrs at MSL and ISA conditions. At zero payload (i.e., corresponding to 1102 lbs [500 kg]), the endurance was found to be 4.65 hrs. The fuel consumption for maximum range corresponds to the point at which a tangent from the origin intersects the fuel/power required curve. Using this value, the maximum range of the helicopter at full gross weight was obtained as 279 miles (243 nm, 450 km). At zero payload the range of the Penguin found to be 312 miles (243 nm, 504 km). The aforementioned results are reflected in Figures 11.8 and 11.7). The high range and endurance of the Penguin are made possible primarily because of the relatively high fuel requirements necessitated by the RFP specification to hover for 2 hrs at 6000 ft and ISA $+20^{\circ}$ conditions.

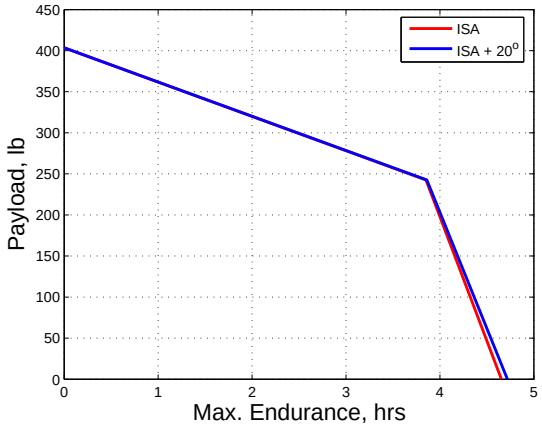


**Figure 11.7:** Payload vs. Maximum Endurance

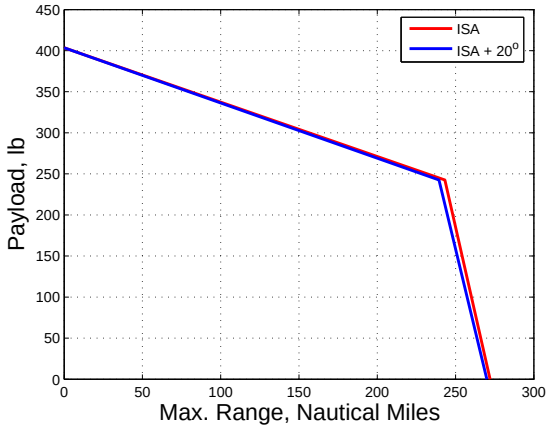


**Figure 11.8:** Payload vs. Maximum Range

## 11.5 Autorotational Performance

The RFP states that the helicopter should have good autorotational capabilities. Autorotational performance is important because the Penguin is primarily a trainer helicopter and safety is a prime concern. The Sikorsky index is generally considered to be a good measure of the autorotational performance and is given by

$$AI = \frac{I\Omega^2}{2W \times DL}$$

where $\frac{1}{2}I\Omega^2$ is the rotor kinetic energy, $W$ is the gross weight and $DL$ is the disk loading. A good autorotational performance therefore requires high rotor kinetic energy and low disk loading. The Penguin main rotor has a

| | R22 | 300CBi | Penguin |
|---|---|---|---|
| HOGE ceiling (ISA) | 5200 ft (1585 m) | 4800 ft (1463 m) | 10,000 ft (3048 m) |
| Max. Cruise Speed | 96 kts (178 km/hr) | 80 kts (140 km/hr) | 110 kts (203 km/hr) |
| Max. ROC | 1000 ft/min | - | 1894 ft/min |
| Range | 209 nm (387 km) | 190 nm (353 km) | 243 nm (450 km) |
| Endurance | 2.2 hrs | 3.0 hrs | 3.85 hrs |

**Table 11.2:** Performance Comparison

tip mass of 2.8 lb at each blade tip to achieve a high rotor kinetic energy. The use of a high aspect ratio blade (and hence a relatively low disk loading for a three bladed rotor), also ensures a good autorotative index. The autorotational index of the Penguin is about 30 $ft^3$/lb. Generally, an autotorotative index of 20 $ft^3$/lb is considered acceptable for a single engine helicopter[52].

Table 11.2 compares the performance characteristics of the Penguin with the R22 and Schweizer 300CBi. The Penguin has 75% more endurance, 20% more range, twice the rate of climb and a 14 kts more forward speed than the R22. The results show that the Penguin, is far superior to its nearest competitors in all performance aspects. These have been made possible by the low gross weight, proper choice of derated engine power (145 hp) and higher fuel capacity.

# 12 Cost Analysis

Acquisition and operational cost minimization is one of the key objectives in the Penguin design. This section identifies the cost cutting features of the design and estimates the acquisition and Direct Operating Cost (DOC) of the Penguin.

## 12.1 Lean Manufacturing

The acquisition price of the airframe and the engine depends on five principal factors: research and development costs, manufacturing, overhead, certification, and value added costs. Keeping the manufacturing costs low has a direct impact on the purchase price of the aircraft.

The aircraft design and assembly process is accomplished through the use of Product Lifecycle Management tools throughout the implementation, from conceptual and detailed design through to full-scale assembly and production. This includes the use of CAD/CAM/CAE software, electronic document tracking and sharing and Total Product Engineering. This enables the product to be designed for ease of manufacture right from the outset, promotes collaboration between the design and the manufacturing teams, and facilitates consistency and rapid dissemination of information. The airframe and engine manufacture will be accomplished through the use

of 'Lean Manufacturing' techniques. This is a systematic approach to minimize the cost of production. The major benefits of this manufacturing philosophy are continual quality improvement, small production runs and the ability to reconfigure the production line for different products. 'Lean Manufacturing' is composed of many elements, including: (i) elimination of waste, (ii) continuous flow and (iii) quality control. Specifically, it would include the use of:

- The minimum number of different types of bolts necessary for the airframe and engine assembly.
- Specification of tight tolerances at the leading edge of the turbine and compressor blades, and relatively larger tolerances at the trailing edge.
- Selection of workable and reasonably inexpensive Nickel based superalloys for turbine blades.
- Forging, which results in low material losses, since components can be produced which are closer to final shape.
- Bolting of various components: tail-boom, transmission, engine and the rotor head to the basic airframe truss network, allowing for ease of transport and assembly of the various components on the shop floor.
- Use of a single jig for the airframe assembly, leading to reduction in manufacturing errors, allowing for the elimination of waste and reduced production time.
- Building up the airframe truss network using shafts having the same diameter, resulting in the selection of an 'off-the-shelf' tube, which further reduces manufacturing costs and production time.

The introduction of 'Lean Manufacturing' initiatives in the Boeing Company has resulted in manufacturing labor costs being reduced by 85%. Sikorsky Aircraft has introduced 'Lean Manufacturing' initiatives, involving thin-client terminals and other digital technologies, resulting in an expected hike in the S-76 helicopter production line from 10-12 helicopters to 35 aircraft with fewer manufacturing errors by the end of 2006. The initiative is expected to be extended to the S-92, UH-60M, MH-60S, and the MH-60R lines[54].

It is apparent that 'Lean Manufacturing' is an innovative manufacturing technique enabling decreased production time and lower manufacturing costs, and therefore is used as one of the major cost-cutting features in the present design.

## 12.2 Acquisition Cost

The acquisition cost estimation is based on historical trends. The Bell Helicopter method [55] provides a set of detailed cost formulas for estimating component costs. It uses component weights, total production quantity and production rate as primary cost drivers.

The Bell cost model was first modified to better estimate the acquisition costs of helicopters in the weight class of the Penguin. The extensive cost, weight, sizing and materials information available for the R22 [56] was

used to modify cost coefficients used in the Bell formula. It was found that reducing the fuselage structure and assembly cost by 30% and using a tooling amortization and profit percentage of 35% (instead of 50%) yields the actual R22 selling price of $215,000. This is justifiable because the R22 and Penguin have a simplified fuselage structure (simple truss support structure instead of a series of bulkheads) that does not extend all the way to the tail rotor. The high production rate of the R22 and Penguin also justify the reduction in the tooling amortization and profit percentage. Based on these refinements, the acquisition cost estimate for the Penguin was computed and the component cost breakdown is summarized in Table 12.1. The acquisition cost of the Penguin ($266k) exceeds that of the R22 by about $50,000. This includes the additional costs associated with the turbine engine, the composite rotor blades and the increased reduction drive system.

The engine cost has been estimated at $55,000. This has been obtained by studying historical trends in engine costs in the size range of the Pyros [17], and further decreasing the cost by 15%, which accounts for:

- Absence of a reduction drive system in the engine.
- Elimination of the lubrication system.
- Practice of lean manufacturing techniques.
- Selection of low cost material for turbine blades.
- Use of an integrated starter-alternator unit.

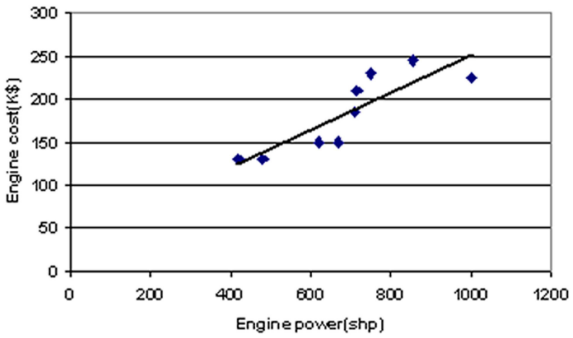


**Figure 12.1:** Comparison of Engine Cost vs. Power for Various Turboshaft Engines [17]

## 12.3 Operating Costs

Operating costs can be divided into Direct Operating Costs (DOCs) and Indirect Operating Costs (IOCs). The DOCs are usually incurred per flight hour, whereas IOCs are generally independent of flying hours. Because IOCs are dependent on operator policy, airport location and policies of local governments, they generally vary from location to location and are difficult to predict at the preliminary design stage. They are therefore not estimated in this report. The DOCs can be broken down further as: Cash DOCs (maintenance, flight crew, fuel and oil); Overhaul DOCs (engine and aircraft parts overhaul, labor) Ownership DOCs (depreciation, hull insurance and finance).

The R22 and the Penguin have nearly the same gross weight, size and range of application. Therefore, the operating costs of the Penguin have been computed using the available R22 DOC breakdown [57]. Table 12.2 shows the operating cost breakdown. The following assumptions have been made in these calculations:

- The Penguin is assumed to fly 500 hours every year.

| Cost Category | Cost |
|---|---|
| Main rotor system | $27,106 |
| Tail rotor system | $3,623 |
| Fuselage Structure | $34,168 |
| Landing Gear | $7,022 |
| Powerplant Structure | $1,680 |
| Drive system | $32375 |
| Flight Control system | $3,220 |
| Instruments system | $16,670 |
| Electrical system | $5,809 |
| Fuselage assembly | $24,795 |
| Manufacturing | $156,470 |
| Tooling Amortization and Profit | $54,764 |
| Engine | $55,000 |
| **Total** | **$266,235** |

**Table 12.1:** Acquisition Cost Breakdown

| | Penguin | R22 |
|---|---|---|
| Depreciation | 0 | 0 |
| Liability Insurance | $1,510 | $1,360 |
| Hull Insurance | $6,443 | $5,802 |
| Total Fixed annual costs | $7,953 | $7,162 |
| **Total Ownership DOC** | **$15.91/hr** | **$14.32/hr** |
| Engine Overhaul | $14.69/hr | $8.50/hr |
| Aircraft Part Overhaul | $31.21/hr | $28.18 |
| Labor | $4.5/hr | $4.50/hr |
| **Total Overhaul DOC** | **$50.40/hr** | **$41.18/hr** |
| Fuel | $23.04/hr | $24.00/hr |
| Oil | $0.20/hr | $0.40/hr |
| Periodic Inspection | $4.95/hr | $6.60/hr |
| Unsced. maint., Parts and Labor | $3.22/hr | $4.30/hr |
| **Total Cash DOC** | **$31.41/hr** | **$35.30/hr** |
| **Total Operating Cost** | **$97.72/hr** | **$90.80** |

**Table 12.2:** Operating Cost Breakdown

- The fuel cost is based on the maximum range fuel requirement of 7.68 gph at $3.00 per gallon.
- The aircraft overhaul, liability insurance and hull insurance costs have been scaled by the ratio of the Penguin and R22 acquisition costs (without engines).
- Labor costs for periodic inspections and unscheduled maintenance costs have been reduced by 25% to account for the cost saving benefits of using the HUMS system and the hingeless rotor configuration.
- Engine overhaul has been scaled by the ratios of the engine cost of the Penguin and R22 while the periodic inspection costs have been reduced by 25% due to
  - Elimination of the lubrication system.
  - Very high durability of the foil air bearings[32].
  - Ease of engine assembly and disassembly, resulting from complete separation of the ‘hot’ and the ‘cold’ sections of the engine.
- Lower manufacturing costs of the radial compressor disk due to improved milling techniques with high precision and accuracy.

The direct operating cost of the R22 is $90.8 (per hour). The analysis shows that the direct operating cost of the Penguin ($97.72/flight hr) compares favorably with that of the R22.

## 12.4 Analysis Limitations

The methods used to predict the Pyros' acquisition costs are based upon historical trends and as a result, do not accurately capture the influence of new technologies such as the use of foil air bearings that eliminate the need for a lubrication system. However, an attempt has been made to provide a reasonable estimate for the savings incurred by the addition of such new technologies. Additionally, for the Penguin, development costs associated with systems such as the bearingless rotor and variable handling qualities are difficult to measure and are not directly factored into the estimate.

# 13 Conclusions

The Penguin is a 2-seater training helicopter installed with the Pyros engine that is designed for low acquisition cost, safety and superior training performance. The Penguin's innovative Variable Handling Qualities system provides low cost *ab initio* and advanced training in the same aircraft - a feature that no other aircraft offers except with a prohibitively expensive FBW FCS. Its composite main rotor blades utilize tailored couplings to reduce vibrations, which in turn eliminates any weight penalty associated with vibration suppression devices. The Pyros, as a low cost oil-free turbine engine, represents a significant step forward in helicopter engines. The weight, acquisition cost and maintenance cost of an oil system are avoided. It is also very compact due to the high rotational speed. The Pyros provides a 50% reduction in SFC and 25% increase in power to weight ratio in comparison with turbine engines of similar horsepower. Cost reductions are achieved through various manufacturing methods.

The Penguin meets or exceeds the RFP requirements, including: (i) the specified hover requirement (ii) good autorotational performance, (iii) crashworthy features such as energy absorbing foam floor and crashworthy seats, (iv) instrumentation and handling representative of the current turbine fleet. In comparison to the R22, the Penguin offers 14 knot increase in maximum cruise speed, 22% more range, 75% greater endurance, twice the rate of climb and twice the HOGE ceiling. With its superior performance, it also can be used for other missions such as intercity commuting and ranching operations. Its ability to hover for two hours lends itself well to surveillance missions. In spite of superior performance, simple and rugged design and many other attractive features, the estimated price of the Penguin is $266,000, which is quite competitive with existing piston trainers. To train the next generation pilots, the innovative and economical Penguin is the best choice.

## MIL-STD-1374 Weight Summary

**MIL-STD-1374 Part 1** **GROUP WEIGHT STATEMENT** PAGE 2
NAME UMD **WEIGHT EMPTY** MODEL Penguin
DATE June 2 2006 REPORT

| | | | | | | | |
|---|---|---|---|---|---|---|---|
| 15 | ROTOR GROUP | | | | | | |
| 16 | BLADE ASSEMBLY | | | 39.50 | | | |
| 17 | HUB & HINGE | ( FOLD WT _____ LBS. ) | | 35.60 | | | |
| 19 | EMPENNAGE GROUP | CANARD | HORIZ. STAB. | VERTICAL FIN | VENTRAL FIN | TAIL ROTOR | |
| 20 | TOTAL | | | | | | |
| 21 | BASIC STRUCTURE | | 2.6 | | | | |
| 22 | SECONDARY STRUCTURE | | | | | | |
| 23 | CONTROL SURFACES | | | | | | |
| 24 | ( INCL. BALANCE WEIGHTS ) | ( ) | ( ) | ( ) | | | |
| 25 | BLADES | | | | | 1.65 | |
| 26 | HUB & HINGE | | | | | 5.80 | |
| 27 | ROTOR / FAN DUCT & ROTOR SUPTS | | | | | | |
| 30 | FUSELAGE GROUP | | | | FUS. / HULL | BOOMS | |
| 31 | TOTAL | | | | 128.00 | 30.20 | |
| 32 | BASIC STRUCTURE | | | | | | |
| 33 | SECONDARY STRUCTURE | | | | | | |
| 34 | ENCLOSURES, FLOORING, ETC. | | | | | | |
| 35 | DOORS, RAMPS, PANELS & MISC. | | | | | | |
| 38 | ALIGHTING GEAR GROUP TYPE * | MAIN | NOSE / TAIL | | ARR. GEAR | CAT. GEAR | |
| 39 | TOTAL | 43.00 | | | | | |
| 57 | TOTAL STRUCTURE | | | | | | 286.4 |

* LANDING GEAR "TYPE": INSERT "TRICYCLE", "TAIL WHEEL", "BICYCLE", "QUADRICYCLE", OR SIMILAR DESCRIPTIVE NOMENCLATURE.

** WING, FUSELAGE, ETC.

**SAWE RP NO. 8A - PART I** **GROUP WEIGHT STATEMENT** PAGE 3
NAME UMD **WEIGHT EMPTY** MODEL Penguin
DATE June 2 2006 REPORT

| | | | | | | | |
|---|---|---|---|---|---|---|---|
| 58 | PROPULSION GROUP | | AUXILIARY | | MAIN | | |
| 59 | ENGINE | | | | 132.30 | | |
| 60 | ENGINE INSTALLATION | | | | 26.50 | | |
| 63 | ENGINE COOLING | | | | | | |
| 68 | LUBRICATING SYSTEM | | | | | | |
| 69 | FUEL SYSTEM | | | | 5.80 | | |
| 70 | TANKS - PROTECTED | | | | 10.30 | | |
| 74 | DRIVE SYSTEM | | | | | | |
| 75 | GEAR BOXES, LUB SYS & RTR BRK | | 35.64 | | 73.30 | | |
| 76 | TRANSMISSION DRIVE | | | | | | |
| 77 | ROTOR SHAFT | | | | 8.70 | | |
| 78 | GAS DRIVE | | | | | | |
| 80 | FLIGHT CONTROLS GROUP | | | | 41.40 | | |
| 81 | COCKPIT CONTROLS | | | | | | |
| 82 | AUTOMATIC FLIGHT CONTROL SYSTEM | | | | | | |
| 83 | SYSTEM CONTROLS | | | | | | |
| 84 | AUXILIARY POWER GROUP | | | | | | |
| 85 | INSTRUMENTS GROUP | | | | | | |
| 88 | ELECTRICAL GROUP | | | | 106.20 | | |
| 89 | AVIONICS GROUP | | | | | | |
| 90 | EQUIPMENT | | | | | | |
| 91 | INSTALLATION | | | | | | |
| 93 | FURNISHINGS & EQUIPMENT GROUP | | | | | | |
| 94 | ACCOMMODATION FOR PERSONNEL | | | | | | |
| 95 | MISCELLANEOUS EQUIPMENT | | | | 16.10 | | |
| 96 | FURNISHINGS | | | | | | |
| 114 | TOTAL WEIGHT EMPTY PG. 2-3 | | | | | | 743 |

# References


[1] Copp, Peter. Informal survey of 105 R22 accident reports (2000-2005) from www.ntsb.gov, 2006.

[2] Tischenko, M. N., Nagaraj, V. T. and Chopra, I., "Preliminary Design of Transport Helicopters," *Journal of the American Helicopter Society*, Vol. 48 (2), April 2003, pp. 71–79.

[3] http://www.sacusa.com/helicopters/300cbi.asp, accessed May 31, 2006.

[4] Turnour, S., *Component Weight Breakdown for Robinson R22*, Robinson Helicopter Company, through personal correspondence.

[5] Anon., The Official Helicopter BlueBook, Helivalue$, Inc. 2001.

[6] Bao, *et. al.*, "Design and Hover Test of Low Vibration Mach Scale Rotor with Twisted Composite Tailored Blade," *Proceedings of the* 44th *AIAA/ASME/ASCE/AHS/ASC Structures, Structural Dynamics, and Materials Conference, Norfolk, VA* , April 2003.

[7] Alex, F.W. and McCoubrey, G.W., "Design and Structural Evaluation of the SH-2F Composite Main Rotor Blade," *Journal of the American Helicopter Society*, April 1986, pp. 345–359

[8] http://www.lord.com, May 2006

[9] Johnson, W., *Helicopter Theory*, Dover Publications Inc., New York, 1994.

[10] Lynn, *et. al.*, "Tail Rotor Design, Part 1 - Aerodynamics," *Journal of American Helicopter Society,* Vol.15, No.4, 1969.

[11] Hindson, W.S., "New Capabilities and Recent Research Programs of the NASA/Army CH-47B Variable Stability Helicopter," American Helicopter Society 42$^{th}$nd Annual Forum, Washington, DC, 1986.

[12] Moralez, E., Hindson, W. S., Frost, C. R., Tucker, G. E., Arterburn, D. R., Kalinowski, K. F., and Dones, F., "Flight Research Qualification of the Army/NASA RASCAL Variable-Stability Helicopter," *Proceedings of the American Helicopter Society 58$^{th}$ Annual Forum*, Montréal, Canada, Jun 2002.

[13] Sissingh, G. J., "Some Remarks on Dynamic Stability of the Helicopter and Characteristics of Gyratory Stabilizing Systems," *Proceedings of the Eighth Annual Forum*, Washington, DC, 1952.

[14] Stiles, L. R., Freisner, A. L., Mayo, J., Landis, K. H., Kothmann B. D., "Impossible to Resist: The Development of Rotorcraft Fly-by-wire Technology," American Helicopter Society 60$^{th}$ Annual Forum, Baltimore, MD, 2004.

[15] Edenborough, H. K., K. G. Wernicke, "Control and Maneuver Requirements for Armed Helicopters," American Helicopter Society 20th Annual Forum *(Proceedings Supplement),* Washington, DC, May 1964.

[16] *Handling Requirements for Military Rotorcraft,* ADS-33E-PRF, U.S. Army Aviation and Troop Command, Mar. 2000.

[17] Discussion with Mr. David J.H.Eames, Chief, Product and Techonology Strategy at Rolls-Royce, Indianapolis, U.S.A.

[18] Balje,O.E., *TURBOMACHINES: A Guide to Design, Selection and Theory*,John Wiley and Sons, New York, 1981.

[19] Boyce, M.P., *Centrifugal Compressors: A Basic Guide*, Pennwell Books, 2002.

[20] Walsh, P.P. and Fletcher, P., *Gas turbine performance*.

[21] Engeda,A., *The Design and Performance Results of Simple Flat Plate Low Solidity Vaned Diffusers,* Proc. Inst. of Mech. Eng., Part A: Journal of power and energy, Vol.215, Number 1, 2 February 2001, pp 109-118.

[22] Rangwala, A., *Turbo-machinery Dynamics: Design and Operation* , McGraw-Hill, 2005.

[23] http://www.radical-departures.net/2001/metalex_turbopump_full.asp, accessed May 31, 2006.

[24] Lefevre, A., *Gas Turbine Combustion* Taylor and Francis, 1998.

[25] *Materials Data Handbook,* Cambridge University Engineering Department.

[26] *Radial Inflow Turbines,* Module 4A3,Turbomachinery I handout 6, http://www2.eng.cam.ac.uk/~tph/4A3_6.pdf.

[27] Garde, J.V.D., Boot, J., Winkes, J., Tijl, P., Honselaar, M.*Steam and Gas turbines*.

[28] *High-Temperature materials in Gas Turbines,* Elsevier Scientific Publishing Company.

[29] Strang, A., Conroy, R. D., Banks W. M., Blackler, M., Leggett, J., McColvin, G. M., Simplson, S., Smith, M., Starr, F., Vanstone, R. W., *‚An Affordable Creep-Resistant Nickel-Base Alloy for Power Plant* Institute of Materials, Proceedings

of the 6th International Charles Parsons Turbine Conference, Engineering Issues in Turbine Machinery, Power Plant and Renewables, London, 2003, 525–535.

[30] *Materials Selection For High Temperature Applications,* TKK-MTR-4/05, Laboratory of Engineering Materials Publications, 2005.

[31] DellaCorte, C., Pinkus, O., *Tribological Limitations in Gas Turbine Engines: A workshop to Identify the Challenges and Set Future Directions,* NASA/TM-2000-210059/REV1, August 2002.

[32] *Oil-Free Turbomachinery Technology for Regional Jet, Transport and Supersonic Business Jet Propulsion Engines*.

[33] Spring S.D., Kaminske, M., Leone, Steve., Drexel, M. V., Bugra, H. E., Ames, E., C., Agrawal, G., Burr, D., Brophy, M., *Application of Compliant Foil Air Bearings for Free Operation of Advanced Turboshaft Engines,* 62nd AHS Conference, Phoenix, May 2006.

[34] http://www.miti.cc/, May 2006.

[35] http://www.turbokart.com/home.htm, accessed May 31, 2006.

[36] Dudley, D, *Handbook of Practical Gear Design*, CRC Press LLC, Boca Raton, FL, 1994.

[37] Schimidt, A. H., "A Method of Estimating the Weight of Aircraft Transmissions," Presentation at the $35^{th}$ Annual Conference of the Society of Allied Weight Engineers, Inc., Philadelphia, PA, May, 1976.

[38] Burroughs, L. R., "Helicopter Mechanical Power Transmission," Presentation at the $29^{th}$ Annual Conference of the Society of Auronautical Weight Engineers, Inc., Washington, DC, May, 1970.

[39] Weitzman, C., "Development of Low Cost HUMS," *Proceedings of the American Helicopter Society $55^{th}$ Annual Forum*, Montréal, Canada, May, 1999.

[40] Anon., Electronic Code of Federal Regulations (e-CFR), http://www.gpoaccess.gov/ecfr/, May $24^{th}$, 2006.

[41] http://www.epp.goodrich.com/fyreroc/, May $26^{th}$,2006.

[42] Ferdinand P. Beer, E. Russell Johnston Jr., Elliot R. Eisenberg, George H. Staab. Vector Mechanics for Engineers: Statics. McGraw-Hill, 2003.

[43] Lincoln Electric "Aluminum: Experience in Application: What you should know about welding aluminum" http://www.lincolnelectric.com/knowledge/articles/content/alumapp.asp

[44] Anon., ERG Materials and Aerospace Corporation, http://www.ergaerospace.com, May $15^{th}$, 2006.

[45] Desjardin, S. P., "The Evolution of Energy Absorption System for Crashworthy Helicopter Seats," American Helicopter Society $59^{th}$ Annual Forum, Phoenix, AZ, May, 2003.

[46] S.A. Meguid1, J. Heyerman and J.C. Stranart. University of Toronto. Finite Element Modeling of the Collapse of Ultralight Foam-Filled Structures. 42nd AIAA/ASME/ASCE/AHS/ASC Structures, Structural Dynamics, and Materials Conference and Exhibit. Seattle, WA. April 2001.

[47] Aircraft Spruce and Speciality Company, http://www.aircraftspruce.com/catalog/avpages/navair.php, accessed May 31, 2006

[48] PCAvionics, http://www.pcavionics.com/index.jsp, accessed May 31, 2006

[49] PC Flight Systems, http://www.pcflightsystems.com/, accessed May 31, 2006

[50] Blue Mountain Avionics, http://www.bluemountainavionics.com/, accessed May 31, 2006

[51] Prouty, R. W., *Helicopter Performance Stability and Control*, Kreiger Publishing Company, Florida, 2005. 1955.

[52] Leishman, J. G., *Principles of Helicopter Aerodynamics,* Cambridge University Press, New York, 2000, Chapter 6, Figure 6.21.

[53] Leishman, J. G., *Principles of Helicopter Aerodynamics,* Cambridge University Press, New York, 2000, Chapter 5, Figure 5.19.

[54] *Vertiflite,* Vol. 51, No. 2, 2005.

[55] Anon., Bell Cost Model, 2002 American Helicopter Society RFP.

[56] http://www.robinsonhelicopter.com, accessed May 31, 2006.

[57] http://www.robinsonheli.com/pdf_files/betaiiopercosts.pdf, accessed May 31, 2006